

AN ABSTRACT OF THE DISSERTATION OF

Amber Hames for the degree of Doctor of Philosophy in Chemistry presented on August 9, 2017.

Title: Investigations of Two Chemical Systems Relevant to Pyroprocessing Used Nuclear Fuel.

Abstract approved: _____

Alena Paulenova

Pyroprocessing is an advanced technology for recycling used nuclear fuel. Pyrochemical processes encompass a wide range of chemical, physical, and electrochemical methods to partition fission products and other components from used nuclear fuel, which allows for the reuse of the actinides in nuclear fuel. This dissertation investigates two chemical systems relevant to pyroprocessing. The first investigation explores the possibility of using molybdate melts containing sodium molybdate (Na_2MoO_4) and molybdenum trioxide (MoO_3) to partition fission products from used nuclear fuel by crystallization. The difference in solubility of the fission product metal oxides compared to the uranium oxide or molybdate in the molybdate melt allows for these separations to occur. Uranium dioxide dissolves in the molybdate at high temperatures, and upon cooling, the uranium precipitates as uranium dioxide or molybdate, whereas the fission product metals remain soluble in the melt. The feasibility of UO_2 purification from the fission products was studied using small-scale experiments with gram quantities of uranium dioxide. The composition of the uranium precipitate as a function of molybdate melt composition was determined through a series of tests. The effectiveness of the partitioning of several fission product surrogates between the uranium precipitate and molybdate melt for various parameters in the process was also studied. A melt consisting of 20 wt% MoO_3 -50 wt% Na_2MoO_4 -30 wt% UO_2 heated to 1313 K and cooled to 1123 K for the physical separation of the UO_2 product from the melt, and washed once with Na_2MoO_4 resulted in

excellent separation of the UO_2 from the surrogate fission products. The second investigation explored the phase equilibria of UCl_3 and NpCl_3 in the LiCl-KCl molten salt electrolyte used in electrorefining used nuclear fuel. The re-evaluation of the LiCl-UCl_3 , KCl-UCl_3 and the LiCl-KCl-UCl_3 phase diagrams and the first known evaluation of the KCl-NpCl_3 system were performed. Samples of varying compositions within each of these systems were thermally analyzed by DSC to determine the temperature and types of the phase transitions. Samples were then analyzed by XRD to determine the identity of the phases formed, and ICP-OES or ICP-MS to establish the cation ratio. The LiCl-UCl_3 system displayed a simple eutectic system. The KCl-UCl_3 system displayed two eutectics and the K_2UCl_5 phase, which was identified by DSC and XRD. There was no evidence of a K_3UCl_6 phase. These LiCl-UCl_3 and KCl-UCl_3 phase diagrams were used to produce a portion of the LiCl-KCl-UCl_3 phase diagram relevant to electrorefining. The LiCl-KCl-UCl_3 system displayed two ternary eutectics and was consistent with literature data. The KCl-NpCl_3 system displayed two eutectics and the K_2NpCl_5 and K_3NpCl_6 phases, which were identified by DSC and XRD. The evaluation of these phase diagrams allows for an improved understanding of the LiCl-KCl-UCl_3 and KCl-NpCl_3 systems and their application to pyroprocessing.

©Copyright by Amber Hames

August 9, 2017

All Rights Reserved

Investigations of Two Chemical Systems Relevant to Pyroprocessing Used Nuclear Fuel

by
Amber Hames

A DISSERTATION

submitted to

Oregon State University

in partial fulfillment of
the requirements for the
degree of

Doctor of Philosophy

Presented August 9, 2017
Commencement June 2018

Doctor of Philosophy dissertation of Amber Hames presented on August 9, 2017

APPROVED:

Major Professor, representing Chemistry

Chair of the Department of Chemistry

Dean of the Graduate School

I understand that my dissertation will become part of the permanent collection of Oregon State University libraries. My signature below authorizes release of my dissertation to any reader upon request.

Amber Hames, Author

ACKNOWLEDGEMENTS

To my advisor Dr. Alena Paulenova, thank you for accepting me into your research group and taking a chance on me, and allowing me to study solid state actinide chemistry, when you are such an actinide expert.

To the Paulenova research group, thank you for being so warm and welcoming to a very homesick Chicagoan, and for all the help you have given me over the years, especially Vanessa Holfeltz, Dr. Joseph Lapka, Dr. M. Alex Brown, and Dr. Brian Gullekson.

To Dr. Mark Williamson, my Argonne National Laboratory advisor, thank you for allowing me to research at Argonne for so long. When I started my summer internship with the pyroprocessing group seven years ago, I never thought I had it in me to get a doctorate in chemistry. Thank you for giving me that push I needed to get here and for never letting me give up.

To Dr. James Willit and the pyroprocessing group at Argonne, thank you for all the help and support you have giving me over the years. You are my second family. I am so happy and proud to be a part of this group.

To Bob Blaskovitz, I do not know if I can ever thank you enough. You have taught me so much and helped me so much, that I will forever be grateful. Thank you for helping me fix the “unfixable” STA.

To my mom, thank you for giving me the love, courage, and support to achieve my dreams. I could not have done this without you.

To my dad, thank you for introducing me to science. It was the best gift you could have given me.

To my sisters, thank you for being there for me through all of this.

To Charlie, thank your support, love and help through all of this. You never let me give up. You never doubted me. Thank you for everything, I cannot wait until you are my husband.

CONTRIBUTION OF AUTHORS

Dr. Mark Williamson and Dr. Alena Paulenova assisted with the editing of each manuscript. Dr. Peter Tkac also assisted with editing Chapter 4.

TABLE OF CONTENTS

	<u>Page</u>
1. Introduction.....	1
1.1. Overview of Pyroprocessing	1
1.2. Goals and Motivation	3
1.2.1. Project 1. Investigation of Molybdate Melts as an Alternative Method of Reprocessing Used Nuclear Fuel	3
1.2.2. Project 2. Phase Equilibria Studies in Molten Chloride Systems Relevant to Pyroprocessing.....	4
1.3. Figures	5
2. Literature Review.....	6
2.1. Project 1. Investigation of Molybdate Melts as an Alternative Method of Reprocessing Used Nuclear Fuel.....	6
2.1.1. $\text{Na}_2\text{MoO}_4 - \text{MoO}_3$ System	6
2.1.2. UO_2 in the $\text{Na}_2\text{MoO}_4 - \text{MoO}_3$ System	7
2.1.3. Fission Product Oxides in the $\text{Na}_2\text{MoO}_4 - \text{MoO}_3 - \text{UO}_2$ System	8
2.2. Project 2. Phase Equilibria Studies of the UCl_3 and NpCl_3 in the LiCl-KCl System	10
2.2.1. Thermodynamics of Phase Diagrams	10
2.2.2. Thermodynamically Probable Phase Diagrams	13
2.2.3. LiCl-KCl System	15
2.2.4. LiCl-UCl_3 System	15
2.2.5. KCl-UCl_3 System.....	16
2.2.6. LiCl-KCl-UCl_3	18
2.3. Neptunium Trichloride Chemistry	19
2.3.1 Synthesis of NpCl_3	20
2.3.2. Structure of NpCl_3	24
2.3.3. Enthalpy of Formation	24
2.3.4. Standard Entropy	25
2.3.5. High Temperature Heat Capacity	26
2.3.6. Vapor Pressure and Melting Temperature	26

	<u>Page</u>
2.4. Figures.....	27
3. Chapter 3: Experimental	34
3.1. Project 1. Investigation of Molybdate Melts as an Alternative Method of Reprocessing Used Nuclear Fuel.....	34
3.1.1. Materials	34
3.1.2. Molybdate Melt Studies	34
3.1.3. Composition of Uranium Product.....	35
3.1.4. Principles of X-ray Diffraction	36
3.1.5. Dissolution of Uranium Product for ICP-MS Analysis	37
3.1.6. Principles of Inductively Coupled Plasma- Mass Spectrometry.....	37
3.2. Project 2. Phase Equilibria Studies of the UCl_3 and $NpCl_3$ in the $LiCl-KCl$ System.....	38
3.2.1. Materials	38
3.2.2. UCl_3 and $NpCl_3$ Synthesis	38
3.2.3. Thermal Analysis of Samples	38
3.2.4. Differential Scanning Calorimetry.....	39
3.2.5. XRD Analysis	41
3.2.6. Dissolution of Sample for ICP-OES Analysis	42
3.2.7. Principles of ICP-OES	42
3.3. Figures.....	42
Chapter 4.....	47
Investigation of Molybdate Melts as an Alternative Method of Reprocessing Used Nuclear Fuel	47
4.1. Abstract	48
4.2. Introduction.....	48
4.3. Experimental	50
4.3.1. Materials	50
4.3.2. Experimental Setup of the Melt	50
4.3.3. Composition of Uranium Product.....	51
4.3.4. Dissolution of Uranium Product for ICP-MS Analysis	52

	<u>Page</u>
4.4. Results.....	52
4.4.1. Uranium Speciation	52
4.4.2. Fission Product Partitioning.....	53
4.5. Discussion	53
4.5.1. Uranium Composition.....	53
4.5.2. Fission Product Partitioning.....	54
4.6. Conclusion	59
4.7. Acknowledgements.....	60
4.8. References.....	60
4.9. Figures.....	61
Chapter 5.....	70
Phase Equilibria Studies of the LiCl-KCl-UCl ₃ System.....	70
5.1. Abstract	71
5.2. Introduction.....	71
5.2.1. LiCl-KCl	72
5.2.2. LiCl-UCl ₃	73
5.2.3. KCl-UCl ₃	73
5.2.4 LiCl-KCl-UCl ₃	75
5.3. Experimental	77
5.3.1. UCl ₃ Synthesis	77
5.3.2. DSC-TGA	78
5.3.3. ICP-OES	78
5.3.4. XRD	78
5.4. Results and Discussion	78
5.4.1. LiCl-UCl ₃ System	78
5.4.2. KCl-UCl ₃ System.....	79
5.4.3. LiCl-KCl-UCl ₃ System	81
5.5. Summary	83
5.6. Acknowledgements.....	83

	<u>Page</u>
5.7. References.....	84
5.8. Figures.....	86
Chapter 6.....	100
Phase Equilibria Studies of the KCl-NpCl ₃ System	100
6.1. Abstract	101
6.2. Introduction.....	101
6.3. Experimental	102
6.3.1. NpCl ₃ Synthesis	102
6.3.2. DSC.....	103
6.3.3. XRD	103
6.3.4. ICP-MS	104
6.4. Results and Discussion	104
6.4.1. Neptunium Chloride Synthesis	104
6.4.2 Phase Equilibria Results	105
6.5. Conclusion	106
6.6. Acknowledgements.....	106
6.6. References.....	107
6.8. Figures.....	109
7. Conclusion	117
8. Bibliography	118

LIST OF FIGURES

<u>Figure</u>	<u>Page</u>
Figure 1.1 Overview of main processed in pyroprocessing used nuclear fuel.....	5
Figure 2.1 An example of a binary phase diagram of components A and B of a simple eutectic.....	28
Figure 2.2 An example of a binary phase diagram of components A and B with a congruently melting intermediate compound	29
Figure 2.3 An example of a binary phase diagram of components A and B with an incongruently melting intermediate compound	30
Figure 2.4 An example of a ternary phase diagram.....	31
Figure 2.5 An example of a ternary phase diagram of components A, B, and C with the binaries only consisting of simple eutectic systems.....	32
Figure 2.6. The crystal structure of NpCl_3	33
Figure 3.1 Flowchart diagramming UO_2 partitioning in the molybdate melt.....	44
Figure 3.2 Experimental setup inside the tube furnace.....	45
Figure 3.3 Actinide chloride synthesis quartz and Pyrex reactor vessel.....	46
Figure 3.4 DSC curves for a sample of 13.24 ± 0.03 mol% UCl_3 - LiCl	47
Figure 4.1 Flowchart diagramming UO_2 partitioning in the molybdate melt.....	64
Figure 4.2 Experimental setup inside the tube furnace.....	65
Figure 4.3 Photographs of uranium precipitates obtained from the melts of varying MoO_3 , Na_2MoO_4 , and UO_2 compositions.	66
Figure 4.4 XRD pattern of uranium precipitate obtained from the salt mixture containing 20% MoO_3 -50% Na_2MoO_4 - 30% UO_2	67
Figure 4.5 Distribution ratios for selected fission products at varying concentrations of MoO_3 and Na_2MoO_4 , and constant 30% UO_2	68
Figure 4.6 Distribution ratios of fission products from tests conducted at two dissolution temperatures followed by cooling at a rate of 38 k min^{-1}	69
Figure 4.7 Distribution ratios of the fission products after uranium precipitate was treated with one or three Na_2MoO_4 washes.....	70

<u>Figure</u>	<u>Page</u>
Figure 5.1 LiCl-UCl ₃ phase diagram drawn from DSC heating curve data with actual data points overlaid.....	87
Figure 5.2 LiCl-UCl ₃ phase diagram drawn from DSC heating curve data with data points from previous phase diagrams.....	88
Figure 5.3 DSC curves for a sample of 13.24 ± 0.03 mol% UCl ₃	89
Figure 5.4 KCl-UCl ₃ phase diagram drawn from DSC heating curve data with actual data points overlaid.....	90
Figure 5.5 KCl-UCl ₃ phase diagram drawn from DSC heating curve data with data points from previous phase diagrams.....	91
Figure 5.6 The XRD results for a sample of 10 mol % UCl ₃ -KCl after thermally cycling by DSC.....	92
Figure 5.7 DSC curves for a sample of 10.81 ± 0.03 mol% UCl ₃ -KCl.....	93
Figure 5.8 LiCl-KCl-UCl ₃ liquidus projection drawn.....	94
Figure 5.9 LiCl-KCl-UCl ₃ liquidus projection of the isotherms with experimental data.....	95
Figure 5.10 DSC heating curve for a sample of 67.85 mol% UCl ₃ , 4.8 mol % LiCl, and 27.35 mol% KCl.....	97
Figure 5.11 The XRD results for a sample of about 20 mol% UCl ₃ , 12 mol% LiCl, and 68 mol% KCl.....	98
Figure 5.12 Isothermal projection of the LiCl-KCl-UCl ₃ system at 773 K.....	99
Figure 5.13 Isothermal projection of the LiCl-KCl-UCl ₃ system at 823 K.....	100
Figure 6.1 The XRD scan for NpCl ₃ product.....	111
Figure 6.2 DSC of the NpCl ₃ product.....	112
Figure 6.3 Experimentally determined phase diagram of the KCl-NpCl ₃ system.....	113
Figure 6.4 The XRD scan for a sample containing 12.4 mol% NpCl ₃	114
Figure 6.5 DSC heating curve for a sample containing 12.4 mol% NpCl ₃	115
Figure 6.6 The XRD results for a sample of 31.0 mol % NpCl ₃	116
Figure 6.7 DSC heating curve for a sample containing 31 mol% NpCl ₃	117

LIST OF TABLES

<u>Table</u>	<u>Page</u>
Table 2.1 Lattice parameters for NpCl_3	33
Table 2.2 Enthalpy of formation for NpCl_3 at 298 K	33
Table 2.3 Standard entropy for NpCl_3 at 298 K.....	34
Table 2.4 Heat capacity for NpCl_3	34
Table 2.5 Fusion data for NpCl_3 vapor pressures and melting temperatures.....	34
Table 3.1 Fission product composition.....	43
Table 4.1 Fission product composition based on a calculated composition.....	63
Table 4.2 XRD results of uranium species precipitated from different compositions of MoO_3 , Na_2MoO_4 , and UO_2	66
Table 5.1 Experimental results and literature values of eutectic composition and melting temperature for the LiCl-UCl_3 system.....	88
Table 5.2 Experimental results and literature values for eutectic compositions and melting temperatures in the KCl-UCl_3 system.....	92
Table 5.3 Experimental results and literature values of eutectic compositions and melting temperatures for the LiCl-KCl-UCl_3 system.....	96
Table 6.1 Experimental parameters and product of each step of the NpCl_3 synthesis.....	110

1. Introduction

1.1. Overview of Pyroprocessing

Since the early 1950s the United States has been developing pyrochemical technology for reprocessing used nuclear fuel. Pyrochemical processes encompass a wide range of chemical, physical, and electrochemical methods to partition fission products and other components from used nuclear fuel to allow for the reuse of the actinides. These processes include: electrorefining, electrowinning, oxidation/reduction reactions that allow for selective extraction of metals from molten salt, fractional crystallization, precipitation, selective absorption in molten salt, and vacuum distillation.[1] These processes have many advantages including the use of inorganic salts that are more resilient against radiolytic degradation. These inorganic salts also have the potential to significantly reduce the volume of waste produced during the processing compared to other forms of reprocessing, such as aqueous solvent extraction methods [2-4].

In the 1960s melt refining was used to recover uranium from Experimental Breeder Reactor (EBR-II) fuel. In melt refining, the uranium and plutonium fuel alloys were melted in a lime-stabilized zirconia crucible in an inert atmosphere at 1673 K for several hours. The fission products in the fuel would either form dross, or be removed via volatilization. The molten actinide metal was then be poured away from the dross. Volatilization was used to remove fission product elements or compounds with high vapor pressures (i.e., noble gases, cesium, cadmium, iodine, and calcium iodide). Selective oxidation was used to remove alkaline earth, and rare earth elements. These elements would react with the oxygen in the zirconia crucible, and form dross on the surface of the crucible. Some materials insoluble in the melt, would react with the dross, and adhere to it. Certain fission products, such as molybdenum, technetium, ruthenium, rhodium, palladium, silver, and tin could not be removed via melt refining and were recycled with the fuel. These fission products are known as the noble metals. [5, 6]

Modern pyroprocessing technology employs pyrometallurgical and electrochemical processes to recover and recycle actinides in used nuclear fuel. Pyroprocessing is effective for recycling fast reactor and light water reactor (LWR) fuel,

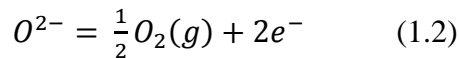
with a goal to recover 99.9 % of the actinides in the used fuel. The technology can be used to treat oxide or metallic fuel discharged from the reactor. [2-4, 7, 8]

Figure 1.1 displays the main unit operations involved in pyroprocessing used nuclear fuel. Metallic fuel discharged from a fast reactor or LWR fuel discharged from a thermal reactor is first chopped into segments. Since LWR fuel is an oxide fuel, the used oxide fuel must be reduced to its metallic state in the oxide reduction unit in order to recover the actinides in the electrorefiner. [2]

In the oxide reduction unit, the electrochemical cell consists of the cathode which is comprised of the chopped segments of the LWR fuel in a fuel basket, the anode which is typically an inert material such as platinum, or an inert ceramic, and the molten electrolyte of LiCl-Li₂O at 923 K. As a current is passed between the cathode and the anode, the metal ions of the metal oxides are reduced to their metallic state at the cathode, while the oxide ions are transported through the electrolyte and oxidized at the anode, where oxygen gas is released. The half reactions for this electrochemical system are given in Equations 1.1 and 1.2.



Anode:



In these equations, M stands for the actinide or other metal (e.g., lanthanide, transition metal) that is reduced. The alkali and alkaline earth oxides in the fuel react with the LiCl, and form chlorides, which are soluble in the electrolyte. [2-4]

In the electrorefiner, metallic fuel in a basket now serves as the anode in the electrochemical cell. The electrolyte is LiCl-KCl containing UCl₃ (<8 wt %) at 773 K or LiCl containing UCl₃ at 923 K. This system generally contains two separate cathodes, one for uranium deposition, and one for uranium and transuranic element (U/TRU) co-deposition, meaning the electrochemical cell consists of two electrical circuits. Passing current through the system anodically dissolves the metallic fuel at the anode. Uranium ions are soluble in the electrolyte, transport through the salt, and are reduced at the cathode where they deposit onto the cathode in the metallic state. Transuranic elements form chlorides upon anodic dissolution, which are soluble in the electrolyte. They can be co-deposited with the U at a separate cathode under

proper conditions. Lanthanides also anodically dissolve forming chlorides soluble in the electrolyte; however, they remain in the melt, and are not deposited onto a U/TRU cathode. Other active metal fission products partition to the salt phase as soluble chlorides while the noble metals remain in the anode basket. [2-4, 9, 10]

Uranium recovered from the electrorefiner is typically in dendritic form containing about 15 wt% electrolyte. This electrolyte salt contains transuranic and fission product chlorides that need to be removed before the uranium can be reused as a fuel source. The electrolyte is vaporized from the uranium product at 1073 K. The U/TRU recovered also contains a significant amount of electrolyte that needs to be removed before the U/TRU can be recycled as a fuel source. Due to the low melting point of the U/TRU, a bottom pour method is used to recover the U/TRU metal. The recovered U and U/TRU metal is then sent to the fuel fabrication, where it is cast into new fuel assemblies. [2-4]

1.2. Goals and Motivation

1.2.1. Project 1. Investigation of Molybdate Melts as an Alternative Method of Reprocessing Used Nuclear Fuel

The use of pyrochemical methods (i.e., high temperature chemical reactions) to recover actinides from used nuclear fuel has been investigated since the 1950s. [2-4] Traditionally, pyrometallurgical and electrochemical methods were developed for the recovery of actinides; however, other pyrochemical methods have been explored.

One method of interest is the recovery of actinide oxides by recrystallization in molybdate melts [11-13]. This method is applicable to LWR or fast reactor fuel of high burn-up, in which recycled fuel does not require a high purification factor such as that used in fast systems. In this approach, the used fuel is dissolved in a melt consisting of sodium molybdate (Na_2MoO_4) and molybdenum trioxide (MoO_3) at temperatures in the range 1223-1413 K. At these temperatures, UO_2 (or transuranic oxides) and fission product oxides are soluble in the melt. Upon cooling to temperatures between 1073-1123 K, the UO_2 (or transuranic oxides) recrystallize while the fission products remain soluble in the melt. At this point, the UO_2 can be physically removed from the melt containing the fission products. [11-15]

This process is of interest in a modified open fuel cycle, which does not make extensive use of chemical processing, to recover actinides for recycle to an advanced reactor that does not require fuel with high decontamination factors (i.e., fast neutron spectrum systems). To investigate the feasibility of molybdate melts for the purification of the UO_2 , small scale experiments using gram quantities of uranium were conducted. The recovery of UO_2 as a function of the composition of the molybdate melt, the temperature of the system, and number of Na_2MoO_4 washes were explored.

1.2.2. Project 2. Phase Equilibria Studies in Molten Chloride Systems Relevant to Pyroprocessing

The electrorefiner is considered the essential component for pyroprocessing used nuclear fuel. In the electrorefiner, uranium, transuranics, lanthanides, alkali and alkaline earth metals anodically dissolve in the electrolyte, resulting in a build-up of contaminants in the electrolyte. [2] A concentration gradient of UCl_3 (and transuranic chlorides) develops at the anode-salt interface and the cathode-salt interface as current is passed in the cell. [16] Ternary phase formation resulting from complexation within the liquid electrolyte could impact the process of electrorefining by impacting the chemical activity of the U and TRU chlorides in the electrolyte. This multi-component electrolyte has multifarious thermodynamics properties and phase equilibria because of the potential formation of ternary or more complex compounds.

To better understand the behavior of the ever-changing electrolyte during electrorefining, the phase equilibria of the LiCl-KCl-UCl_3 system must be established. Thus, the phase diagram of the LiCl-KCl-UCl_3 system needs to be defined. In order to do that, the binary systems for the LiCl-KCl , LiCl-UCl_3 , and KCl-UCl_3 must first be developed and assessed before the ternary phase diagram can be produced. As the LiCl-KCl system has been well defined in the literature, [17-28], this study will focus on determining data for the LiCl-UCl_3 , [28-30], KCl-UCl_3 , [29, 31-33] and LiCl-KCl-UCl_3 systems [16, 32, 34] in which the data is lacking, and/or inconsistent. The goal of this work is to experimentally determine the LiCl-UCl_3 , KCl-UCl_3 and LiCl-KCl-UCl_3 phase diagrams to improve the fundamental understanding of the chemistry of the actinide chlorides in the LiCl-KCl-UCl_3 system.

The activity of neptunium in the molten electrolyte was also of interest because there is no literature regarding the behavior of neptunium chloride in this molten electrolyte. The phase

behavior of NpCl_3 with KCl was of interest because the possible intermediate compound formation in this system could impact the chemical activity of neptunium during electrorefining.

1.3. Figures

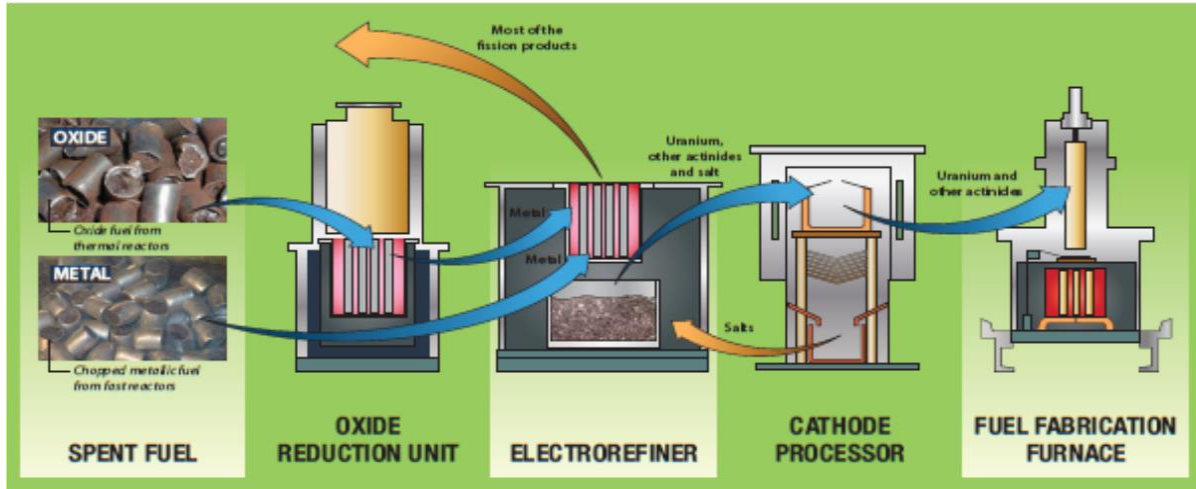


Figure 1.1 Overview of main processes in pyroprocessing used nuclear fuel. [8]

2. Literature Review

2.1. Project 1. Investigation of Molybdate Melts as an Alternative Method of Reprocessing Used Nuclear Fuel

In the early 1970s Ustinov *et al.* began investigating systems of metal oxides with MoO_3 to understand the recrystallization of the metal oxides from molybdate melts. [35-37] Ustinov reported on the interactions of several metal oxides such as: UO_2 , PuO_2 , ZrO_2 , RuO_2 , La_2O_3 , and CeO_2 with MoO_3 . He also studied UO_2 and PuO_2 in $\text{MoO}_3\text{-Na}_2\text{MoO}_4$, and reported that UO_2 and PuO_2 displayed very poor solubility in Na_2MoO_4 in inert atmosphere (~ 0.2 mol % at 1273 K for UO_2 , and ~ 0.1 mol % at 1273 K for PuO_2). The fission product oxides, with the exception of RuO_2 , are more soluble in MoO_3 than UO_2 or PuO_2 , and are oxidized to form molybdates that are soluble in Na_2MoO_4 . [11] Increasing the temperature of the system increases the solubility of UO_2 (and PuO_2) in the MoO_3 . Ustinov reported that Na_2MoO_4 serves to precipitate the UO_2 or PuO_2 upon cooling in the system. [13] In 1997, Ustinov determined that recrystallization from molybdate melts could be used to purify UO_2 and PuO_2 from fission products in used nuclear fuel. [13] The separation is based on the difference of solubility of the uranium (and plutonium) and fission product oxides in the melt. When studying the purification of the uranium from fission products in a melt only consisting of $\text{UO}_2\text{-MoO}_3$, Ustinov reported that $\text{U}(\text{MoO}_4)_2$ recrystallized, and the melt yielded a 98-99% purification from Cs, Ce, Pr, Zr, and Nb; however only a 60% purification from Ru and Rh was achieved [1]. Additional Na_2MoO_4 washes have been reported to further purify the uranium product from the fission products, and to decompose any $\text{U}(\text{MoO}_4)_2$ that has crystallized. [11-14, 35-39] When studying the purification of the uranium from fission products in a melt consisting of $\text{Na}_2\text{MoO}_4\text{-UO}_2\text{-MoO}_3$ the UO_2 recrystallized and the purification from Cs, La, Zr and Nb was 98.5-99.9% efficient. [13]

2.1.1. $\text{Na}_2\text{MoO}_4\text{-MoO}_3$ System

Molybdenum exhibits a wide range of oxidation states in oxide form. Both the MoO_3 and the Na_2MoO_4 are in the (VI) oxidation state. Na_2MoO_4 is a spinel structure that is isostructural with Na_2WO_4 . It consists of Na^+ cations in the octahedral coordination and MoO_4^{2-} anions in tetrahedral coordination. [40] Na_2MoO_4 is known to exhibit three solid phase transitions, which

occur at 773, 853, and 915 K and it melts at 958 K. [40, 41] In molybdate compounds, Mo-O form strong covalent bonds. [42]

MoO₃ consists of layers of MoO₆ units in which the Mo is six coordinate. The MoO₆ are in an octahedra structure, and are edge-sharing to form chains. The chains are cross-linked by oxygen atoms, forming layers. The coordination around the Mo is a distorted octahedra [43, 44].

According to the Na₂MoO₄-MoO₃ phase diagrams, this system forms two ternary phases Na₂Mo₂O₇ and Na₂Mo₄O₁₃ [45-47]. Certain systems of dialkali-metal polymolybdates have been studied by Raman spectroscopy upon melting to identify the melting behavior of these systems. Dialkali-metal dimolybdates, such as Na₂Mo₂O₇, form ribbons of corner-sharing MoO₄ and MoO₆ groups, [48-51]. Each Mo₂O₇²⁻ anion is connected to its neighboring anion by weak Mo-O bonds. Upon melting only the MoO₄ tetrahedra exist. [51] In molten Na₂Mo₂O₇, the two linked MoO₄ consist of terminal groups and bridge bonds [48]. The dialkali-metal tetramolybdates form ribbons of MoO₆ octahedra that are also edge-sharing. Upon melting, four linked tetrahedral of MoO₄ consisting of terminal and two middle groups of MoO₂ and bridge bonds form. [48]

2.1.2. UO₂ in the Na₂MoO₄ – MoO₃ System

Uranium and plutonium dioxide exist in the fluorite structure at room temperature. In this structure, the uranium is eight coordinate, and each oxygen is four coordinate. [52] The UO₈ cubic polyhedra are edge sharing. Upon melting, the coordination around the U lowers to be ~40% UO₆, ~40% UO₇, and a 20% mixture of UO₅ and UO₈. The connectivity of the UO_x polyhedra changes from edge sharing to 60% corner sharing, 33% edge sharing and 7% face sharing. [53]

UO₂ is soluble in MoO₃, with its solubility increasing with temperature. In Na₂MoO₄, UO₂ has a solubility of only about 0.2 mol% at 1273 K. [13] Studies of the UO₂-MoO₃ system identified the formation of UMoO₅, UMo₂O₈, and UMo₁₁O₃₅. [13] In the UO₂-MoO₃ system, the MoO₃ is a Lewis acid, as it accepts electrons from the Lewis base UO₂. In the UMoO₅, β-UMo₂O₈, and UMo₁₁O₃₅ structures, the U or Mo coordination polyhedra polymerize. The polymerization leads to extended structural units and these structures are considered complex oxides consisting of ReO₃-type slabs of

corner-sharing MoO_6 distorted octahedra. The number of octahedra across the ReO_3 slab is determined by the formula of the complex: $\text{UOM}_n\text{O}_{3n+1}$, where n denotes the number of MoO_6 across the slab. In these structures, the U is seven coordinate in the pentagonal bipyramid structure. The pentagonal bipyramids form chains by edge-sharing. The $\text{UOM}_n\text{O}_{3n+1}$ structure consists of layers of the chains of the UO_7 polyhedra, and the MoO_6 octahedra. The UO_7 and MoO_6 are bonded by the apical O of the pentagonal bipyramids, and the apical corners of the octahedra. [54] UMo_2O_8 also exists in a high temperature α phase and a low temperature γ phase. In the α - UMo_2O_8 , the U^{4+} exists in an octahedral coordination and a nine-coordinate tricapped trigonal prism. The U and Mo coordination polyhedral are corner sharing.[54] In the γ - UMo_2O_8 , the U^{4+} exists in square antiprismatic coordination. The UO_8 and MoO_4 polyhedra are connected by corner-sharing. [54, 55]

UO_2 has very limited solubility in Na_2MoO_4 . $\text{U}(\text{MoO}_4)_2$, however, it is soluble in Na_2MoO_4 , and is known to form $\text{Na}_2\text{U}(\text{MoO}_4)_3$ and $\text{Na}_4\text{U}(\text{MoO}_4)_3$. [11, 56]

$\text{Na}_2\text{U}(\text{MoO}_4)_3$ has a scheelite structure with the Na^+ and the U^{4+} cations surrounded by eight oxygen atoms. The Mo^{6+} is in the tetrahedral coordination with four oxygen atoms.[57] $\text{Na}_4\text{U}(\text{MoO}_4)_4$ is in a super scheelite structure. The super scheelite structure consists of MoO_4 tetrahedra and UO_8 and NaO_6 polyhedra. The MoO_4 share corners with the NaO_6 , and the UO_8 share corners with eight different MoO_4 . The UO_8 connects to the NaO_6 by edge sharing. The MoO_4^{2-} vacancies result in the Na atom to be six coordinate as opposed to eight coordinate, which Na is in the scheelite structure. [56]

2.1.3. Fission Product Oxides in the Na_2MoO_4 - MoO_3 - UO_2 System

Fission product oxides found in used nuclear fuel are more soluble in MoO_3 than UO_2 , with exception of RuO_2 . [35] The fission product molybdates formed upon dissolution are not isostructural with the UO_2 , which prevents co-crystallization. The fission product oxides are known to form various molybdates with MoO_3 , none of which are isostructural with the uranium molybdates.[55, 58-60] In studying the molybdate melts to remove the fission products from the UO_2 , Tul'ski *et al.* determined four methods in which the fission products could contaminate the UO_2 product [37]:

1. The fission product oxide could dissolve into the melt and enter into the UO_2 product by adsorption or trapping of the melt onto the surface of the UO_2 product.

2. The fission product cation could be substituted for the Na^+ cation the uranium mixed molybdate $3\text{Na}_2\text{MoO}_4 \cdot 2\text{U}(\text{MoO}_4)_2$.
3. The fission product oxide or molybdate could exhibit parallel crystallization with the UO_2 and not be washed out during elutriation because the density of the fission product oxide is too close to the density of the UO_2 product.
4. The fission product oxide could form a solid solution with the UO_2 , by incorporating the fission product into the UO_2 lattice during crystallization.

Washing the U-bearing product with multiple Na_2MoO_4 washes would reduce the fission product contamination occurring by first two methods. The fission product oxide on the surface of the product would be dissolved in the Na_2MoO_4 wash, removing the contamination from the product. The mixed molybdate would decompose in the Na_2MoO_4 wash thus removing the fission products from the UO_2 product. For lanthanum this method of contamination is very likely, as $\text{La}_2\text{Mo}_3\text{O}_{12}$ and $\text{La}_2\text{Na}_2\text{Mo}_4\text{O}_{16}$ are known to form a solid solution when the La^{3+} replaces three Na^+ cations. [61] Cesium is also speculated to contaminate a mixed molybdate of $3\text{Na}_2\text{MoO}_4 \cdot 2 \text{U}(\text{MoO}_4)_2$ by replacing the Na^+ cation.[37]

Physically removing the UO_2 product from the melt would mitigate the third method of contamination by separating the UO_2 product from the melt upon cooling. As RuO_2 is not soluble in the MoO_3 , Tul'skii concluded that the RuO_2 crystallizes in parallel with UO_2 , and claimed the RuO_2 can be separated if there are separate zones for crystallization.[37] The physical separation of the UO_2 upon cooling to temperatures low enough for UO_2 to precipitate allows for the separate zones to reduce co-crystallization. At these temperatures (1073 -1123 K), the liquid fission product oxides remain soluble in the melt, while the UO_2 is precipitated.

The final method of contamination, the formation of solid solutions, is the most likely method of contamination for most fission product elements, especially the lanthanides. [62, 63] The following fission product oxides are known to form solid solutions with UO_2 : SrO [63], ZrO_2 [63-66], La_2O_3 [67, 68], CeO_2 [63, 69, 70], Nd_2O_3 [63, 71, 72], Eu_2O_3 [73, 74], Gd_2O_3 [75-77], Dy_2O_3 [78, 79], Er_2O_3 [80], and Lu_2O_3 [80]. In these solid solutions, the cation of the fission product has a radius of similar size to the U^{4+} radius; a fission product cation randomly replaces the U^{4+} cation in the UO_2 structure without changing the fluorite

structure of the UO_2 . The fluorite structure is commonly subjected to non-stoichiometric defects and remains stable. Uranium dioxide in particular has an anion excess structure, which allows for excess O^{2-} anions to be accommodated in interstitial sites. [67, 70, 72, 73, 81, 82]

2.2. Project 2. Phase Equilibria Studies of the UCl_3 and NpCl_3 in the LiCl-KCl System

2.2.1. Thermodynamics of Phase Diagrams

The equilibrium state occurs when Gibbs free energy is at its minimum for a given set of external conditions. The general equation for Gibbs free energy is given in equation 2.1 [83, 84]:

$$G = PV - TS + \mu_1 X_1 + \dots + \mu_i X_i \quad (2.1)$$

In this equation, G is Gibbs free energy, P is the pressure of the system, V is the volume of the system, T is absolute temperature, S is entropy, μ_i is the chemical potential of the i^{th} component, and X_i is the mole fraction of the i^{th} component. [83]

A phase diagram graphically represents the phases in a system in equilibrium under a given set of conditions. [84] A phase is defined as a physically homogenous portion of a system that is bound by a surface so that it is mechanically separated from any other portion. The components of a system are the smallest number of independently variable chemical constituents that are essential to convey the phases that exist in the equilibrium state. The variance, which is also known as the degrees of freedom, represents the externally controllable variable(s), which include temperature, pressure and the composition of the components in the phase. These variables allow for the condition of the system to be defined. [83] The phase rule, developed by J. Willard Gibbs, allows for the conditions of equilibrium to be defined by the relationship of the number of phases and components in the system. The phase rule is given in equation 2.2 [83, 84]:

$$F = C - P + 2 \quad (2.2)$$

In this equation, F is the variance, C is the number of components, and P is the number of phases. The relationships within phase diagrams are dictated by this rule. [83, 84] The phase rule is directly related to the Gibbs free energy relationship. In a two phase system, the energy gain by the first phase, α , must be equal to the energy loss by the second phase, β ; therefore, the total change in free energy is zero. This relationship is shown in the following equations [83]:

$$dG = dG^\alpha - dG^\beta \quad (2.3)$$

$$dG = (-SdT + VdP + \mu_i^\alpha dX_i) - (-SdT + VdP + \mu_i^\beta dX_i) \quad (2.4)$$

$$dG = \mu_i^\alpha dX_i - \mu_i^\beta dX_i \quad (2.5)$$

For a system with two components, the two phases coexisting leads to the following two equations [83]:

$$\mu_1^\alpha(T, P, X_1^\alpha) = \mu_1^\beta(T, P, X_1^\beta) \quad (2.6)$$

$$\mu_2^\alpha(T, P, X_2^\alpha) = \mu_2^\beta(T, P, X_2^\beta) \quad (2.7)$$

In this system, there are four independent variables, T, P, X_1^α and X_1^β . The variance is determined by comparing the number of independent variables to the number of equations; therefore, for the two component system with two equations, and four independent variables, there are two unknowns. These two unknowns are variables that can be fixed without changing the number of phases in the system, meaning this system has two degrees of freedom. [83, 84]

A binary system can be represented as a two component system and at constant pressure the phase rule becomes $F = C - P + 1 = 3 - P$.

Figure 2.1 is an example of a binary temperature composition phase diagram of a simple eutectic. In this system, both end members melt congruently, thus the solid is in equilibrium with the liquid of the same composition at fixed temperature and pressure. Notice in figure 2.1 the line labelled liquidus. All compositions at temperatures above the liquidus line will exist in a single-phase liquid solution. Below the solidus line, in figure 2.1, all compositions will be in the A and B phases. A sample at equilibrium at temperatures and compositions between the liquidus and solidus will consist of a solid and liquid phase. When a sample is at equilibrium at a temperature and composition above the liquidus curve, for example at 20 mole % B at 850 K, and is slowly cooled to the liquidus temperature, 700 K, the first solid, A, begins to appear. Continuing to decrease the temperature further increases the precipitation of the solid, while the liquid composition follows the liquidus curve to the eutectic composition. The solidification of the A and B phases are complete at the solidus temperature, 500 K. [84]

Congruently melting intermediate compounds can exist in binary systems, an example is given in figure 2.2. In the example, the compound A_2B_3 is in equilibrium as 40 mole % A and 60 mole % B as a liquid at temperatures above 685 K. The A_2B_3 compound divides the A-B system

into two simple eutectic systems. At the first eutectic, at 65 mol% A and 35 mol % B at 500 K, there is a coexistence of A, A_2B_3 and the liquid. At this point, there are three phases present, so at constant pressure, according to the phase rule, the variance is zero. At the second eutectic, 20 mol% A and 80 mol% B at 600 K, B, A_2B_3 and the liquid coexist while the variance is again zero. [83]

Incongruently melting compounds can also exist in binary systems, an example is given in figure 2.3. During incongruent melting a solid phase transforms to another solid phase and a liquid, both of different compositions, at a specified temperature. In a system with incongruent melting a peritectic point exists. The peritectic point in figure 2.3 occurs at 45 mole % A and 55 mole % B, melting at 685 K. At this point, the three phases of B, AB_3 and liquid coexist, meaning the variance is zero. At 25 mole% A and 75 mole % B at 685 K, the AB_3 compound decomposes to solid B and a liquid of 45 mole% A and 55 mole % B. While increasing the temperature, the solid B will coexist with the liquid until the temperature of melting, 785 K, is reached. [83]

Ternary phase diagrams are the superposition of three binary systems represented in the form of the equilateral Gibb's triangle. Increasing the system to three components changes the phase rule to $F = 3 - P + 2 = 5 - P$. In a condensed system of constant pressure the phase rule converts to $F = 4 - P$. In a 3 dimensional representation of the ternary phase diagram, the base of the diagram, which makes the equilateral triangle, is comprised of the mole fractions of the three components. The temperature is displayed perpendicular to the base. The two dimensional representation of the ternary system is often the polythermal projection of the liquidus surface. Liquidus surface projections are shown in figures 2.4 and 2.5. In this representation, the constant temperature lines representing, the liquidus transitions are called, the liquidus isotherms, and represent the equilibrium between the solid phase, and the liquid. In three simple binary eutectic systems, lines from the three eutectics intersect at the ternary eutectic point, shown in figure 2.4 in bold. In a system of A-B-C, on the line extending from eutectic A-B, e_1 , to the ternary eutectic point, E, the A and B solids are in equilibrium with the liquid phase, thus the variance is one. The e_1 -E line is a valley where the temperature is lower than the liquidus isotherms. At the E, the A, B, C solid and the liquid phases are in equilibrium, so the variance is zero. A composition of 75 mol% A, 12.5 mol% B and 12.5 mol% C lies in the primary crystallization of A. As this

composition is cooled from about 500 K, an A-rich solid begins to precipitate. As the temperature is further cooled, the A-rich solid precipitates out, while the $X_B:X_C$ ratio in the liquid remains the same. Upon cooling to about 400 K, the e_2 -E valley is reached, and a B-rich solid begins to co-precipitate. Once the temperature reaches about 380 K, the ternary eutectic temperature is reached, the ternary eutectic reaction occurs.[83, 84]

$$liquid = s_a + s_b + s_c \quad (2.8)$$

Figure 2.5 displays a ternary liquidus projection of two binary systems with a simple eutectic, and a binary system with a congruently melting compound. This system consists of four binary eutectics, and two ternary eutectics. The solid phases include A, B, AC_2 , and C. The red line that joins AC-B is the true binary join, also known as the Alkemeades line. This line breaks the A-B-C triangle into two separate composition triangles, or subsystems, of A- AC_2 -B, and C- AC_2 -B. When a boundary line, such as E_1 - E_2 intersects the Alkemeade like, the intersection represents a temperature maximum for the boundary line, and a temperature minimum on the Alkemeade line. All liquid compositions in the C- AC_2 -B triangle complete crystallization at E_1 , while all liquid compositions in the A- AC_2 -B triangle complete crystallization at E_2 . If the liquid's composition is on the AC_2 -B line, crystallization will complete at the point on the AC_2 -B line that intersects E_1 - E_2 boundary line. [83]

2.2.2. Thermodynamically Probable Phase Diagrams

Phase diagrams are produced from thermodynamic calculations, or experimental data. It is very important to check the validity of a proposed phase diagram, which can be achieved by observing the general pattern of the proposed phase diagram. Okamoto developed the following guidelines to determine if a proposed phase diagram is probable:[85, 86]

1. At zero solute, a two-phase field cannot extend to the pure element side of the phase diagram.
2. Both ends of the liquidus transitions of intermediate phases must meet at invariant reactions, such as a eutectic, or peritectic transition.
3. Tie-lines must end at phase boundaries.
4. Two boundaries of the same phase must meet at one composition and temperature.

5. After crossing an invariant point, a phase boundary must extrapolate into a two-phase field.
6. Single-phase fields cannot be in contact along a horizontal line.
7. A single-phase phase should not be sub divided by a single line.
8. For binary systems, an invariant temperature line should always have equilibrium among three phases.
9. In between two single-phase fields should be a two-phase field.
10. Two phase boundaries should touch at the extremity of temperature.
11. A liquidus and solidus must have a horizontal common tangent at a congruent point.
12. In the lower part of a single-phase field, a local minimum point must contact an additional boundary.
13. In the lower part of a single-phase field, a local maximum point must be drawn with either a monotectic, monotectoid, syntactic or syntectoid reaction occurring below it.
14. A phase boundary must not end within a phase field.
15. An invariant reaction within a binary system must be at a constant temperature.
16. At the melting point of a compound, a liquidus must not have a discontinuous sharp peak.
17. At an invariant reaction, the compositions of all three phases must be different.
18. In a binary system, a four-phase equilibrium is forbidden.
19. A two-phase field between two phases in equilibrium must not have their phase boundaries cross.
20. The liquidus line cannot be too asymmetrical.
21. If the liquid curve is regarded as an ideal solution, then the tolerable change of the liquidus slope can be examined by the Arrhenius plot of $\ln X$ vs. $1/T$.
22. The shape of the miscibility gap at its critical point is round.
23. The steepness of the liquids line is related to the stability of the compound at low temperatures.
24. The critical point of a liquid miscibility gap has a composition usually found in the center range of the phase diagram.
25. Two compounds of similar compositions should not coexist over a wide temperature range.

These guidelines allows for one to check the validity of a proposed phase diagram, and have been used in the current research to determine the validity of the proposed phase diagrams in the literature of the LiCl-KCl-UCl₃ system.

2.2.3. LiCl-KCl System

The LiCl-KCl system is the most studied binary system of the ternary system of interest. Both LiCl and KCl crystallize in the rock-salt structure. In this structure, the chlorine ions occupy the octahedral holes of the cubic closed packing array of the Li or K ions. The coordination around the cations and anions in these structures is six.[82] Upon melting pure LiCl or KCl, the molten salts retain their octahedral structures.[87, 88] When melting LiCl and KCl together, it has been predicted that the Li coordination number decreases to four, while the KCl remains at a six coordination.[89] Various researchers reported phase diagrams that are in good agreement with one another with a eutectic temperature to be between 625-634 K and a eutectic composition between 57.0-59.5 mol% LiCl.[17-28, 90]. Older experimentation relied on visually examining the phase behavior during heating and cooling to determine the melting temperatures [17-23], while newer reports use differential thermal analysis (DTA), or differential scanning calorimetry (DSC) to determine the eutectic and melting temperatures, and modeling to assess the reliability of the data [24-28, 90]. Only taking into consideration the data from DSC, DTA, and calculations, the literature shows a eutectic temperature 625-628 K with a eutectic composition range of 58.2-59.5 mol% LiCl. [24-28, 90]

2.2.4. LiCl-UCl₃ System

The LiCl-UCl₃ system was only studied a few times. The UCl₃ crystallizes in what is called the UCl₃ structure. In this structure, the U ion is coordinated by nine Cl⁻ ions, and is in a tricapped trigonal prismatic structure.[91] Upon melting, the coordination number decreases from nine to six. [92] Studies of the LiCl-UCl₃ were first performed by Barton *et al.* Barton published a phase diagram compiled from examining 17 samples of various LiCl-UCl₃ compositions.[29] Although, the method of thermal analysis was not discussed, Barton reported a single eutectic at 25 mol% UCl₃, and 768 ±5 K.

Desyatnik *et al.* studied this same system using cooling curve data from DTA, and reported a eutectic composition at 26.5 mol% UCl_3 and a melting temperature of 763 ± 2 K.[30] Ghosh *et al.* used Gibb's energy modelling to calculate the LiCl-UCl_3 phase diagram from Barton, and Desyatnik's data. Ghosh reported a single eutectic at 24.2 mol% UCl_3 with a melting temperature of 765 K. Due to the limited experimental information available on the LiCl-UCl_3 system, this phase diagram was the first to be investigated in this study.

2.2.5. KCl-UCl_3 System

The KCl-UCl_3 system is more complex than the LiCl-UCl_3 system. This system has been studied many times, with each study resulting in a phase diagram displaying contradictory data for the eutectics, congruent melting compositions, and number of phases formed. Kraus was the first to study this system.[31] He determined phase transitions by slowly cooling samples and recording the temperatures with a recording potentiometer. Kraus concluded that, while some samples contained a considerable amount of error due to supercooling, most samples only contained a ± 5 K error. The samples of UCl_3 were reported to contain small quantities, $< 0.5\%$, of UCl_4 . The resulting phase diagram showed two eutectic compositions, one at 20 mol % UCl_3 with a melting temperature at 863 ± 5 K, and one at 50 mol % UCl_3 with a melting temperature at 818 ± 5 K. In compositions with less than 33.3 mol % UCl_3 , Kraus reported that the appearance of two thermal effects upon cooling. The first thermal effect was attributed to the K_2UCl_5 phase. K_2UCl_5 has an orthorhombic structure, with UCl_7 existing in monocapped trigonal prisms that are edge sharing with UCl_5^{2-} chains. [93] The second thermal effect gives rise to the existence of the K_3UCl_6 phase, which was not isolated to allow for characterization. This significant difference from Kraus's diagram. The thermal analysis and the maximum gradient of 25 mol \% UCl_3 [94] to collect data for Thoma's diagram. Thoma expressed that excess uranium metal was introduced to the compositions tested to minimize the presence of U^{4+} , which Thoma believes caused the K_3UCl_6 phase in Kraus' diagram. Thoma stated that when the excess uranium was not present, the melts behaved identical to the melts reported by Kraus. This excess uranium metal resulted in Thoma actually studying the $\text{U-UCl}_3\text{-KCl}$ ternary system. Two eutectics were reported at 19 mol UCl_3 and 55 mol % UCl_3 melting at 833 K and 826 K. There was no evidence supporting the existence of K_3UCl_6 . Thoma did, however, report

on a “eutectic break” occurring in compositions with UCl_3 greater than 55 mol %. The reason for this “eutectic break” is unknown. [94]

Desyatnik *et al.* reported studying the KCl-UCl_3 system with DTA and x-ray diffraction (XRD). It is assumed that cooling data was used to construct the phase diagram, as this technique was used by Desyantik for determining the LiCl-UCl_3 system. The compound K_2UCl_5 was reported with two eutectic compositions. E_1 was found at 16 mol % UCl_3 melting at 863 ± 2 K, and E_2 at 50 mol % UCl_3 at 816 ± 2 K. [32]

Suglobova *et al.* used thermographic studies and XRD to explore the alkali metal (M) chlorides with UCl_3 . Cooling curves were used to determine phase equilibria of samples in contained quartz ampules. The samples were then analyzed by XRD to observe the stable phases after thermal cycling. Suglobova explained that the hexahalouranates (M_3UCl_6) melt congruently, and decompose to the pentahalouranates (M_2UCl_5) and an alkali halide. Suglobova’s diagram displays a break in the composition of the compound K_3UCl_6 , which is attributed to possible solid solution formation. Suglobova’s diagram suggests solid solution formation for K_3UCl_6 and decomposition of that phase to K_2UCl_5 and KCl at low temperature. If this decomposition occurs, an invariant line must extend from KCl past the decomposition point of K_3UCl_6 to the K_2UCl_5 phase. As drawn, this diagram violates phase rules. If the line separating the two two-phase regions is a boundary line, then this line cannot be horizontal. In addition, two two-phase regions cannot bound each other because a degree of freedom is introduced by this line. [86] Suglobova’s break in the K_3UCl_6 phase displays two solubility values for a phase boundary at 743 K. Two eutectics are reported at 22 mol % UCl_3 and 50 mol % UCl_3 melting at 863 and 813 K, respectively. While the K_2UCl_5 was characterized by XRD and its melting point determined, no such data were determined for the K_3UCl_6 making its existence questionable. [33]

Ghosh *et al.* reexamined the KCl-UCl_3 system using computer modeling of phase diagrams (CALPHAD) with Kraus, Suglobova, and Thoma’s data. Due to the lack of XRD data of the K_3UCl_6 phase, Ghosh assumed the phase does not exist, and did not include it in the calculations. Ghosh computed two eutectic compositions at 18.6 and 54 mol % UCl_3 melting at 847 and 831 K, respectively. [28]

While the literature does agree on the presence of two eutectics in the KCl- UCl_3 system, the exact composition of these eutectics and their melting temperatures are inconsistent. Furthermore, the existence of K_3UCl_6 is inconclusive. These discrepancies result in the dire need for the KCl- UCl_3 system to be re-examined experimentally using newer, more accurate techniques, such as differential scanning calorimetry

2.2.6. LiCl-KCl- UCl_3

The literature available for the ternary system is very limited. The coordination of the U^{3+} ion in the LiCl-KCl electrolyte was found to be mainly six, with U^{3+} in the coordination cage fluctuating between six and seven.[95] Thamer was the first to investigate the ternary system. Data from the DTA cooling were used to determine the phase transitions. Thamer claimed that supercooling was overcome by agitating the samples above 973 K through an arc of 30 K at two cycles per second. Thamer also added additional uranium metal in a ratio of $\text{U}^0/\text{U(III)} = 0.20$ to ensure the absence of UCl_4 , meaning Thamer actually studied the U- UCl_3 -LiCl-KCl system. Thamer was only interested in samples of high uranium concentrations because the objective of his work was to understand salt phases that would yield a high breeding ratio for molten salt reactors. One eutectic was identified in the system at 691 ± 2 K at 46% LiCl- 24% KCl- 30% UCl_3 with the solidifying phases consisting of LiCl, KCl, and UCl_3 . [30] Desyatnik et al. [31] studied the ternary system by heating samples of various compositions in quartz closed tubes until the samples were melted, followed by cooling at a rate of 3-6 K min^{-1} , and simultaneously recording the processes occurring during cooling on photographic paper. The ternary system was calculated from liquidus transitions of the LiCl-KCl [20], LiCl- UCl_3 [32], and KCl- UCl_3 [30] binary phase diagrams. Desyatnik determined four solidifying phases consisting of LiCl, KCl, K_2UCl_5 and UCl_3 . This ternary system was divided by a triangulating section of LiCl- K_2UCl_5 which divided the diagram into two secondary subsystems consisting of LiCl- K_2UCl_5 - UCl_3 , and LiCl-KCl- K_2UCl_5 . The LiCl-KCl- K_2UCl_5 system was reported to be a simple eutectic system with the eutectic composition of 29.5 mol% LiCl, 58.5 mol% KCl, 12 mol% UCl_3 melting at 608 ± 2 K. The LiCl- K_2UCl_5 - UCl_3 system was reported to have a eutectic composition of 38 mol% LiCl, 30.5 mol% KCl, and 31.5 mol% UCl_3 melting at 661 K. The work was performed to understand phases formed during accidental cooling of an

electrorefiner salt; therefore, the scope of the work was to determine the highest temperature at which the salt would begin to freeze. Twenty samples were investigated using heating curves from DTA and XRD. Nakayoshi concluded that the diagram consists of two boundary lines, one connects to the LiCl-K₂UCl₅ system, and the other line connects to the LiCl-KCl eutectic- 17mol% UCl₃. The two eutectics Desyatnik reported were also investigated in this study. The first eutectic was not found, and the second eutectic was reported to have a slightly different composition, with a melting temperature that did not correspond to Desyatnik's reported temperature. Because the scope of this work was to determine the temperature at which the electrolyte would crystallize during accidental cooling of the electrorefiner, the exact eutectic temperatures and compositions were of interest, and thus were not reported. [16]

The ternary system was also investigated by Ghosh *et al.* Two compositions of the LiCl-KCl eutectic with varying UCl₃ compositions were examined by DTA and DSC using heating curve data. Ghosh used CALPHAD to calculate the ternary diagram with data from Nakayoshi, Thamer and his DSC/DTA experiments, and the enthalpy of mixing calculated from the surrounded ion model. The projected liquidus diagram was reported to be close to Desyatnik and Nakayoshi's findings. Ghosh reported two eutectic compositions, E₁, at 45.6 mol% LiCl, 21.5 mol% KCl, 33.1 mol% UCl₃ melting at 702 K, and E₂ at 57.6 mol% LiCl, 41.9 mol% KCl, and 0.468 mol% UCl₃ at 625 K. A monovariant eutectic reaction was also reported at 746 K with the LiCl-KCl eutectic and 18 mol% UCl₃. [28]

While all reports agree that the liquidus ternary diagram consists of two boundary lines, one for the LiCl-K₂UCl₅-UCl₃ system, and the other of the LiCl-KCl-K₂UCl₅ system, the eutectic compositions and temperatures reported for these systems were contradictory. This ternary system is of the utmost importance for understanding the electrolyte used in the electrorefiner. However before the ternary system could be studied, the binary systems of LiCl-UCl₃ and KCl-UCl₃ must be evaluated.

2.3. Neptunium Trichloride Chemistry

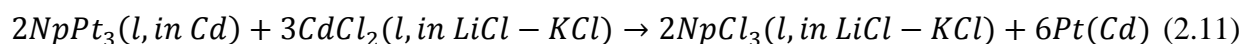
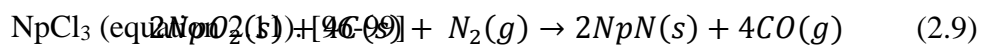
Complex phases containing transuranics impact the performance of the electrorefining system by influencing the chemical activity of the actinides in the molten

salt electrolyte and thus the redox potentials of the actinide chlorides in the molten salt solution. The thermodynamic activity of the transuranic elements will affect the transuranic-lanthanide separation factors thus, studies performed on the behavior of transuranic elements are essential for predictive modeling and interpretation of the results of electrorefining experiments. Limited experimental thermodynamic studies have been performed regarding the behavior of the transuranic elements in the LiCl-KCl system. Upon beginning the study of the neptunium chlorides in the LiCl-KCl system, it was quickly realized that information available for the neptunium chlorides was lacking. Unlike uranium and plutonium chlorides, preparation, characterization, and thermodynamic properties have not been extensively studied. With regard to the thermodynamic data for neptunium chlorides, most of the data is extrapolated from thorium, uranium, and plutonium compounds. Of the available resources on the neptunium chlorides, some were contradictory, while most were confirmatory. Because of the scarcity of data and contradictions within the available information, a thorough investigation of the available information on the neptunium chlorides was performed.

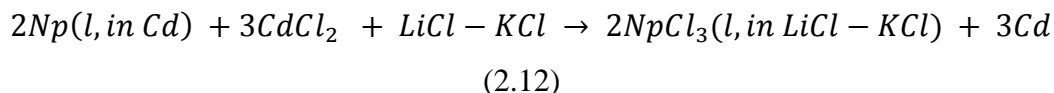
2.3.1 Synthesis of NpCl₃

Multiple methods have been employed for the synthesis of solid NpCl₃. These synthetic methods include chlorination of the metal, carbothermic reduction of the oxide followed by chlorination, etc. It is imperative to have multiple procedures for the production of neptunium chloride due to the limits on the resources available to an experimenter, the quality and/or quantity of product needed and its intended use, and the some. In 2001, Shirai *et al.* synthesized NpCl₃ by the chlorination of NpPt₃ with CdCl₂.

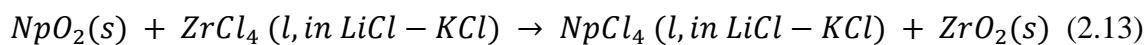
They mixed NpO₂ with graphite in N₂-8% H₂ mixed gas stream at 1823 K to produce NpN (equation 2.9). The resulting NpN was combined with platinum powder and heated at 1073 K to yield NpPt₃ (equation 2.10). Finally, the NpPt₃ was dissolved into liquid cadmium and reacted with CdCl₂ contained in LiCl-KCl eutectic salt at 773 K to produce NpCl₃ (equation 2.11).



A similar mechanism, utilized by multiple authors, started with Np metal, and dissolved the Np in Cd, to form an alloy. The alloy phase was contacted with LiCl-KCl containing CdCl₂ at 723-773 K resulting in the oxidation of Np to form NpCl₃. [100, 101]

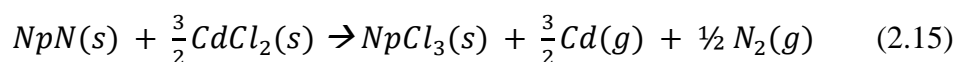


An additional method of NpCl₃ synthesis is the reaction of NpO₂ with ZrCl₄ contained in the LiCl-KCl eutectic electrolyte. This process, demonstrated by Sakamura *et al.*, chlorinated NpO₂ with ZrCl₄ in the LiCl-KCl eutectic salt at 773 K. Zirconium metal was added to the system to reduce NpCl₄ to NpCl₃. [102]:



In all of these synthetic approaches, the final product NpCl₃, is dissolved in the LiCl-KCl. These methods are appropriate when the NpCl₃ is required to be dissolved in the eutectic LiCl-KCl electrolyte, such as when performing electrochemical measurements. If pure NpCl₃ is the objective, without the electrolyte, these approaches are less than desirable due to the impracticality of removing the LiCl-KCl from the NpCl₃.

Recently, the synthesis of NpCl₃ from NpN and CdCl₂ was demonstrated by Hayashi and Tankano [103]. The NpN was synthesized using the same carbothermic reduction of NpO₂ as used by Shirai [97, 98]. The NpN was then reacted with CdCl₂ at a 1.56 CdCl₂:NpN ratio at 738 K under vacuum. The synthesis equipment contained a water-cooled cold finger, set in the furnace, to capture cadmium vapor produced by the reaction:

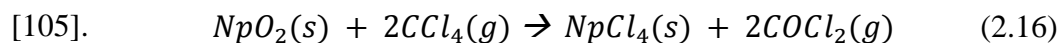


Nitrogen gas was evacuated from the system, and the system was then heated to 700 K to remove any residual CdCl₂. [103] Hayashi reported synthesizing a highly pure product with a yield of nearly 100%.

The synthesis of anhydrous actinide trichlorides from aqueous solutions was proposed by Foropoulus in 1992, and used for the production of PuCl₃ [104]. An aqueous solution of plutonium chloride was reacted with a reducing agent, such as hydroxylamine

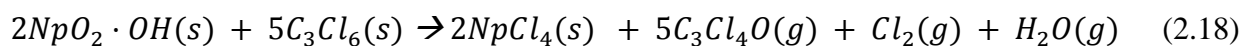
hydrochloride, to reduce any PuCl_4 in the solution to PuCl_3 . The solution was then evaporated to a crystalline plutonium trichloride hydrate. The product then underwent reflux distillation with $\text{SOCl}_2(l)$ at about 340 K to dehydrate the trichloride. The PuCl_3 was then placed in a vacuum furnace at 773 K to remove trace SOCl_2 . The overall process resulted in a 97% yield of high purity PuCl_3 . [104] Unfortunately, this procedure was never implemented for the synthesis of NpCl_3 . As this approach was suggested to be applicable for NpCl_3 , the reduction of the neptunium in aqueous solution is much more complicated than the reduction of plutonium since plutonium is much more stable in the 3^+ state, and Np is much more stable in the 4^+ state. Thus, it is unclear if this synthesis pathway would yield neptunium trichloride.

Multiple methods have been demonstrated for the synthesis of $\text{NpCl}_4(s)$. One method contacts neptunium oxalate or neptunium dioxide with $\text{CCl}_4(g)$ at 773 K. The NpCl_4 forms, and is sublimated, for purification purposes, at temperatures below 809 K. This method, developed by Fried and Davidson in 1951, generates phosgene, which serves as a supplemental chlorinating agent for any oxide that is unreacted in the system



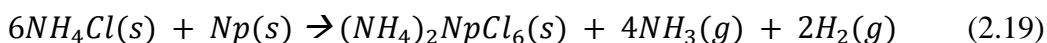
In 1968, Charporov and Chudinov reduced the temperature of the synthesis to between 553-678 K, to eliminate the immediate sublimation of the NpCl_4 . [106] The final tetrachloride product was, however, sublimated under vacuum at 633-653 K for purification. Yet another method of NpCl_4 production, developed by Bagnall and Laidler in

1966, involves reacting $\text{NpO}_2 \cdot \text{OH}$ with hexachloropropene, and heating under reflux:

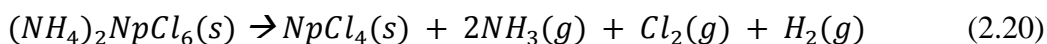


After sublimating the crude product at 923 K, the NpCl_4 product was found to be pure, but the method only gave a 50% yield of pure NpCl_4 . [106, 110, 111]

Currently, the synthesis of NpCl_4 from Np metal and NH_4Cl is being investigated. As this is an effective method for synthesizing UCl_4 , [57] it is anticipated that this process will be applicable to synthesizing NpCl_4 . It is postulated that in this synthetic method, NH_4Cl and Np metal upon heating to 573 K form an intermediate complex [57]:



The intermediate is then heated above 623 K under vacuum to decompose it to the final tetrachloride product:



When using this method to synthesize UCl_4 , the intermediate was found to decompose at 593 K. The neptunium intermediate complex is expected to decompose at a similar temperature.[57]

Polovov *et al.* synthesized $NpCl_4$ from a Np (VI) stock solution in 1 M HNO_3 . The solution was reacted with 6 M NaOH, which precipitated $NpO_2OH \cdot xH_2O$. The precipitate was then dissolved in 1 M HCl to form NpO_2Cl , and HI was added to reduce the Np(V) to Np(IV). UV-VIS-NIR spectroscopy confirmed the reduction occurred. The solution was then evaporated, and the residue was dissolved in water. Next, the solution was reacted with 6 M NaOH, which formed the precipitate $Np(OH)_4$. The precipitate was then dissolved in 1 M HCl. The resulting product was aqueous $NpCl_4$. The solution was purged with argon and heated to remove the hydrate.[112] Polovov bubbled HCl through the final product to remove any residual neptunium oxides. Other than UV-VIS, no other analytical measurements of the product were taken, which calls into question the purity of the $NpCl_4$ produced. Depending on the purity of the final product, this method may be applicable to synthesizing $NpCl_4$ from an aqueous solution.[113]

To reduce $NpCl_4$ to $NpCl_3$, Fried and Davidson used a mixture of hydrogen gas and $CCl_4(g)$ at 623-673 K. [105, 114] More recently, Masset and Apostolidis reduced $NpCl_4$ with hydrogen gas at 723 K, and produced a high yield of $NpCl_3$ [107]



Fried synthesized $NpCl_3$ by directly chlorinating NpO_2 at 573-673 K in the presence of H_2 and CCl_4 . He reported a very high yield of $NpCl_3$ due to the intermediate compound (i.e., $NpCl_4$) remaining in the effective reaction zone in this temperature range, and not sublimating. Overall, Fried maintained that a larger yield of $NpCl_3$ is obtained from the direct chlorination of the NpO_2 rather than the reduction of $NpCl_4$. [105]

Another process, developed by Brown and Edwards, was the reduction of $NpCl_4$ to $NpCl_3$ with excess zinc. The method yielded 98% of $NpCl_3$ product. Excess zinc and $ZnCl_2$ were removed from the system via sublimation at 1223-1273 K under a high vacuum.[115]

2.3.2. Structure of NpCl₃

The crystal structure of NpCl₃ has been thoroughly investigated. NpCl₃ exhibits a nine-coordinate UCl₃-type structure existing in a C_{6h} point group and a C_{63/m} space group in which the site symmetry of the neptunium ion is C_{3h}. [108, 115, 116] X-ray diffraction characterized NpCl₃ as hexagonal with two molecules per unit cell. [108] This structure is published in figure 2.6. The published lattice parameters of NpCl₃ are presented in table 2.1. Fried used these dimensions to calculate a density of 5.58 g cm⁻³. [105] Brown also used these parameters to determine the molecular volume of NpCl₃ to be 101.8 Å³. [115]

Carnall *et al.* performed an extensive study of the absorption spectra of NpCl₃. The study gives the energies of the observed absorption bands in NpCl₃ at 4 K as well as all of the spectra for Np³⁺:LaCl₃. The absorption spectra of NpCl₃ revealed that on average there is a slightly greater interaction between the 5f electrons and the Cl⁻ ion in the NpCl₃ than U³⁺ in the structure of the 9-coordinate UCl₃ type. [108]

2.3.3. Enthalpy of Formation

The enthalpy of formation of NpCl₃(s) was estimated by various sources and these values are given in table 2.2. Westrum *et al.* first determined the heat of formation of the trichloride by the extrapolation of the experimental data, found using calorimetry, for the heats of a formation of UCl₃, PuCl₃, and ThCl₃, in aqueous solutions, as a function of ionic radius and hydrogen ion concentration. Westrum dissolved neptunium metal in HCl, to oxidize it, and measured the evolution of hydrogen gas. By comparing the hydrogen evolution of Np metal to that of U, and Th metal, Westrum was able to determine a heat of formation of NpCl₃ not only based on ionic radius. [117] Details of the apparatus designed by Westrum *et al.* to determine hydrogen concentration is reported in reference [118]. Fuger *et al.* used a similar method to estimate the enthalpy of formation; however, they only interpolated values as a function of the ionic radii of actinides. Because the heat of formation was not plotted as a function of hydrogen ion concentration as well, there is additional error when extrapolating. Fuger reported a value of about 6 kJ mol⁻¹ less than that of Westrum. [106]

Lemire *et al.* estimated the enthalpy of formation of NpCl₃ by plotting the difference in enthalpy of formation for the uranium and plutonium halides: $\Delta H_f^\circ(\text{MCl}_{3,c}, 298.15 \text{ K}) - \Delta H_f^\circ$

(MBr_{3,c}, 298.15 K) and interpolating to estimate the enthalpy of formation for NpCl₃.

Lemire then took this value and Fuger's value to calculate a mean value for the heat of formation of the trichloride, which is reported table 2. [119]

Bratsch *et al.* used a modified ionic model to calculate the enthalpy of formation. As a result of their calculations, they came to the realization that the energy contribution from covalent bonding comes from so-called environmental effects due to the greater expansion of the actinide's 5f orbital, and not just from the ionic radius. Since their model only accounted for ionic radii, and not the environmental effects, in the calculation of the energy contribution, they noticed that their calculated enthalpy of formation data for the actinide chlorides were consistently 20 kJ mol⁻¹ less than the literature values. Taking into account their 20 kJ mol⁻¹ error, one would calculate a value 901 kJ mol⁻¹, which is close to the value determined by Westrum. [120]

Ionova calculated the heat of formation by adding covalence contributions to a simple ionic model. Ionova claimed that the larger spatial expansion of the 5f and 6d orbitals causes a greater charge density and larger overlap with ligands, which leads to greater covalence contributions. [116] Although Ionova shows this trend with the actinide tribromides, and triiodides, it is less apparent for the actinide chlorides and fluorides. The enthalpy of formation calculated using this model is much lower than that reported in the other literature. The energy contribution calculated from the covalent effects appears to be too small in the Ionova model.

Overall, the theoretical values based on interpolated data from the enthalpy of formation of the other actinide chlorides are in good agreement. The values that used the simple ionic model, but took into account a speculative covalent contribution, were not in agreement with these values.

2.3.4. Standard Entropy

The values found for the standard entropies of the neptunium chlorides are based on correlations with the other actinide chlorides. The values for NpCl₃ are reported in table 2.3.

To determine the standard entropy of NpCl₃, Kubaschewski *et al.* used the revised Latimer method, which sums the standard entropy contribution of the constituent ions to

give the entropy of the compound. The neptunium atom contribution was established from the standard entropy of NpO_2 and NpF_3 . [121]

Rand *et al.* estimated the entropy by adding the spin-only contribution of the extra electron ($R \ln(5/4)$) to the standard entropy of UCl_3 (method 1). [122] Rand *et al.* also assumed the entropy of NpCl_3 to be the same as UCl_3 and incorporated the entropy difference between UCl_3 and PuCl_3 to determine the standard entropy of NpCl_3 , (method 2). Kubaschewski's reported value is only about $2\text{-}4 \text{ J K}^{-1} \text{ mol}^{-1}$ higher than the values found by Rand's methods, and is considered to be in good agreement with Rand's data.

Fuger *et al.* also estimated the standard entropy of NpCl_3 by extrapolating from a linear fit of the UCl_3 and PuCl_3 entropies. According to Fuger, the difference in the entropy of these compounds is attributed to the spin-only contribution of the unpaired electrons. Fuger's entropy is in good agreement with Rand and Kubaschewski's values. [120] Konings *et al.* selected values that were taken as the sum of the lattice entropy S_{lat} and the excess entropy S_{exs} . The S_{lat} values were estimated from UCl_3 and the S_{exs} values were calculated from known crystal field levels. Konings' entropy is in good agreement with the previous author's findings. [123]

2.3.5. High Temperature Heat Capacity

The heat capacity of solid NpCl_3 was estimated multiple ways by various authors. The results of the findings for NpCl_3 are given in table 2.4.

Rand *et al.* hypothesized that the heat capacity for NpCl_3 was similar to UCl_3 . [122] Konings *et al.* took the sum of the lattice heat capacity and the excess heat capacity to determine the standard heat capacity. [123] Krestov used a method in which calculation of the specific heat of ionic crystals was applied to the sum of the temperature dependence of the cations and anions. [124]

2.3.6. Vapor Pressure and Melting Temperature

There is a lack of information on the vapor pressure and melting temperature of NpCl_3 . The reported values for the melting temperature and vapor pressure of NpCl_3 are given in Table 2.5. The vapor pressure for NpCl_3 was assumed by Rand *et al.* to be the mean of the vapor pressure of UCl_3 and PuCl_3 , as there are no available measurements of the vapor pressure of NpCl_3 . The

first equation, for the temperature range 900-1075 K, is for the solid-vapor equilibrium (sublimation) of NpCl_3 , and the second equation pertains to the liquid-vapor equilibrium (vaporization) of NpCl_3 from 1075- 1300K. [122]

To determine the melting point of NpCl_3 , Rand *et al.* extrapolated from the values for UCl_3 (1115 K) and PuCl_3 (1041 K). [122] Fried reports that NpCl_3 melts “over a considerable range in the neighborhood of 1073 K”. [105]

2.4. Figures

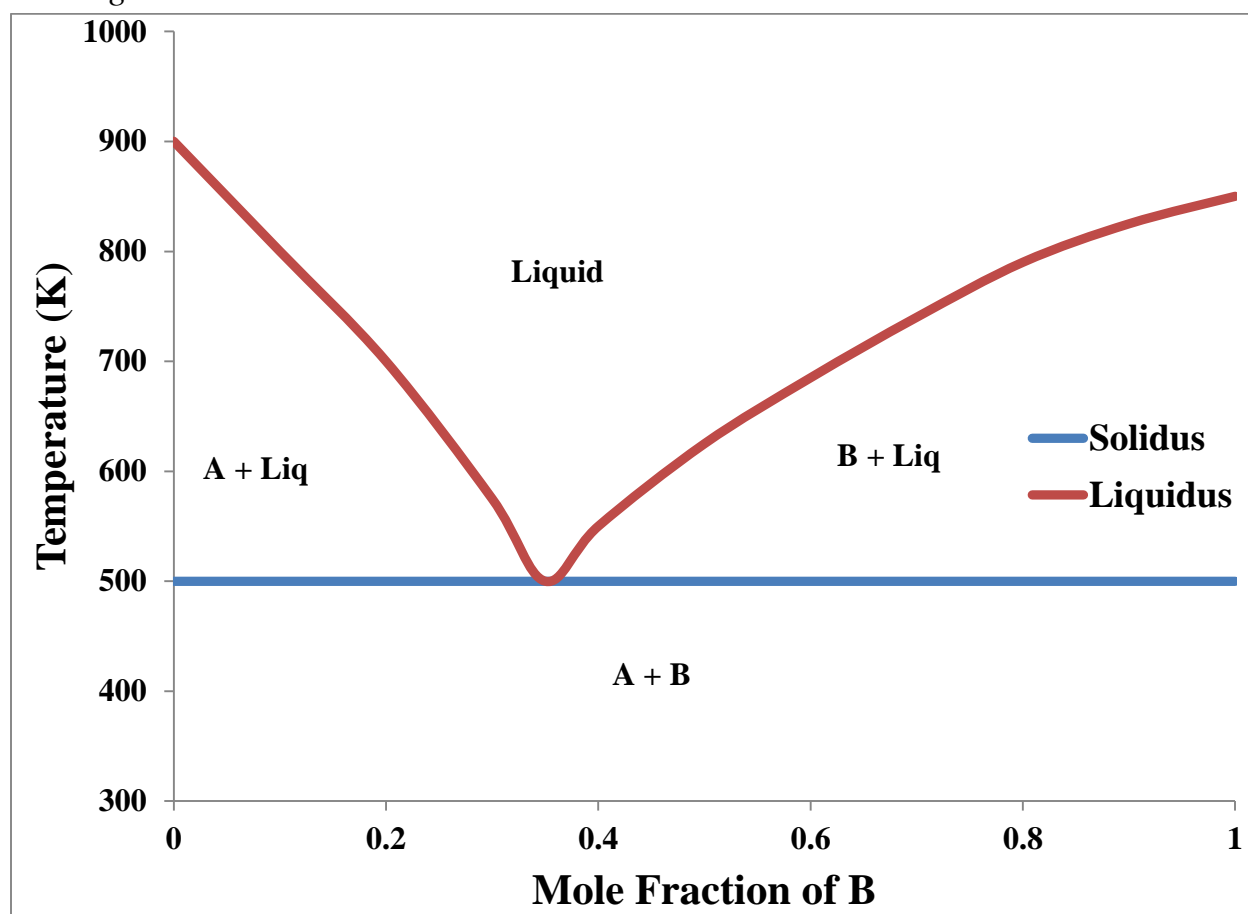


Figure 2.1 An example of a binary phase diagram of components A and B of a simple eutectic

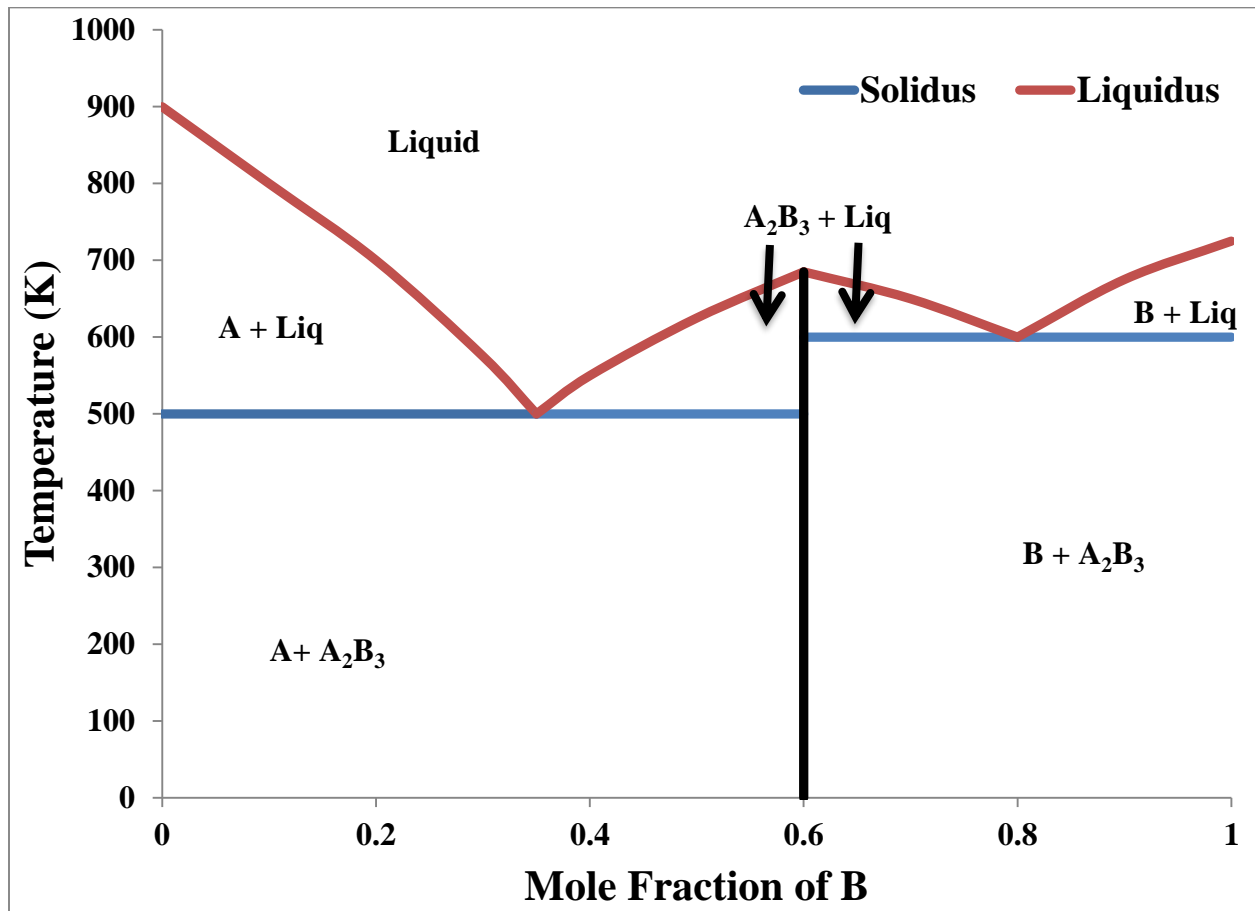


Figure 2.2 An example of a binary phase diagram of components A and B with a congruently melting intermediate compound

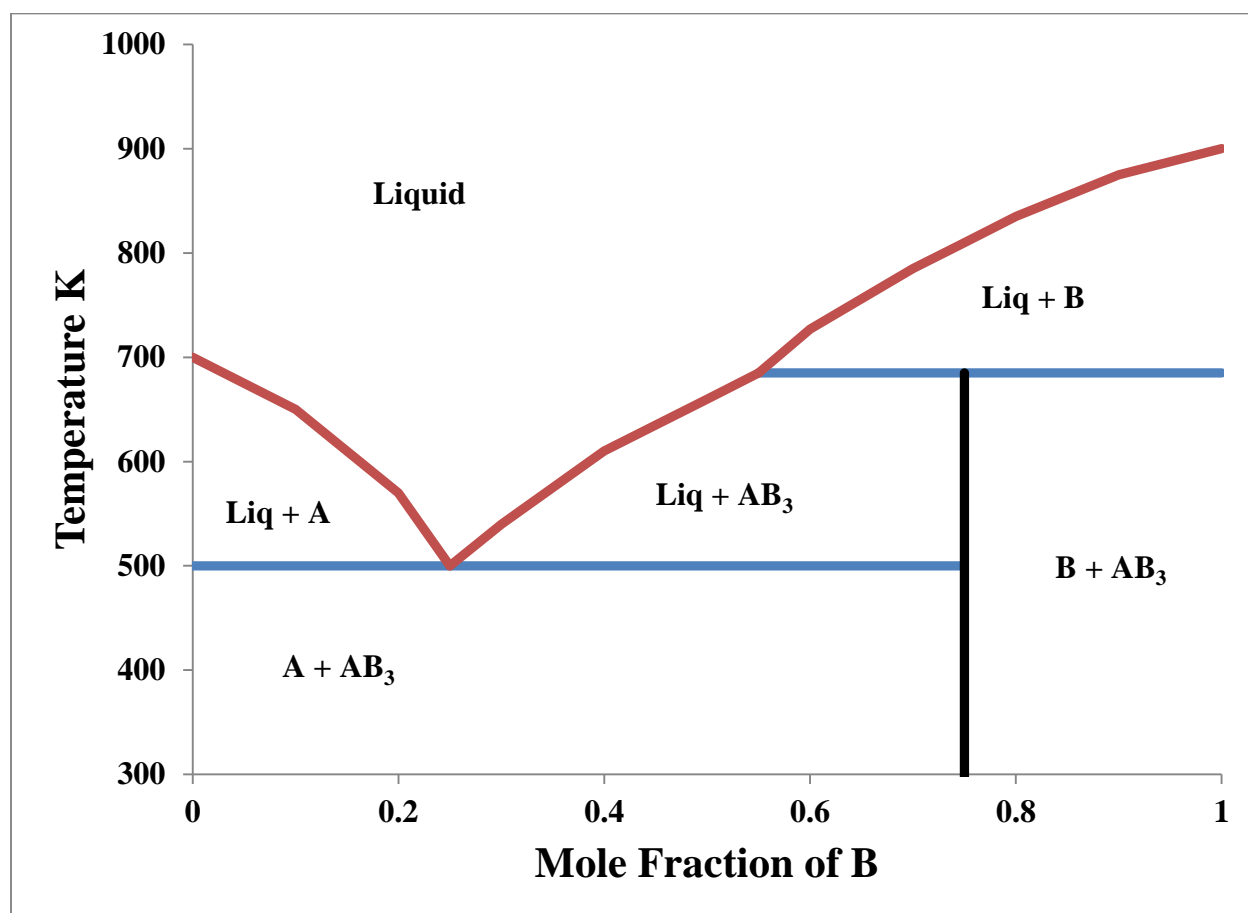


Figure 2.3 An example of a binary phase diagram of components A and B with an incongruently melting intermediate compound

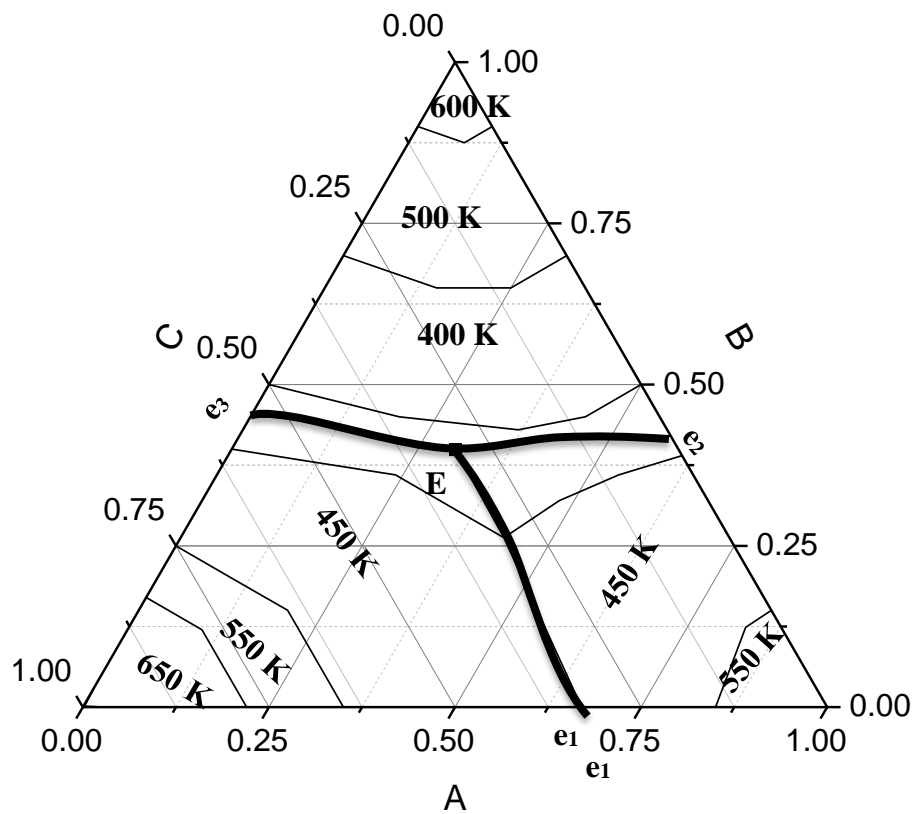


Figure 2.4 An example of a ternary phase diagram of components A, B, and C with two binaries consisting of simple eutectic systems and one binary consisting of a congruently melting compound

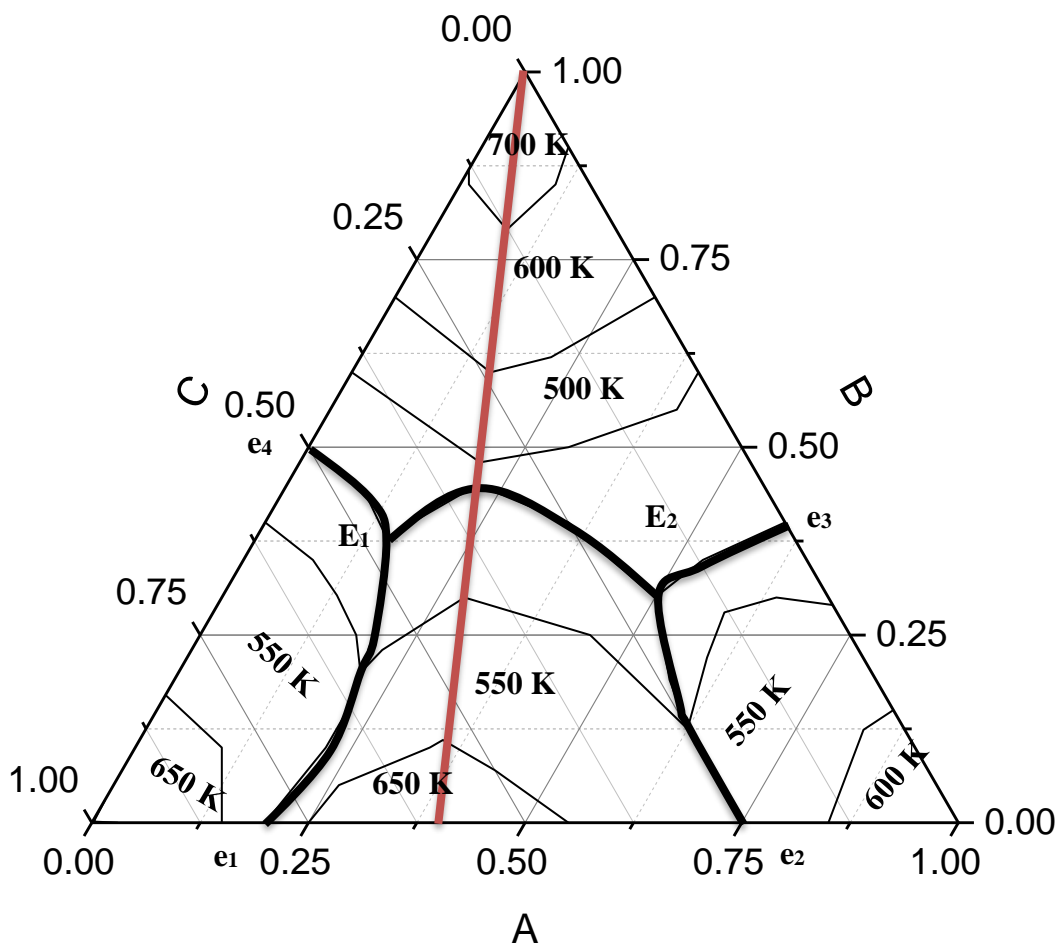


Figure 2.5 An example of a ternary phase diagram of components A, B, and C with the binaries only consisting of simple eutectic systems

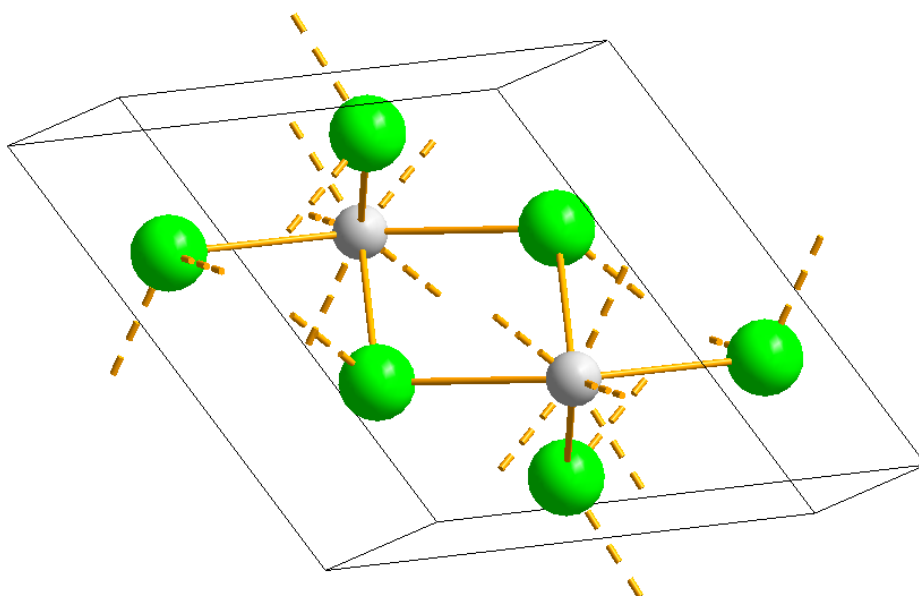


Figure 2.6 The crystal structure of NpCl_3 . The white circles represent neptunium, while the green circles represent chlorine.[125]

a_1 (Å)	c_0 (Å)	Source
7.405 ± 0.01	4.273 ± 0.005	Fried [105]
7.413 ± 0.01	4.282 ± 0.001	Brown [115]
7.420	4.282 \AA	Carnall [108]

Table 2.1 Lattice parameters for NpCl_3 based on various sources.

Enthalpy of formation kJ mol^{-1}	Source
-904 ± 4	Westrum [117]
-868	Ionova [116]
-898.3	Fuger [106]
-895.3	Lemire [119]
-881	Bratsch [120]

Table 2.2 Enthalpy of formation for NpCl_3 at 298 K estimated by various authors

Standard Entropy J K ⁻¹ mol ⁻¹	Source
162.9	Kubaschewski [121]
160.0	Rand [122](method 1)
158.4	Rand [122](method 2)
161.2	Fuger [106]
165.24	Konings[126]

Table 2.3 Standard entropy for NpCl₃ at 298 K estimated by various authors

Heat Capacity J K ⁻¹ mol ⁻¹ (298.15-1000 K)	Heat Capacity at 298.15 K J K ⁻¹ mol ⁻¹	Source
$89.6 + 27.5 \times 10^{-3}T + 3.6 \times 10^5 T^{-2}$	101.9	Rand [122]
$94.6 + 3.3 \times 10^{-2}T$	104.4	Krestov [124]
$89.598 + 27.5 \times 10^{-3}T + 83.712/T^{-2}$	97.8	Konings [123]

Table 2.4 Heat capacity for NpCl₃ estimated by various authors

Vapor Pressure Log (p/bar)	T _{melting} K
$-15177/T + 9.057$ (900-1075 K)	1075 ± 30
$-12259/T + 6.346$ (1075-1300 K)	1073

Table 2.5 Fusion data for NpCl₃ vapor pressures and melting temperatures by Rand.[122] Second melting temperature by Fried [105].

3. Chapter 3: Experimental

3.1. Project 1. Investigation of Molybdate Melts as an Alternative Method of Reprocessing Used Nuclear Fuel

3.1.1. Materials

Nickel based alloys were tested for compatibility with the $\text{MoO}_3\text{-Na}_2\text{MoO}_4$ system as previous studies claimed to have used nickel while studying this oxide melt [11-13]. If Inconel was used as a crucible and basket material in the presence of MoO_3 , severe corrosion was observed. Preliminary tests also investigated a glassy carbon crucible; however, corrosion was observed after continued use in the presence of MoO_3 . Platinum displays good corrosion resistance in the MoO_3 , and thus was chosen for the crucible and basket construction. The in-house platinum crucible was 1.5” in diameter by 1.5” in height. The platinum mesh, used for the basket, was also an in-house material. The source of the uranium for the experiments was in-house depleted uranium oxide pellets, UO_2 . These pellets were crushed into smaller pieces before processing to allow for faster dissolution.

Fission product oxide simulants and Na_2MoO_4 were purchased from Sigma Aldrich. The MoO_3 was purchased from MP Biomedicals. The oxides and molybdates were ground into a homogeneous mixture with a mortar and pestle. The composition of the fission product oxide mixture used in the study is given in table 3.1. This composition is based on a calculated composition of fission products in used fuel, with an initial enrichment of 3.2%, after 33 MWd/kg burnup in a typical pressurized water reactor after 10 years of cooling. [127] Due to the difficulty in measuring such small quantities of the oxides in a glovebox, several fission product oxides (Tb, Dy, Lu and Er) are in a much higher concentration than what was calculated.

3.1.2. Molybdate Melt Studies

Experiments were performed in a vertical tube furnace inside an argon atmosphere glovebox with oxygen levels less than 10 ppm, and the moisture level between 3 and 50 ppm. The crucible contained six to seven grams of UO_2 and approximately fifteen grams of MoO_3 and Na_2MoO_4 in varying $\text{MoO}_3\text{:Na}_2\text{MoO}_4$ ratios. Figure 3.1 displays a flowchart of the basic separations process. A diagram of the experimental setup is shown in figure 3.1. The crucible was situated in the tube

furnace that was surrounded by Inconel heat shields. The temperature was monitored with a type K thermocouple.

For experiments to determine uranium phase information, UO_2 , Na_2MoO_4 , and MoO_3 were loaded into the crucible, which did not contain the basket. Samples were heated in the furnace at rate of about 300 K hr^{-1} until the temperature reached 1413 K, and held for about 8 hours, which allowed for the dissolution of UO_2 in the melt.

For experiments investigating fission product partitioning, UO_2 , Na_2MoO_4 , MoO_3 , and the fission product mixture were loaded into the basket and placed in the crucible. The mixture was heated at the same rate and to the same temperatures for the same amount of time, as the phase formation experiments. The melt continued in a closed furnace, so the possible release of gaseous fission products, such as RuO_2 , upon the dissolution of the simulated UO_2 fuel into the melt was not monitored. Upon cooling the melt to a pre-determined temperature in the range of 1073-1123 K, the platinum basket was lifted out of the crucible to allow for the physical separation of the uranium product from the fission products, which remained in the molybdate melt. The temperature was held at 1073-1123 K for about 10 hours to allow enough time for phase separation. Upon cooling the system to room temperature, the precipitate was recovered. After recovery of the precipitate from the basket, the product was washed with approximately thirty grams of liquid Na_2MoO_4 .

3.1.3. Composition of Uranium Product

To determine the composition of the main uranium-bearing product upon precipitation, experiments varying the composition of the melt of MoO_3 , Na_2MoO_4 , and UO_2 were performed. Samples of the uranium precipitate were analyzed using XRD to determine the composition of the uranium product resulting from the different compositions of the molybdate melts. After the samples were cooled in the furnace, the samples were transferred to a hood, ground with a mortar and pestle, washed several times with de-ionized (DI) water to remove excess molybdate melt, and air dried. A thin layer of the sample was placed on a glass slide covered with double sided tape to allow the precipitate to adhere to the slide, and then covered with a thin Mylar film. These slides were analyzed by XRD to identify the uranium-bearing phases; the experimental XRD spectra were compared to the powder diffraction database.[128]

3.1.4. Principles of X-ray Diffraction

X-ray diffraction is a key tool in determining the structure of many substances. XRD allows for bond lengths, bond angles and position of ions in a unit cell to determine the positions of the geometric structure of a solid substance. Powder X-ray diffraction was used for phase identification in these experiments. Powder XRD can also be used to determine lattice parameters and lattice type. When an X-ray beam strikes a powder sample, there is interference in the waves that occur due to the samples, the electrons elastically scatter the X-rays. As X-rays impinge on the crystal and the ordered atoms cause constructive interference, the diffraction intensity is at its maximum and a diffraction pattern occurs at an angle, θ , which corresponds to the distance between the planes of the atoms, d , in the crystal. The constructive interference occurs between the waves of the wavelength, λ , and the angle at which this occurs is given by Bragg's equation: [82]

$$2d \sin\theta = n\lambda \quad (3.1)$$

In this equation, n , is an integer, which represents an integral number of wavelengths. The intensity of the measured diffraction maxima is proportional to the square of number of electrons in the atom or ion. The resulting diffraction pattern characterizes the positions and types of atoms present in the crystal, and the diffraction angles and intensities give insight into the structure. [82]

In powder XRD, X-ray diffraction results in a cone of diffraction due to the large number of very small crystallites, which are present in powder samples. The angles of the diffracted beams are measured by the powder diffractometer. This detector scans the circumference of the circle surrounding sample, cutting through the cone of diffraction to measure the intensity of the scattered X-ray as a function of detector angle. Crystalline solids have unique powder XRD patterns due to the angles of reflections, and the intensities. The reflections and positions are influenced by the cell parameters, crystal system, and the wavelength used for data collection. The intensities are influenced by the position of atoms present, and the types of atoms that are present. Powder XRD allows for the detection of small quantities, as low as five to ten percent, of impurity phases in samples. [82]

3.1.5. Dissolution of Uranium Product for ICP-MS Analysis

Samples from the fission product partitioning experiments were transferred from the tube furnace to a fume hood after cooling. A NaOH wash was used to remove any residual molybdate salt from the precipitate. A 0.1M HNO₃ wash was used to remove any remaining fission products that could be present on the surface of the precipitate. Sodium molybdate is highly solubility in water, 65 g/100 g H₂O,[28] therefore deionized water with a resistivity $\geq 18 \text{ M}\Omega \text{ cm}$ was used to remove a significant portion of the molybdate salt present in the precipitate. The UO₂ precipitate was washed several times, and decanted with water. This water wash was performed several times. Sodium hydroxide was very effective for removal of molybdenum salts from the precipitate (>99.9% of all Mo present in the precipitate). Water and sodium hydroxide washes were both effective in the removal of remaining cesium. Cs₂MoO₄ formed upon the dissolution of Cs₂O in MoO₃ at temperatures exceeding 673 K, Cs₂MoO₄ is very soluble in water. To dissolve uranium molybdates (UMo₂O₈, UMo₇O₂₂, and UMo₁₁O₃₅), a combination of NaOH and H₂O₂ appeared to be most effective. Precipitates that were mostly UO₂ dissolved in HNO₃/H₂O₂ solutions. Elemental analysis of uranium containing precipitates was performed using inductively coupled plasma-mass spectroscopy ICP-MS (PerkinElmer SCIEX ELAN DRC II) with a reported uncertainty of +/-10%.

3.1.6. Principles of Inductively Coupled Plasma- Mass Spectrometry

Inductively coupled plasma mass spectroscopy allows for multi-element analysis in solutions with detection limits as low as parts per trillion. To produce an inductively coupled plasma, a current is driven through a cooled copper tube that acts as the induction coil. The current, oscillating through the coil, produces an oscillating electromagnetic field. A plasma discharge is started through a high voltage spark that seeds electrons through argon gas. The oscillating magnetic field accelerates the plasma. A sample is pumped in the sample introduction chamber, which consists of a nebulizer and a spray chamber. The nebulizer converts the sample to an aerosol. The spray chamber eliminates drops in the aerosol that are too large to vaporize in the plasma. When the aerosol drop enters the plasma, the solvent evaporates to leave a particle, which is vaporized, atomized, and ionized. The atoms and ions travel through the plasma to the sampling orifice of the mass spectrometer. When the ions flow through the sampling orifice, the

gas expands, and a skimmer samples a portion of this gas. As electrons diffuse in the plasma, a positive ion beam is formed, and a separation of charge occurs. The positive ion beam passes through a series of ion optics and a radio frequency only quadrupole lens that focuses the beam to the mass spectrometer. Ions are detected by their mass to charge ratio. [129]

3.2. Project 2. Phase Equilibria Studies of the UCl_3 and $NpCl_3$ in the LiCl-KCl System

3.2.1. Materials

High purity LiCl (99.999%) and KCl (99.998%) were purchased through Sigma Aldrich. For the synthesis of UCl_3 , in house uranium dendrites and anhydrous NH_4Cl (99.998%) purchased through Sigma Aldrich were used. For the synthesis of $NpCl_4$, in house neptunium nitrate was ignited at 973 K to produce NpO_2 . The NpO_2 was then reduced with Ca metal (Sigma Aldrich) in anhydrous $CaCl_2$ (Sigma Aldrich). Samples analyzed by differential scanning calorimetry (DSC) were contained in hermetically sealed gold pans purchased from TA Instruments.

3.2.2. UCl_3 and $NpCl_3$ Synthesis

Actinide trichloride synthesis was performed in an argon atmosphere glove box. A closed reaction vessel, pictured in figure 3.3, consisting of a closed quartz tube was placed in a jeweler's furnace with a thermocouple situated next to the quartz tube near the reaction zone. The open portion of the quartz tube was affixed to a large Pyrex tube which in turn was connected to a vacuum via a hose to trap any vapors produced during the reaction, and to allow for gas evolution without over pressurizing the system. The quartz tube and the Pyrex top were connected with a Viton O-ring that is designed to leak in the case of over-pressurization. Uranium dendrites or neptunium metal and anhydrous ammonium chloride were the starting materials.

3.2.3. Thermal Analysis of Samples

Mixtures of the synthesized UCl_3 and high purity LiCl, KCl, or LiCl-KCl, or $NpCl_3$ and KCl, were ground together with a mortar and pestle in an argon atmosphere glovebox. Samples were loaded into gold cells, and hermetically sealed using a cell press. The sample crucible was

loaded into the Netzsch STA 449 C Jupiter. The simultaneous thermal analysis (STA) combines the capabilities of differential thermal analysis (DTA), differential scanning calorimetry (DSC) and thermogravimetric analysis (TGA). The sample crucible was situated on a platinum sample carrier with a type S thermocouple. An empty gold hermetically sealed crucible was stationed on the other side of the sample carrier to serve as the reference crucible. The samples were thermally cycled three times. The first thermal cycle was completed at a rate of 20 K min⁻¹ to initiate melting, and ensure sample homogenization. The following thermal cycles were completed at a rate of 5 K min⁻¹ to identify transition temperatures of the material. Only data from the heating curves were used for transition temperatures, as the cooling curves displayed supercooling. The composition of the samples analyzed with the DSC was determined by inductively coupled plasma optical emission spectrometry (ICP-OES).

3.2.4. Differential Scanning Calorimetry

Differential scanning calorimetry was used to determine the temperature of the phase transitions occurring upon heating and cooling of the sample. DSC measures the difference in heat flow rate between a sample and a reference sample while both are subjected to a controlled temperature program. As the sample is altered there is normally a change in property, such as a crystal structure or solid-liquid transition, which results in the DSC measuring a difference in heat flow between the sample and reference. Typically, the transition temperature at which the phenomena occurs is identified. [130]

The Netzsch STA has a heat flux DSC with a disk-type measuring system. Heat flux DSC has a well-defined heat conduction path with a given thermal resistance, and measures the exchange of heat with the environment. The temperature difference between the sample, T_s , and the reference, T_r , is the primary measurement signal in this system, ΔT . [130]

$$\Delta T = T_s - T_r \quad (3.7)$$

This signal is given as a voltage. The heat flow rate, ϕ_m is proportional to the ΔT , and is corrected for by the internal calibration, K' , of the STA: [130]

$$\phi_m = -K' \cdot \Delta T \quad (3.8)$$

In this disk-type configuration, the heat flow occurs through a disk which serves as a solid sample support, which allows for high sensitivity for samples of small volume.

Heat flows from the furnace to the sample, and passes through the disk which is of medium thermal conductivity. Temperature sensors integrated in the disk cover the area of support to the crucibles. If the system is in steady state equilibrium, the heat flow to the sample and reference is the same, and the ΔT is zero. Any change in the equilibrium due to a transition of the sample will generate a differential signal, which is proportional to the difference in heat flow rates to the sample and the reference. [130]

The heat flow rates are measured as a function of temperature or time. Data acquisition systems, in this case the program Proteus Analysis, are used to convert the measured data to a curve. To determine a phase transition temperature, the curve is plotted as differential heat flow rate versus the temperature of the furnace. A peak in the baseline of the curve appears when the steady state equilibrium between the sample and the reference is disturbed by thermally activated heat production, or consumption by the sample, that result from transitions or reactions. The experimental conditions and sample properties, such as heat rate, thermal conductance of the sample, and mass of the sample, strongly affect the shape of the peak. The heat rate and the thermal conductance determine the descending slope of the peak. Figure 3.4 displays typical DSC curves for heating and cooling a sample of UCl_3 -LiCl. The eutectic temperature is found by extrapolating the onset temperature of the eutectic peak. The onset temperature is extrapolated from the auxiliary line that ascends from the peak slope and intersects the baseline. [130] The liquidus temperature is taken as the onset temperature of the baseline shift. [16, 131]. The extrapolated onset peak is independent of the experimental parameters which allows for the use of smaller sample sizes. The onset temperature of the cooling curve is about 20 K of supercooling displayed in figure 3.4. Supercooling results from nucleation and crystal growth, and is an abrupt process that accounts for the very sharp peaks seen in figure 3.4. [132] Upon melting, there is thermal resistance limited heat flow within the sample which causes a thermal lag and results in a shallower slope of the heating curve compared to the cooling curve. Supercooling is affected by particle size and cooling rate. [132] To determine whether supercooling is affected more by particle size or cooling rate, symmetry tests of varying heating and cooling rates can be performed with the DSC. In these multiple heating/cooling rate tests, a sample is thermally cycled at various heating and cooling rates within the same thermo-profile. The onset temperature of the transition is

plotted versus heating and cooling rate, and the zero heating rate extrapolated from the heating and cooling rates. [130, 132, 133] As previously stated, the thermal conductance and heating rate determine the slope of the peak. The temperature difference results in a thermal lag, ΔT_l : [132]

$$\Delta T_l = R_{th} \cdot \phi_s \quad (3.9)$$

$$\phi_s = m_s c_p \frac{dT}{dt} \quad (3.10)$$

In equation 3.9, R_{th} is the thermal resistivity, reciprocal of the thermal conductance, between the particle and the membrane, and ϕ_s is the heat flow to the sample, which is defined in equation 3.10. In equation 3.10, m_s is the mass of the sample, c_p is the specific heat capacity of the sample, and dT/dt is the heating/cooling rate. Based on equation 3.9, thermal lag has a linear relationship with the rate; therefore, the onset temperature of the transition increases linearly with the heating rate. [132] If supercooling in the system of interest was mainly a product of the rate of nucleation, then ideally, the effects of supercooling could be overcome by extrapolating to the zero heating rate transition from the heating and cooling curves. [130, 132]

Temperature modulated DSC (TMDSC) can also be used to analyze kinetic events, such as the effects of the rate of nucleation on supercooling, and heat capacity. In TMDSC, sinusoidal temperature fluctuations during a single thermal cycle to allow for the separation of the heat capacity baseline from the heat flow signal. TMDSC allows for the identification, measurement and quantification of kinetic events by generating multiple signals in a single experiment. These signals allows for the total heat flow signal to be analyzed by individual components. [130, 133]

$$\phi(T, t) = C_p(T) \cdot \frac{dT}{dt} + \phi^{ex} \quad (3.11)$$

In equation 3.11, the differential heat flow rate, $\phi(T, t)$, has two components; the non-zero heat capacity, which is equal to the heat capacity, $C_p(T)$, multiplied by the heat rate, and the kinetic heat flow rate, which is the additional endothermic or exothermic process that occurs at a certain temperature and rate, ϕ^{ex} . TMDSC studies the linearity and stationarity of a system to allow for the measurement of heat capacity and kinetic processes during a single thermal cycle. [130, 133]

3.2.5. XRD Analysis

X-ray diffraction samples were prepared in the argon filled glovebox. The samples were loaded, inside the argon glove box on a single well glass slide coated with two layers of double sided tape. Kapton film was then mounted on the slide to envelop the slide, with

the aid of a folded piece of cardboard, and sample. Once removed from the glove box, the cardboard was removed and the samples were analyzed on the XRD.

3.2.6. Dissolution of Sample for ICP-OES Analysis

After thermal analysis, the hermetically sealed DSC crucibles containing the samples were transferred to a hood, where the crucibles were cut open, and the samples were dissolved in nitric acid. The solution was heated on a hot plate for about a half hour to allow for the total dissolution of the salt. Solutions were analyzed with a Perkin Elmer Optima 8300 ICP-OES to determine the Li/U and K/U elemental ratios and the concentrations of U and Li in each sample.

3.2.7. Principles of ICP-OES

The principles of ICP inductively coupled plasma systems are described in section 3.1.6. OES, which is shorthand for optical emission spectroscopy, is used to identify the concentration of elements present in a sample. After the sample is vaporized and ionized, the atoms and ions are excited, and emit light in the ultraviolet or visible region of the spectrum. The light is emitted at wavelengths characteristic of elements of interest, and the intensity of the light emitted can be used to measure the relative concentration of the element of interest by calibration with a set standards for that element. [134]

3.3. Figures

Fission Product Composition, mg of FP Metal/g-U									
Metal	Sr (SrO)	Zr (ZrMoO ₅)	Ru (RuO ₂)	Rh (Rh ₂ O ₃)	Pd (PdO)	Cs (Cs ₂ MoO ₄)	La (La ₂ O ₃)	Ce (CeO ₂)	Nd (Nd ₂ O ₃)
mg/g-U	0.805	3.79	2.28	0.492	1.433	2.49	1.28	2.48	4.22
Metal	Sm (Sm ₂ O ₃)	Eu (Eu ₂ O ₃)	Gd (Gd ₂ O ₃)	Tb (Tb ₂ O ₃)	Dy (Dy ₂ O ₃)	Er (Er ₂ O ₃)	Lu (Lu ₂ O ₃)	Pr (Pr ₂ O ₃)	total FP metals
mg/g-U	0.9	0.136	0.126	0.003* (.123)	0.001* (0.138)	0.001* (0.151)	0.001* (0.127)	1.17	21.6 (~2.2%)

Table 3.1 Fission product composition based on a calculated composition of 3.2% enriched used fuel with 33 MWd/kg burnup in a typical PWR after 10 years of cooling.[127] Fission product partitioning experiments contained about 2.2 % of this composition in each melt.

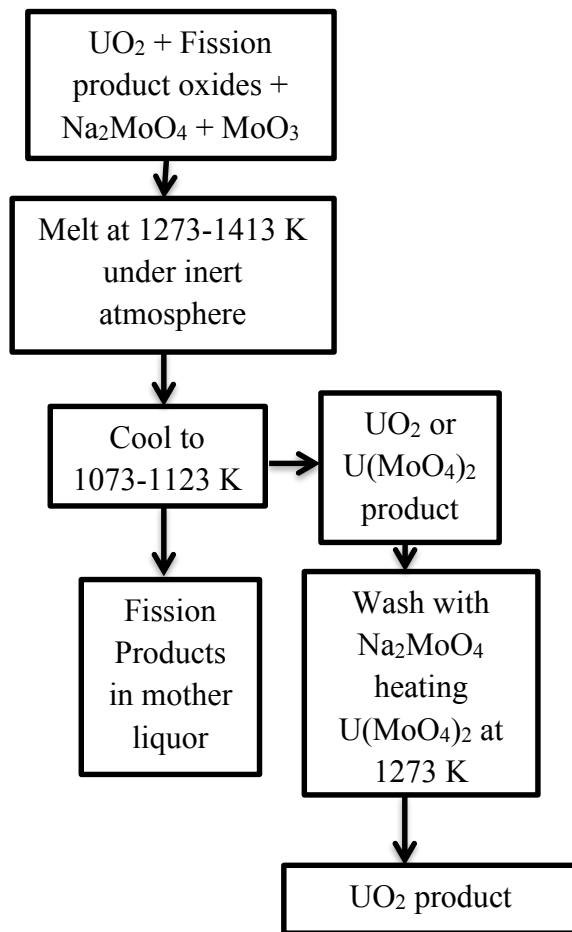


Figure 3.1 Flowchart diagramming UO_2 partitioning in the molybdate melt [11-15, 38, 39]

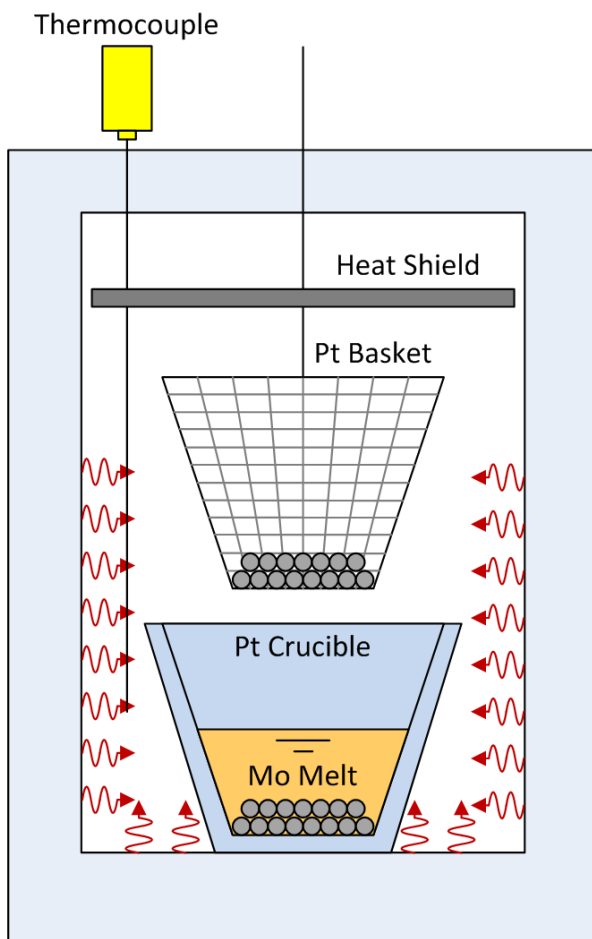


Figure 3.2 Sketch of experimental apparatus inside the tube furnace

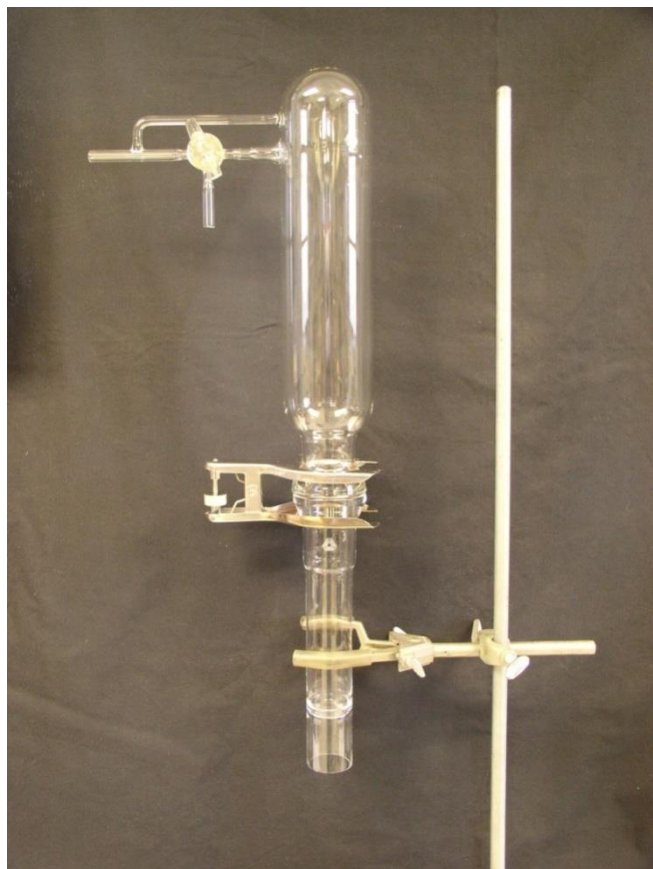


Figure 3.3 Actinide chloride synthesis reactor vessel

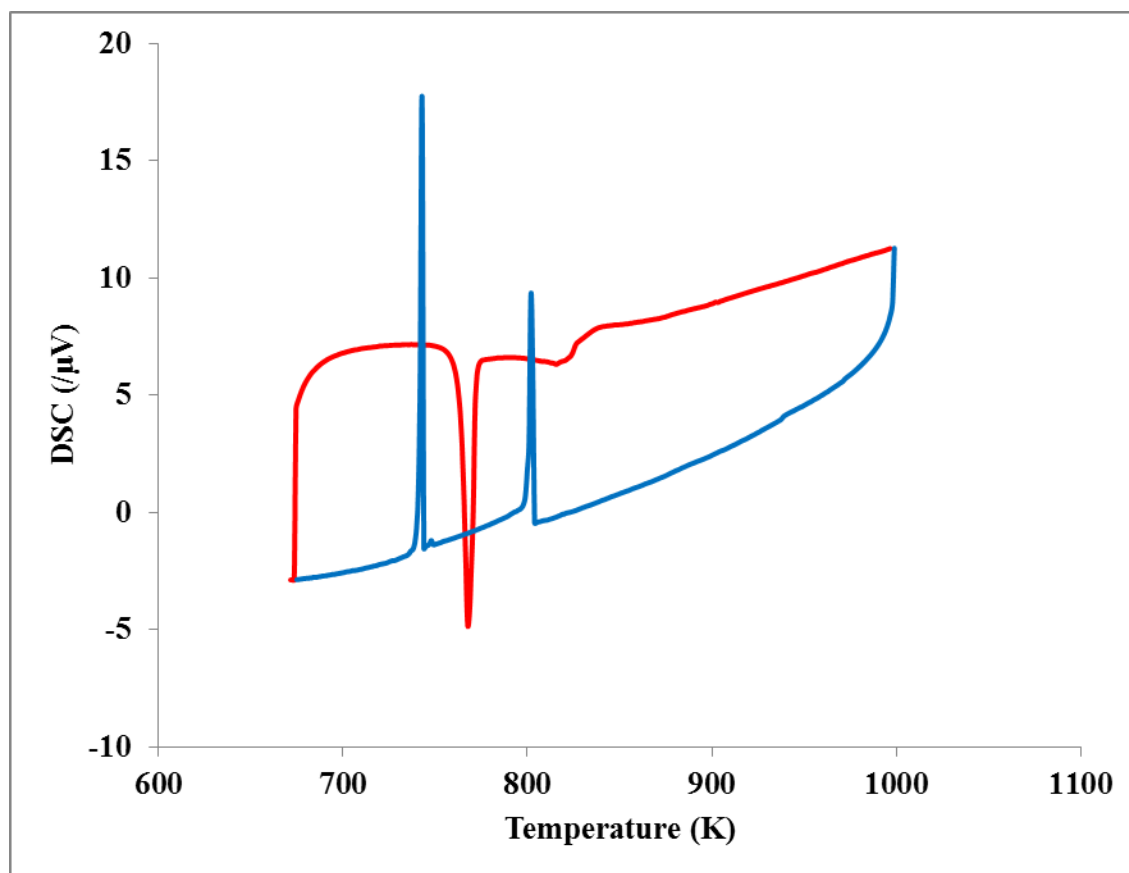


Figure 3.4 DSC curves for a sample of 13.24 ± 0.03 mol% UCl₃-LiCl. The heating curve is shown in red, while the cooling curve is shown in blue.

Chapter 4
Investigation of Molybdate Melts as an Alternative Method of Reprocessing
Used Nuclear Fuel

Amber L. Hames^{1,2}, Peter Tkac², Alena Paulenova¹, James L. Willit², and Mark A. Williamson²

1. Oregon State University 1500 SW Jefferson St. Corvallis, OR 97331

2 Argonne National Laboratory 9700 S Cass Ave. Argonne, IL 60439

4.1. Abstract

An investigation of molybdate melts containing sodium molybdate (Na_2MoO_4) and molybdenum trioxide (MoO_3) to achieve the separation of uranium from fission products by crystallization has been performed. The separation is based on the difference in solubility of the fission product metal oxides compared to the uranium oxide or molybdate in the molybdate melt. The molybdate melt dissolves uranium dioxide at high temperatures, and upon cooling, uranium precipitates as uranium dioxide or molybdate, whereas the fission product metals remain soluble in the melt. Small-scale experiments using gram quantities of uranium dioxide have been performed to investigate the feasibility of UO_2 purification from the fission products. The composition of the uranium precipitate as well as data for partitioning of several fission product surrogates between the uranium precipitate and molybdate melt for various melt compositions are presented and discussed. The fission products Cs, Sr, Ru and Rh all displayed very large distribution ratios. The fission products Zr, Pd, and the lanthanides also displayed good distribution ratios ($D > 10$). A melt consisting of 20 wt% MoO_3 - 50 wt% Na_2MoO_4 -30 wt% UO_2 heated to 1313 K and cooled to 1123 K for the physical separation of the UO_2 product from the melt, and washed once with Na_2MoO_4 displays optimum conditions for separation of the UO_2 from the fission products.

4.2. Introduction

Pyrochemical processes are very attractive for recycling short-cooled used nuclear fuel due to the use of inorganic salts since they are more resilient against radiolytic processes than the aqueous or organic solvents, which are used in solvent extraction processes. [1-3] In addition, the use of inorganic salts has the potential to significantly reduce the volume of waste produced during the processing compared to solvent extraction processes. [1-3] Generally, halide-based molten salts have been used as electrolytes in electrorefining used nuclear fuel; [1-3] however, Ustinov *et al.* have explored molybdate melts for an alternative pyrochemical processing technique, specifically for oxide fuel treatment. [4-9] We explored this alternative approach in developing a so-called modified open fuel cycle in which the actinides are recovered for recycle. In this approach, near crystallization methods are used to achieve the desired separations in which the used nuclear fuel is dissolved in the molybdate melt containing a mixture of sodium

molybdate (Na_2MoO_4) and molybdenum trioxide (MoO_3) at temperatures between 1273-1413 K, and UO_2 (or transuranic oxides) recrystallize upon cooling, separating it from the fission products. [4-12] The process is based on the difference in solubility of the fission product metal oxides compared to the uranium (or transuranic) oxides in the molybdate melt. [4-12] The advantage of this process is that the fission products are more soluble in molybdate melt than the UO_2 . The fission product metals are oxidized in MoO_3 and form molybdates, or other oxides, and the resulting products are soluble in Na_2MoO_4 . [5] As the temperature of the system increases, the solubility of UO_2 in MoO_3 increases. At temperatures exceeding 1273 K, any UO_2 that dissolves in MoO_3 forms $\text{U}(\text{MoO}_4)_2$. [7] In addition, most of the fission product oxides are also very soluble in Na_2MoO_4 , while UO_2 has very limited solubility, a property of the system that can be used for its separation from fission products. [4-11] Upon cooling to 973-1073 K, the fission products remain soluble in the melt, the mother liquor, whereas uranium precipitates as uranium dioxide or uranium molybdate, depending on the initial composition of the salt. [10-12] A wash of Na_2MoO_4 is then used to remove any remaining fission product oxides or molybdates from the uranium-bearing precipitate. [4-12]

Ustinov reported that recrystallization of $\text{U}(\text{MoO}_4)_2$ from a UO_2 - MoO_3 melt containing fission products yielded a 98-99% purification from Cs, Ce, Pr, Zr, and Nb; however only a 60% purification from Ru and Rh was achieved [1]. For the recrystallization of UO_2 from a UO_2 - MoO_3 - Na_2MoO_4 melt, the purification from Cs, La, Zr and Nb was 98.5-99.9% efficient. [4] There is no change in the oxidation state of uranium (or transuranics); therefore, no electrochemical methods or additional oxidants or reductants are required, and the actinide oxide product can be filtered from the fission products that remain in the melt. [10-12]

Small scale experiments using gram quantities of uranium have been performed to test the feasibility of using the molybdate melts to purify UO_2 from fission products. In addition to looking at the feasibility of the molybdate melts, the method of contamination of the UO_2 product by the fission products, and the optimum conditions for dissolution and precipitation of uranium oxide or molybdate and its separation from selected simulated fission product oxides were investigated. Our study explored UO_2 recovery as

a function of the composition of the molybdate melt, temperature, and precipitate washing with sodium molybdate.

4.3. Experimental

4.3.1. Materials

Nickel based alloys were suggested to be suitable containers for studies conducted in these salt compositions [4, 5, 9], but, severe corrosion was observed when Inconel (Sigma Aldrich) was used as a crucible and basket material in the presence of MoO_3 . A glassy carbon crucible was also experimented with in preliminary tests; however, the crucible corroded after prolonged use in molybdate melts. Platinum was selected for the crucible and basket construction based on its good corrosion resistance to molybdate melts. The platinum crucible, and mesh for the basket were both in-house materials. The crucible was 1.5” in diameter by 1.5” in height. In-house depleted uranium oxide pellets, UO_2 , were used as the source of uranium for the tests. Before processing, the pellets were crushed into smaller pieces to achieve faster dissolution. Fission product oxide simulants and Na_2MoO_4 were purchased from Sigma Aldrich. The MoO_3 was purchased from MP Biomedicals. The oxides and molybdates were homogenized by grinding with a mortar and pestle. The fission product oxide composition used in the study is given in table 4.1. This composition is based on a calculated composition of fission products in the used fuel, with an initial enrichment of 3.2%, after 33 MWd/kg burnup at a mean flux of $3.24 \times 10^{18} \text{ n m}^{-2} \text{ s}^{-1}$ in a typical pressurized water reactor after 10 years of cooling.[13] Select fission product oxides (Tb, Dy, and Er) are in a much higher concentration in the composition than what was calculated due to the difficulty in measuring such small quantities of the oxides in a glovebox.

4.3.2. Experimental Setup of the Melt

Small-scale experiments containing six to seven grams of UO_2 and approximately fifteen grams of MoO_3 and Na_2MoO_4 in varying $\text{MoO}_3:\text{Na}_2\text{MoO}_4$ ratios were performed in a vertical tube furnace inside an argon atmosphere glovebox with oxygen levels less than 10 ppm, and the moisture level between 3 and 50 ppm. Figure 4.1 displays a flowchart of the basic separations process. A diagram of the tube furnace and experimental setup is shown in figure 4.2. The

crucible was situated in the furnace and surrounded by Inconel heat shields. For uranium phase formation experiments, UO_2 , Na_2MoO_4 , and MoO_3 were loaded into the crucible without the basket, heated in the furnace at rate of about 573 K hr^{-1} until the temperature reached 1473 K , and held for about 8 hours to allow for the dissolution of UO_2 in the melt. The temperature was monitored by a type K thermocouple. For fission product partitioning experiments, UO_2 , Na_2MoO_4 , MoO_3 , and the fission product mixture were loaded into the basket and placed in the crucible. The mixture was heated at the same rate and to the same temperatures for the same amount of time, as the phase formation experiments. Because the melt was in a closed furnace, the possible release of gaseous fission products upon the dissolution of the simulated UO_2 fuel into the melt could not be monitored. The melt was then cooled to a pre-determined temperature in the range of $973\text{-}1073 \text{ K}$, at which point the uranium precipitated as an oxide or molybdate. The platinum basket was lifted out of the crucible to allow for the physical separation of the uranium product from the fission products, which remained in the salt phase. The temperature was held at $973\text{-}1073 \text{ K}$ for about 10 hours to give ample separation time. When the system was cooled to room temperature, the precipitate was recovered. After the precipitate was recovered from the basket, the product was washed with approximately thirty grams of liquid Na_2MoO_4 .

4.3.3. Composition of Uranium Product

Experiments varying the composition of the initial melt of MoO_3 , Na_2MoO_4 , and UO_2 allowed for the determination of the composition of the main uranium-bearing precipitate upon cooling. Compositions of the melts studied are given in table 4.2. To determine the composition of the uranium product from different compositions of the molybdate melts, samples of the uranium precipitate were analyzed using X-ray diffraction analysis (XRD). After cooling, samples of the uranium precipitate were transferred to a hood. The samples were ground and washed several times with de-ionized (DI) water to remove excess molybdate melt, and then air dried. A thin layer of powder was placed on a glass plate covered with double sided tape to allow the precipitate to adhere to the slide. The precipitate was then covered with a thin Mylar film.

To identify the uranium-bearing phases obtained, the experimental XRD spectra were compared to the PDF database. [14]

4.3.4. Dissolution of Uranium Product for ICP-MS Analysis

After cooling, a portion of the uranium-bearing precipitate was removed from the basket and transferred for dissolution. Samples were first washed with NaOH to remove any residual molybdenum salts, and then washed with 0.1M HNO₃, which removes any remaining fission products that could be present on the surface of the precipitate. Due to the high solubility of sodium molybdate, 65 g/100 g H₂O, [16], deionized water with a resistivity $\geq 18 \text{ M}\Omega \text{ cm}$ was used to remove a significant portion of the molybdate salt present in the precipitate after the sodium molybdate wash. After several washes and decanting of the UO₂ precipitate with water, the resulting precipitate was green/brown. The precipitate was initially suspended in the water wash, forming a green/brown solution. The precipitate eventually settled, leaving a yellow solution indicating the presence sodium molybdate in the wash, and the water wash was decanted away. This wash was performed several times. If sodium hydroxide was used instead of water, a clear solution formed. Sodium hydroxide was very effective for removal of molybdenum salts (>99.9% of all Mo present in the precipitate). Both water and sodium hydroxide washes were also effective for the removal of any remaining cesium. When Cs₂O was dissolved in MoO₃ at temperatures exceeding 673 K, Cs₂MoO₄ formed, which is very soluble in water. For precipitates containing uranium molybdates, a combination of NaOH and H₂O₂ was the most effective way for dissolution of the uranium molybdates (UMo₂O₈, UMo₇O₂₂, and UMo₁₁O₃₅). On the other hand, precipitates obtained from mixtures with higher Na₂MoO₄ content were mostly UO₂ and they dissolved in HNO₃/H₂O₂ solutions. The product of mostly UO₂ and possibly Na₄U(MoO₄)₄, was then dissolved in HNO₃ with the addition of H₂O₂ to accelerate dissolution of the UO₂.

Elemental analysis of uranium containing precipitates was performed using ICP-MS

4.4. Results
(PerkinElmer SCIEX ELAN DRC II) with a reported uncertainty of +/-10%.

4.4.1. Uranium Speciation

Figure 4.3 shows photographs of the precipitated products after they were recovered from the Pt mesh basket. Information regarding the composition of each melt, the color of the samples

after rinsing with water, the major and minor uranium species identified, as well as the solubility of the product is provided in table 4.2.

4.4.2. Fission Product Partitioning

After dissolving the uranium product using the procedure discussed in Section 5.3.4, samples were analyzed using ICP-MS to determine the distribution ratio of the fission products remaining in the sample. To determine the effectiveness of the separation, the distribution ratio was calculated from ratio of the mass of fission product in the melt and the mass of fission product remaining in the uranium product:

$$D = \frac{\text{Fission Product}_{\text{melt}}}{\text{Fission Product}_{\text{U Product}}}$$

Distribution ratios for the fission products studied are provided in Figures 4.5-7.

4.5. Discussion

4.5.1. Uranium Composition

The composition of MoO₃ and Na₂MoO₄ in the initial melts directly affected the uranium phase formed during precipitation. It was observed that melts consisting of a MoO₃ mass fraction smaller than UO₂ resulted in a UO₂ precipitate as the major product. These results are consistent with the phase diagram produced by Ustinov *et al.*[5]. The phase diagram reveals that compositions consisting of much higher mass fractions of MoO₃ result in U(MoO₄)₂. Results reported here confirm that MoO₃-rich salt compositions (MoO₃>UO₂) usually lead to the formation of the purple uranium molybdate precipitate (U(MoO₄)₂).

Samples resulting in UO₂ displayed good separation between UO₂ and the excess molybdate salt. As seen in figure 4.3, the product of sample 1 formed from the composition 20% MoO₃- 50% Na₂MoO₄- 30% UO₂ showed two separate layers. The bottom dark layer is the UO₂, which settled to the bottom of the crucible upon cooling, while the top yellow layer is the less dense excess MoO₃ and Na₂MoO₄. After this sample was washed with water to remove the molybdate salt layer, it was analyzed by XRD. The XRD spectrum of this sample, figure 4.4, confirmed the effective separation, as no molybdate salt remained in the sample. Based on XRD analysis, the product was identified as UO₂.

To determine the effect of Na_2MoO_4 washes on the product's composition, two samples of the same composition (60% MoO_3 -30% UO_2 - 10% Na_2MoO_4) were analyzed, one with a Na_2MoO_4 wash (sample 6) and one without the wash (sample 5). Sample 5 resulted in a $\text{U}(\text{MoO}_4)_2$ product, which was to be expected with such a high concentration of MoO_3 . Sample 6 resulted in a UO_2 product. According to Ustinov, the Na_2MoO_4 wash forms two incongruently melting compounds with the $\text{U}(\text{MoO}_4)_2$ left in the melt, and, upon cooling, these compounds decompose to a UO_2 product in the temperature range between 973 and 1073 K. [13] Our products from samples 5 and 6 confirmed Ustinov's findings. The ability of the Na_2MoO_4 wash to form the UO_2 product from the $\text{U}(\text{MoO}_4)_2$ product demonstrated the necessity of the Na_2MoO_4 wash. Ustinov *et al.* explained that the limited solubility of the UO_2 in the Na_2MoO_4 is important because the MoO_3 serves as the solvent, while the Na_2MoO_4 serves to precipitate the UO_2 . This explains the reason that melts consisting of UO_2 - MoO_3 recrystallize $\text{U}(\text{MoO}_4)_2$, while melts consisting of UO_2 - Na_2MoO_4 - MoO_3 recrystallize UO_2 . [4]

4.5.2. Fission Product Partitioning

Figures 4.5-7 display the distribution ratios of the fission products in melts as a function of sample composition, temperature of the melt, and number of Na_2MoO_4 washes. In all of the melts, Cs, Sr, Ru, and Rh displayed very large distribution ratios ($D > 100$), indicating good purification of the uranium product. Other fission products, including Zr, Pd and the lanthanides (Ln) displayed smaller distribution ratios, ($D > 10$), however, this purification is an adequate separation from the uranium product. In order to determine optimum conditions for the removal of the fission products with small distribution ratios ($D > 10$) and to increase purification of the uranium product, the methods by which the fission products contaminate the uranium product was examined.

According to Tul'skii *et al.*, the fission products have four methods by which they could contaminate the UO_2 product [7]:

1. The fission product oxide could be dissolved in the mother liquor and entered the UO_2 product via adsorption or trapping of the mother liquor onto the surface of the product.
2. The fission product oxide can interact with the uranium mixed molybdate $3\text{Na}_2\text{MoO}_4 \cdot 2\text{U}(\text{MoO}_4)_2$, replacing the Na ion in the mixed molybdate.

3. The fission product oxide or molybdate could crystallize parallel to the UO_2 , but not be washed out during elutriation because the specific gravity of the fission product oxide is too close to the specific gravity of the UO_2 product.
4. The fission product oxide could form a solid solution with the UO_2 , which would incorporate the fission product into the UO_2 lattice during crystallization.

The first two methods of contamination could be reduced by washing the product with multiple Na_2MoO_4 washes. The Na_2MoO_4 wash would dissolve the fission product oxide on the surface of the product, removing the contaminant from the product. The Na_2MoO_4 wash would also react with the mixed molybdate contaminated with fission products, and decompose the uranium-bearing phase to the UO_2 product. The third method of contamination is expected to be compensated for by physically lifting the Pt mesh basket with the UO_2 product out of the mother liquor, thus separating the UO_2 product from the mother liquor upon cooling. For example, in the case of Ru, Tul'skii was able to conclude that the Ru crystallizes parallel with UO_2 but can be separated if there are separate zones for crystallization.[7] These separate zones are achieved during the physical separation of the UO_2 contained in the Pt basket upon cooling to temperatures low enough for the UO_2 to precipitate, but higher than the crystallization temperatures of the fission product oxides. At these temperatures, while the UO_2 is precipitating in the Pt basket, the liquid fission product oxides remain in the Pt crucible. The final method of contamination is considered the most common method of contamination for the fission product oxides, as most of the fission product oxides, especially the lanthanides, are known to form solid solutions with UO_2 . [16,17]

4.5.2.1. Effect of Melt Composition

Figure 4.5 shows data from samples with varying $\text{MoO}_3:\text{Na}_2\text{MoO}_4$ ratios at a constant concentration of UO_2 . The compositions containing 20, 30, and 50% MoO_3 were of interest because uranium phase composition experiments indicated that these $\text{MoO}_3:\text{Na}_2\text{MoO}_4$ ratios produce the desired UO_2 product. To investigate the effect of the melt composition on fission product partitioning, partitioning experiments heated to 1413 K were conducted because initial uranium phase composition experiments were

performed at this temperature. When the same experiment was performed at 1313 K, similar trends were seen for the partitioning of fission products from the UO_2 product. The composition that displayed the best partitioning at 1413 K for the lanthanides and Zr is the 20% MoO_3 -50% Na_2MoO_4 -30% UO_2 composition. From the uranium product composition experiments, this composition resulted in UO_2 as the final product. The UO_2 can be contaminated by the lanthanides and zirconium oxides during the crystallization process because of the formation of fission product oxide-uranium oxide solid solutions [16-18]. For example, as zirconium dissolves in the molybdate melt, the compound ZrMo_2O_8 forms, which incongruently melts and decomposes to ZrO_2 [4]. Fission product contamination was lessened in the 20% MoO_3 -50% Na_2MoO_4 -30% UO_2 melt because the high concentration of Na_2MoO_4 allowed for the increased solubility of the lanthanides and zirconium in the melt, forming molybdates, and the low concentration of MoO_3 decreased the solubility of UO_2 in the melt, decreasing the fission product oxide's opportunity to form solid solution with the UO_2 .

When the Na_2MoO_4 concentration was decreased below 50% and the MoO_3 concentration was increased to the same level as UO_2 (30% MoO_3 -40% Na_2MoO_4 -30% UO_2), the distribution ratios for the lanthanides and zirconium decreased. This result suggests that the solubility of the zirconium and lanthanide fission product oxides is directly proportional to the amount of the Na_2MoO_4 in the melt, which is consistent with the finding above. However, this trend was not seen in the composition 50% MoO_3 -20% Na_2MoO_4 -30% UO_2 , at 1413 K, where the distribution ratios for zirconium and the lanthanides are greater than the 30% MoO_3 -40% Na_2MoO_4 -30% UO_2 composition. From the uranium product composition experiments, it was seen that the samples containing 30% MoO_3 -40% Na_2MoO_4 -30% UO_2 formed a UO_2 product, while the 50% MoO_3 -20% Na_2MoO_4 -30% UO_2 composition formed UO_2 and $\text{U}(\text{MoO}_4)_2$ products. The increased solubility of the UO_2 in the melt due to larger MoO_3 : Na_2MoO_4 ratios allowed for more $\text{U}(\text{MoO}_4)_2$ formation. The high distribution ratios of Sr and Cs appeared as fission products (in log scale) of the weight fractions of MoO_3 and Na_2MoO_4 . As SrO-UO_2 is known to form solid solutions [62, 63], the trace amount of Sr left in the product could be attributed to a solid solution of SrO_2 formed with UO_2 , however, this trace amount of Sr is more likely present due to the interaction SrMoO_4

with the mixed molybdate, $3\text{Na}_2\text{MoO}_4 \cdot 2\text{U}(\text{MoO}_4)_2$. The removal of this type of contamination is discussed in a later section.

4.5.2.2 Temperature Effects

Figure 4.6 displays the fission product partitioning that result from varying the temperature to which the melt was heated. The distribution ratio for the heavier lanthanides, and Zr, appeared to be nearly constant at the two temperatures studied for the concentration of 30% MoO_3 , while the lighter lanthanides, displayed better partitioning at the lower temperatures, especially for the 50% MoO_3 composition. As previously discussed, the lanthanides form solid solutions with UO_2 . [16-19] Increasing the temperature of the system increased the solubility of the UO_2 in the MoO_3 . This increased solubility of the UO_2 potentially allows for increased formation of the fission product oxide- UO_2 solid solutions. This observation explains the greater purification of the lanthanides at the lower temperatures.

Another fission product that exhibited temperature dependence was Ru, which had better partitioning at the higher temperatures. Unlike the rest of the fission product oxides, RuO_2 is not soluble in MoO_3 . [4] RuO_2 is also very volatile at temperatures exceeding 1173 K, therefore, the higher temperature could lead to volatilization of Ru from the melt; however, our experiments were not designed to detect fission product vaporization.

4.5.2.3. Effects of the Na_2MoO_4 Washes

As seen in the uranium product composition experiments, the Na_2MoO_4 wash breaks down the $\text{U}(\text{MoO}_4)_2$ product to form a UO_2 product. This approach is not the only application of the Na_2MoO_4 wash. One method for the fission product oxides to contaminate the uranium product is by dissolving in the mother liquor and adsorption or trapping of the mother liquor onto the surface of the UO_2 product. Due to the slight solubility of the UO_2 in Na_2MoO_4 and the large solubility of the fission product oxides in the Na_2MoO_4 , washes using Na_2MoO_4 can remove this form of contamination by forming the fission product molybdates.

Fission product oxides can also interact with the mixed molybdate $3\text{Na}_2\text{MoO}_4 \cdot 2\text{U}(\text{MoO}_4)_2$ by replacing the sodium ion [7]. Fission product molybdates and

uranium molybdate are very soluble in Na_2MoO_4 , therefore, multiple washes using Na_2MoO_4 decompose the mixed molybdate, removing the fission product contamination and purifying the UO_2 product.

Figure 4.7 shows the distribution ratios of all the fission products after one or three Na_2MoO_4 washes performed for a composition of 30 % MoO_3 -40% Na_2MoO_4 - 30% UO_2 . The distribution ratio for Cs, Sr, Rh and Pd clearly indicated that surface or substitutional contamination occurred because the purification of the fission products increased by increasing the number of Na_2MoO_4 washes. When Tul'skii *et al.* performed experiments to remove trace amounts of Cs from UO_2 , they speculated that the Cs was incorporated into the mixed molybdate lattice of $3\text{Na}_2\text{MoO}_4 \cdot 2 \text{U}(\text{MoO}_4)_2$ by replacing the Na ion .[7] The high distribution ratio achieved for the Cs after multiple washes of Na_2MoO_4 suggest that nearly all of the Cs was removed from the UO_2 product. The results of the Na_2MoO_4 washes indicate that the Cs is likely incorporated in the of $3\text{Na}_2\text{MoO}_4 \cdot 2 \text{U}(\text{MoO}_4)_2$ lattice (or surface contamination). Sr and Rh also exhibited reasonable purification from the final product with multiple washes of Na_2MoO_4 . SrO is known to form Sr_2MoO_4 with MoO_3 , and Rh_2O_3 is very soluble in the Na_2MoO_4 and MoO_3 , which would result in their increased removal from the product with multiple washings. Little information is known of how Pd interacts with the MoO_3 and Na_2MoO_4 . Due to the increased purification that Pd displays with multiple washes of Na_2MoO_4 , it is speculated that Pd contaminates UO_2 either by dissolution in the mother liquor followed by adsorption or trapping of the mother liquor on the surface of the UO_2 . Additional Na_2MoO_4 washes suggest that the molybdate did not contaminate the UO_2 product by forming a mixed molybdate, and that the oxides does not dissolve in the mother liquor, and crystallize on the UO_2 through trapping or adsorption. Tul'skii *et al.*, claimed that Ce entered the UO_2 lattice by forming a solid solution of $\text{UO}_2\text{-Ce}_2(\text{MoO}_4)_3$ during crystallization. Tul'kii also claimed that the $\text{Ce}_2(\text{MoO}_4)_3$ dissolves in the mother liquor, and penetrates the UO_2 by adsorption. [7] Figure 4.7 does not support this second claim, as the distribution ratio for Ce did not increase as the number of Na_2MoO_4 washes increase.

4.6. Conclusion

Molybdate melts demonstrated the ability to separate fission products from a uranium product for potential application of a modified open fuel cycle for used fuel treatment. Overall, the conditions we identified to achieve the purest uranium oxide product were:

1. A melt consisting of 20 wt% MoO₃- 50 wt% Na₂MoO₄-30 wt% UO₂
2. Heating the melt to 1313 K and performing the physical separation of the UO₂ from the mother liquor.
3. Washing the uranium product once with Na₂MoO₄.

It was determined that melt compositions containing more MoO₃ than UO₂ yield uranium molybdates as a major species, such as UMo₂O₈, while melts containing less MoO₃ lead to the formation of UO₂ precipitate as a major species.

The fission products investigated in the mock fuel displayed adequate partitioning from the uranium precipitate product. Certain fission products such as Cs, Sr, Ru and Rh displayed particularly good separations ($D=100-55000$), while Zr, and the lanthanides, had lower distribution ratios ($D=5-100$). Distribution ratios greater than 10 are adequate for purification of the UO₂. Zirconium and the lanthanides displayed the best partitioning in melts consisting of 20% MoO₃-50% Na₂MoO₄-30% UO₂.

The fission product oxides exhibited better partitioning when the system was only heated to 1313 K as compared to 1413 K. The UO₂ and fission products were more soluble in the MoO₃ at 1413 K, which increased the opportunity to form solid solutions with the fission product oxides as the solution was cooled to precipitate the UO₂.

A number of washes of Na₂MoO₄ allowed for greater removal of Cs, Sr, Rh and Pd contaminants from the UO₂ by dissolving them into the wash solution. These contaminants were likely present in the UO₂ from adsorption or trapping of the mother liquor onto the surface of the product, or interacting with the mixed molybdate 3Na₂MoO₄·2U(MoO₄)₂ by replacing the Na ion. However, no obvious benefit in repeated washing steps was observed for Zr and lanthanides, and thus was not deemed necessary for purification of the UO₂ product.

This study demonstrated the feasibility of using the molybdate process for the recovery of UO₂ and provided insight into fission product partitioning during the process. However,

a significant amount of work remains to be completed before the process can be used in the treatment of used nuclear fuel.

4.7. Acknowledgements

The submitted manuscript has been created by U Chicago Argonne, LLC, Operator of Argonne National Laboratory (“Argonne”). Argonne, a U.S. Department of Energy Office of Science laboratory, is operated under Contract No. DE-AC02-06CH11357. The U.S. Government retains for itself, and others acting on its behalf, a paid-up nonexclusive, irrevocable worldwide license in said article to reproduce, prepare derivative works, distribute copies to the public, and perform publicly and display publicly, by or on behalf of the Government. Argonne National Laboratory’s work was supported by the U.S. Department of Energy, Office of Nuclear Energy, under contract DE-AC02-06CH11357.

4.8. References

1. Laidler, J.J., et al., *Development of pyroprocessing technology*. Progress in Nuclear Energy, 1997. **31**(1): p. 131-140.
2. Williamson, M.A. and J.L. Willit, *Pyroprocessing Flowsheets for Recycling Used Nuclear Fuel*. Nuclear Engineering and Technology, 2011: p. Medium: X; Size: 329-334.
3. McPheeters, C.C., R.D. Pierce, and T.P. Mulcahey, *Application of the pyrochemical process to recycle of actinides from LWR spent fuel*. Progress in Nuclear Energy, 1997. **31**(1): p. 175-186.
4. Ustinov, O.A., *The physical chemistry for regenerating spent uranium and plutonium oxide fuel by recrystallization from molybdate melts*. Atomic Energy, 1997. **82**(2): p. 99-102.
5. Ustinov, O.A., L.P. Sukhanov, and S.A. Yakunin, *Reprocessing of spent oxide nuclear fuel by recrystallization in molybdate melts*. Atomic Energy, 2006. **101**(4): p. 771-774.
6. Prokoshin A.D., U.O.A., Andrianov I.A., Chebotarev N.T., Matyushin E.A., , *The MoO₃-PuO₂ System*. Russian Journal of Inorganic Chemistry, 1976. **21**(6): p. 854-856.
7. Tul'skii G.V., U.O.A., *Behavior of Trace Impurities of Ruthenium, Cerium, and Cesium in the Crystallization of Uranium Dioxide from Molten UO₂-MoO₃-Na₂MoO₄*. Radiochemistry, 1977. **19**(3): p. 254-259.
8. Ustinov, O.A., et al., *The system MoO₃-UO₃*. Soviet Atomic Energy. **34**(3): p. 203-205.
9. Ustinov, O.A., L.P. Sukhanov, and O.N. Pogorelko, *Reduction recrystallization of uranium oxides in molybdate melts*. Atomic Energy. **102**(5): p. 361-363.
10. Hames A.L., Tkac P., Williamson M.A., Willit J.L. *Investigation of Molybdate Melts for Alternative Pyrochemical Reprocessing of Used Nuclear Fuel*. in *2012 International Pyroprocessing Research Conference*. 2012. Fontana, Wisconsin.
11. Tkac P., Hames A.L., Cruse T.A., Willit J.L. Williamson M.A. . *Alternative Pyrochemical Reprocessing of Used Nuclear Fuel Using Molybdate Melts*. in *12th Information Exchange Meeting on Actinide and Fission Product Partitioning and Transmutation 2012*. Prague, Czech Republic.

12. Hames A.L., Tkac P., Paulenova A., Williamson M.A., Willit J.L. *Investigation of U Behavior in Molybdate Melts for Alternative Pyrochemical Reprocessing of Spent Nuclear Fuel*. in *American Chemical Society National Meeting*. 2013. Indianapolis, Indiana.
13. Choppin, G.R., J.-O. Liljenzin, and J.A.N. Rydberg, *CHAPTER 21 - The Nuclear Fuel Cycle*, in *Radiochemistry and Nuclear Chemistry (Third Edition)*. 2002, Butterworth-Heinemann: Woburn. p. 583-641.
14. Liu, L.G., *Eart Planet Sci. Lett*, 1982. **1**: p. 110.
15. *Physical Constants of Inorganic Compounds*, in *CRC Handbook of Chemistry and Physics* CRC Press. p. 87.
16. Desal K.H., G.R.W., Parfitt D., Wiss T., Van Uffelen p., *Atomic-scale Simulation of Soluble Fission Products in UO₂*, in *EUR Report ISSN*, E.C.-J.R.C.-I.f.T. Elements, Editor. 2009, E Institute fo Transuranium Elements.
17. Lang, S.M., et al., *High-temperature reactions of uranium dioxide with various metal oxides*. 1956, National Bureau of Standards, Washington, DC.
18. Cohen, I. and B.E. Schaner, *A metallographic and X-ray study of the UO₂-ZrO₂ system*. *Journal of Nuclear Materials*, 1963. **9**(1): p. 18-52.
19. Evans, P., *The system UO₂-ZrO₂*. *Journal of the American Ceramic Society*, 1960. **43**(9): p. 443-446.

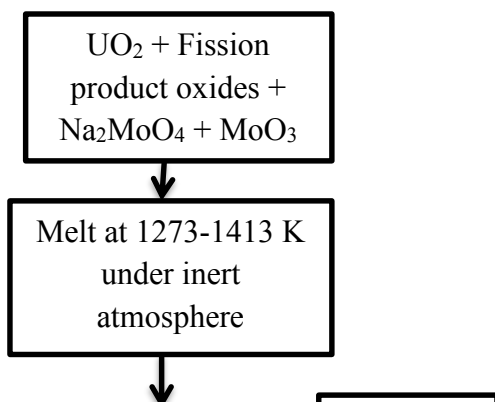
4.9. Figures

Fission Product Composition, mg of FP Metal/g-U									
Metal	Sr (SrO)	Zr (ZrMoO ₅)	Ru (RuO ₂)	Rh (Rh ₂ O ₃)	Pd (PdO)	Cs (Cs ₂ MoO ₄)	La (La ₂ O ₃)	Ce (CeO ₂)	Nd (Nd ₂ O ₃)
mg/g-U	0.805	3.79	2.28	0.492	1.433	2.49	1.28	2.48	4.22

Metal	Sm (Sm ₂ O ₃)	Eu (Eu ₂ O ₃)	Gd (Gd ₂ O ₃)	Tb (Tb ₂ O ₃)	Dy (Dy ₂ O ₃)	Er (Er ₂ O ₃)	Lu (Lu ₂ O ₃)	Pr (Pr ₂ O ₃)	total FP metals
mg/g-U	0.9	0.136	0.126	0.003*	0.001* (0.138)	0.001* (0.151)	0.001* (0.127)	1.17	21.6 (~2.2%)

*larger quantities than expected for this mock fuel composition were actually used; the actual quantities are given in parenthesis below the calculated quantity.

Table 4.1 Fission product composition based on a calculated composition of 3.2% enriched used fuel with 33 MWd/kg burnup at a mean flux of $3.24 \times 10^{18} \text{ n m}^{-2} \text{ s}^{-1}$ in a typical PWR after 10 years of cooling.[13] Fission product partitioning experiments contained about 2.2 % of this composition in each melt.



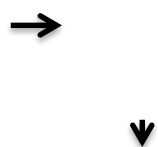


Figure 4.1 Flowchart diagramming UO_2 partitioning in the molybdate melt.

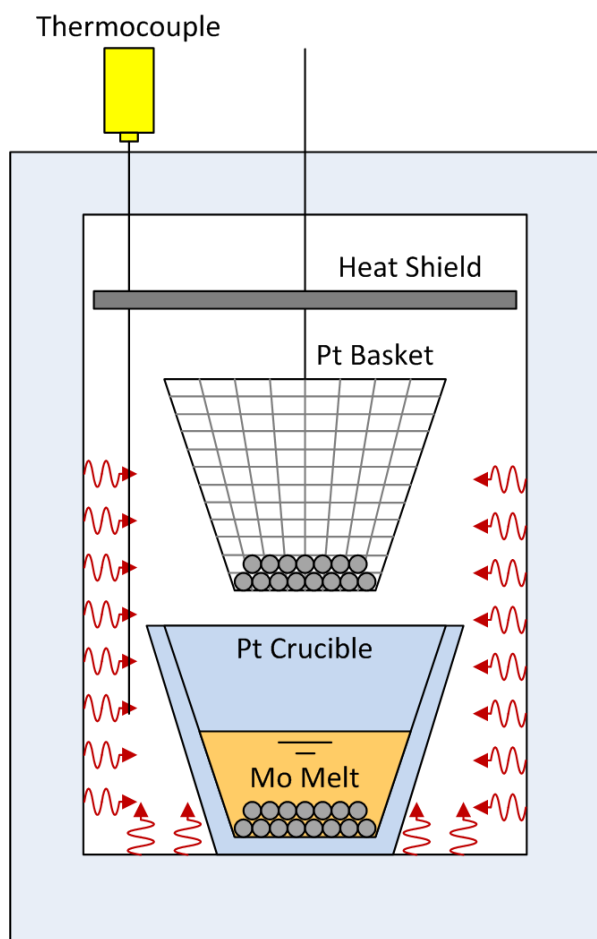


Figure 4.2 Experimental setup inside the tube furnace

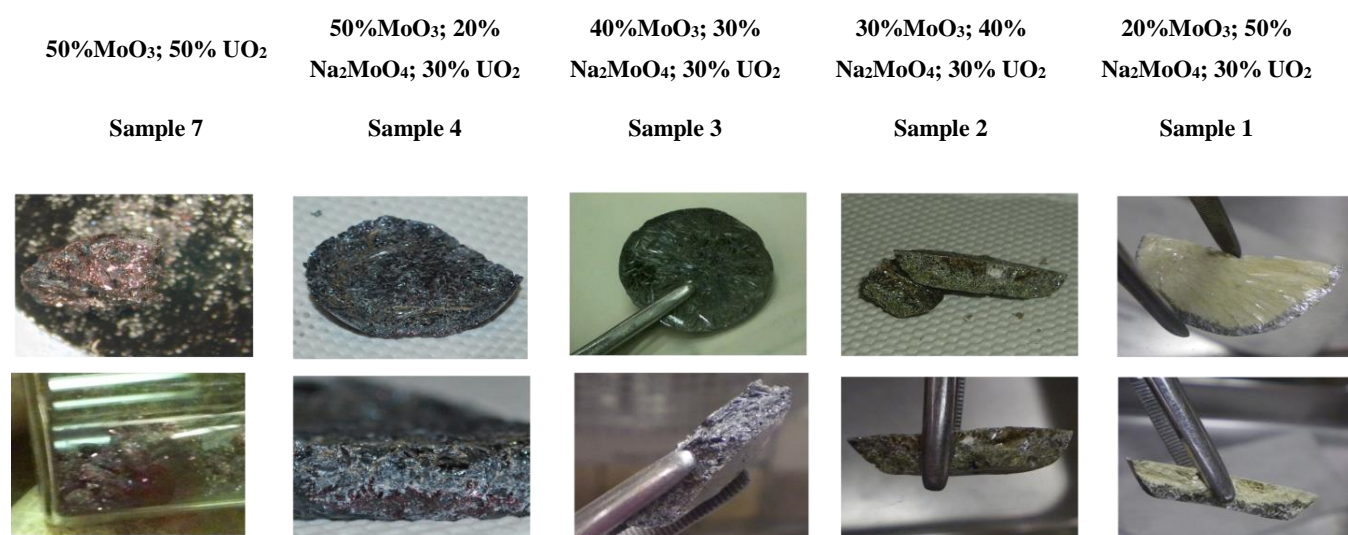


Figure 4.3 Photographs of uranium precipitates obtained from the melts of varying MoO₃, Na₂MoO₄, and UO₂ compositions.

Sample #	Initial Composition (weight %)			Color after H ₂ O wash	Species		Soluble in
	MoO ₃	Na ₂ MoO ₄	UO ₂		Major	Minor	
1	20%	50%	30%	gray-black	UO ₂		Hot HNO ₃ /H ₂ O ₂
2	30%	40%	30%	gray, yellow-green	UO ₂	Na ₄ U(MoO ₄) ₄	Hot NaOH/H ₂ O ₂ partially hot HNO ₃ /H ₂ O ₂
3	40%	30%	30%	brown-purple	U(MoO ₄) ₂	UMo ₇ O ₂₂	partially hot HNO ₃ partially hot NaOH/H ₂ O ₂
4	50%	20%	30%	brown-purple-gray	UO ₂ , U(MoO ₄) ₂	Na ₄ U(MoO ₄) ₄	partially hot HNO ₃ /H ₂ O ₂ partially hot NaOH/H ₂ O ₂
5	60%	10%	30%	dark blue-purple	U(MoO ₄) ₂		Hot NaOH/H ₂ O ₂ partially hot HNO ₃ /H ₂ O ₂
6	60% MoO ₃ , 10% Na ₂ MoO ₄ , 30% UO ₂ washed with Na ₂ MoO ₄ heat to 1150 °C			green-gray	UO ₂	Na ₄ U(MoO ₄) ₄	Hot NaOH/H ₂ O ₂ partially hot HNO ₃ /H ₂ O ₂
7	50%	-	50%	purple	U(MoO ₄) ₂	UMo ₁₁ O ₃₅ UMo ₇ O ₂₂	Hot NaOH/H ₂ O ₂
8	70%	10%	20%	dark blue, purple	U(MoO ₄) ₂	UMo ₇ O ₂₂	Hot NaOH/H ₂ O ₂
9	30%	10%	60%	green-gray	UO ₂	Na ₄ U(MoO ₄) ₄	Hot HNO ₃ /H ₂ O ₂

Table 4.2 XRD results of uranium species precipitated from different compositions of MoO₃, Na₂MoO₄, and UO₂

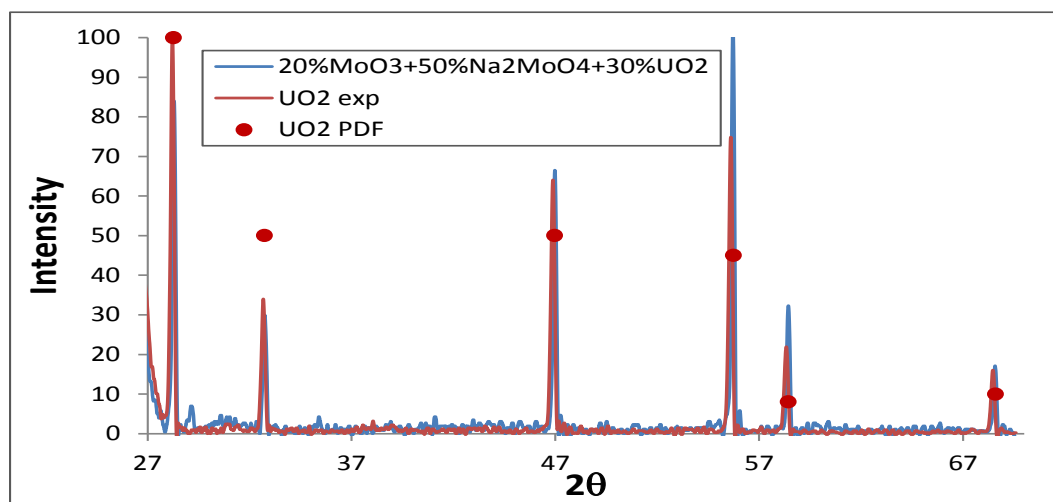


Figure 4.4 XRD pattern of uranium precipitate obtained from the salt mixture containing 20% MoO₃-50% Na₂MoO₄- 30%UO₂ heated to 1313 K and cooled to room temperature. This spectrum is compared to a UO₂ powder and a standard pattern for UO₂.

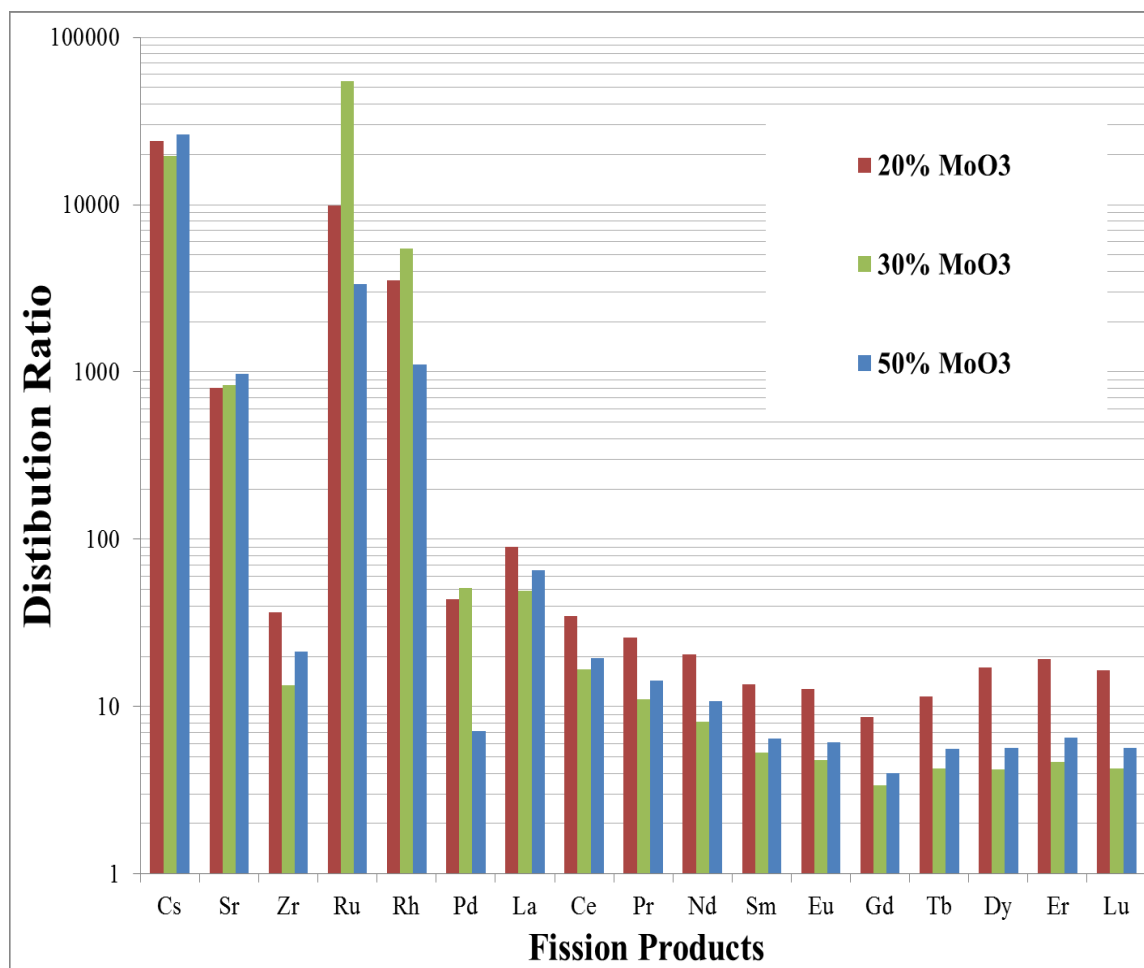


Figure 4.5 Distribution ratios for selected fission products at varying concentrations of MoO₃ and Na₂MoO₄, and constant 30% UO₂. Samples were heated to 1413 K and cooled to 1223 K at a rate of 38 K min⁻¹, and then were washed once with Na₂MoO₄.

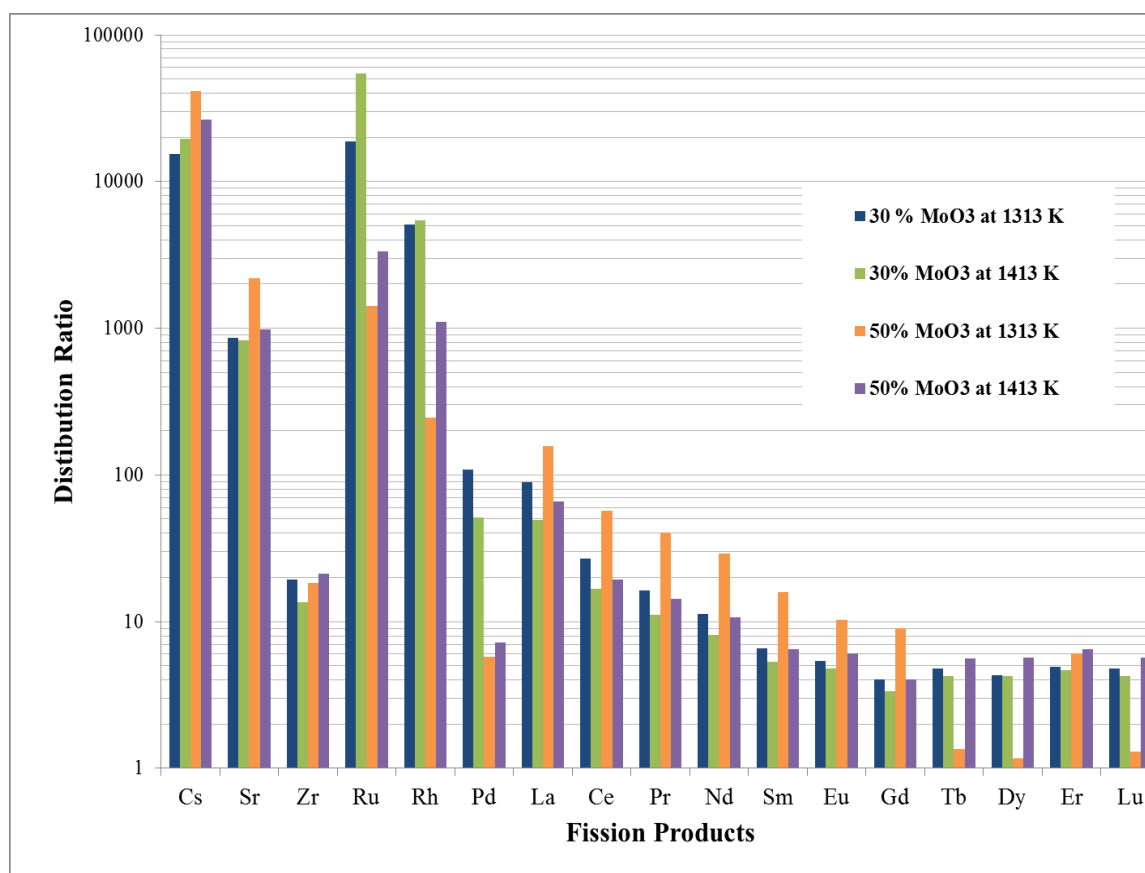


Figure 4.6 Distribution ratios of fission products from tests conducted at two dissolution temperatures followed by cooling at a rate of 38 k min^{-1} . Samples contain 30% MoO₃, 40% Na₂MoO₄, and 30% UO₂ and were washed once with Na₂MoO₄.

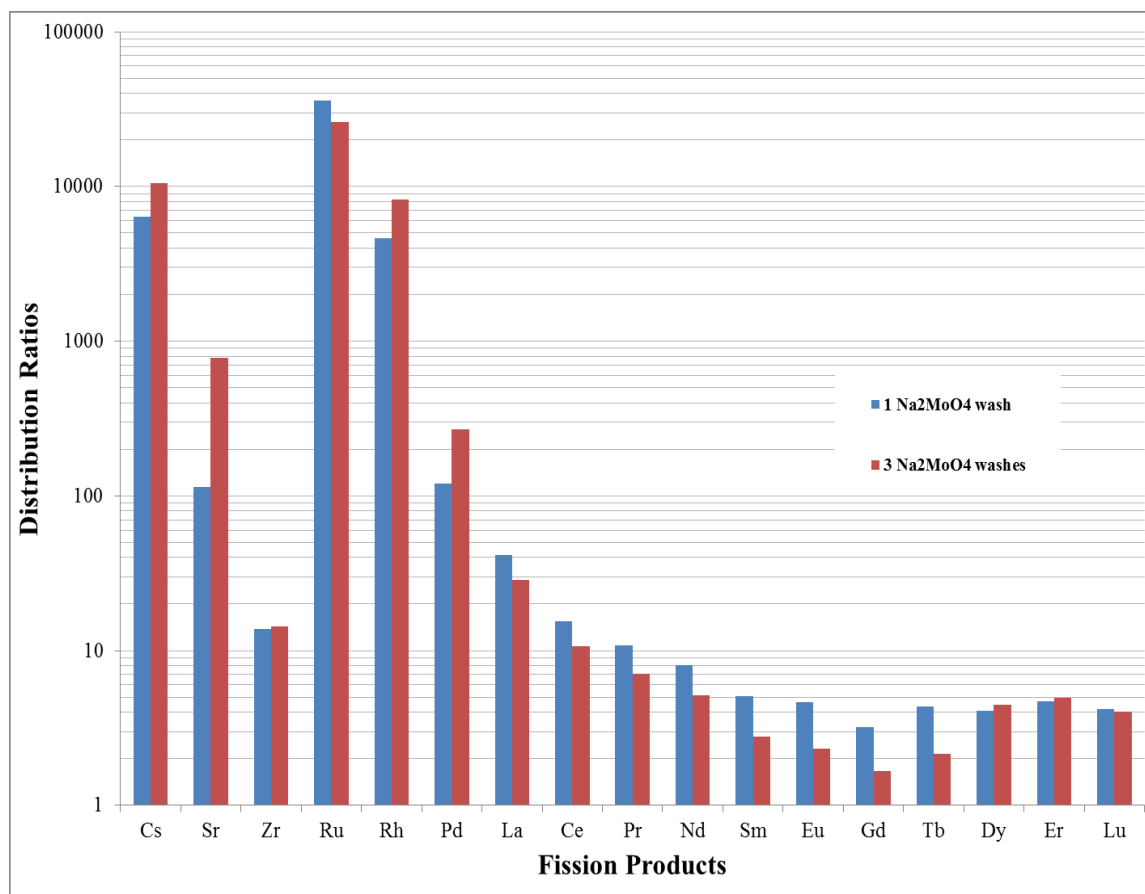


Figure 4.7 Distribution ratios of the fission products after uranium precipitate was treated with one or three Na₂MoO₄ washes. The precipitates were obtained from samples containing 30% MoO₃, 40% Na₂MoO₄, and 30% UO₂ that were heated to 1413 K and cooled to 1223 K at a rate of 38 K min⁻¹.

Chapter 5

Phase Equilibria Studies of the LiCl-KCl-UCl₃ System

Amber L. Hames^{1,2}, Alena Paulenova¹, James L. Willit², and Mark A. Williamson²

1. Oregon State University 1500 SW Jefferson St. Corvallis, OR 97331
2. Argonne National Laboratory 9700 S Cass Ave. Argonne, IL 60439

5.1. Abstract

An investigation into the phase equilibria in the LiCl-KCl-UCl₃ molten salt electrolyte used in electrorefining used nuclear fuel lead to the reevaluation of the LiCl-UCl₃, KCl-UCl₃ and the LiCl-KCl-UCl₃ phase diagrams. Samples of varying compositions within each of these systems were thermally analyzed by DSC to determine the temperature of the phase transitions. Samples were then analyzed by XRD to determine the identity of the phases formed, and ICP-OES to establish the cation ratio. The LiCl-UCl₃ system displayed a eutectic transition at 24.6 mol % UCl₃ and 75.4 mol% LiCl with melting at 763±2 K. The KCl-UCl₃ system displayed two eutectic transitions, one occurring at 19.25 mol% UCl₃ and 80.75 mol % KCl with melting at 827± 3 K, and another at 56.70 mol% UCl₃ and 43.30 mol % KCl with melting at 805 ± 4 K. The K₂UCl₅ phase was identified by DSC and XRD, while there was no evidence of a K₃UCl₆ phase. These LiCl-UCl₃ and KCl-UCl₃ phase diagrams were used to produce a portion of the LiCl-KCl-UCl₃ phase diagram. The LiCl-KCl-UCl₃ system displayed two ternary eutectics, one occurring at 32.7 mol % UCl₃, 41.96 mol% LiCl, and 25.34 mol % KCl with melting at 681.1 ± 5.9 K, and another occurring at 7.85 mol % UCl₃, 50.02 mol % LiCl, and 42.13 mol % KCl with melting at 619.3 ± 1.1 K. The evaluation of these phase diagrams allows for an improved understanding of the LiCl-KCl-UCl₃ system.

5.2. Introduction

The advanced technology of pyroprocessing allows for the recovery and recycle of actinides, especially transuranics, in used nuclear fuel. Pyroprocessing is unique from other used fuel treatment technologies in that it has the ability to handle short-cooled fuel, it has a small process footprint, and metallic uranium and transuranic (TRU) products can be directly fabricated into metallic fuel for advanced reactors. This process has the capability to recycle both used metallic and light water reactor (LWR) oxide fuel. The LWR fuel must first be electrochemically treated in a head end operation to reduce the oxides to their metallic form. The used metallic fuel is then loaded into the anode basket of the electrorefiner and submerged in the molten salt electrolyte consisting of LiCl-KCl-UCl₃, which allows for the dissolution of the used fuel. Metallic uranium and a U/TRU product are then electrodeposited onto two separate cathodes. [1-3] During this process,

contaminants in the used fuel consisting of lanthanides, alkali, and alkaline earth metals also anodically dissolve in the electrolyte, resulting in a buildup of fission products in the electrolyte. Additionally, a concentration gradient of UCl_3 develops at the anode-salt interface, and the cathode-salt interface when current is passed in the cell. The formation of ternary phases at either of these interfaces could impact the process of electrorefining by impacting the chemical activity, thus the redox potentials, of the uranium and transuranic elements in the molten salt electrolyte.

Multi-component electrolytes have multifarious thermodynamic properties due to the formation of ternary or more complex compounds. Establishing the fundamental phase equilibria provides insight into the characteristics of the LiCl-KCl-UCl_3 molten salt, which allows for an enhanced understanding of the behavior of the ever-changing electrolyte throughout the process of electrorefining. The goal of this work is to improve the fundamental understanding of the phase behavior of uranium, present as UCl_3 , in the LiCl-KCl-UCl_3 system.

5.2.1. LiCl-KCl

The LiCl-KCl system has been well characterized by many researchers. [4-16] The reported phase diagrams of the LiCl-KCl system are in good agreement with one another and show a eutectic composition between 57.0-59.5 mol% LiCl , and a eutectic temperature 625-634 K.[4-16]. Initial investigations of this system relied on visually examining the melting/crystallization temperatures during heating and cooling. [4-10] The evolution of thermal analysis instrumentation allowed for differential thermal analysis (DTA), and differential scanning calorimetry (DSC) to be used to determine the eutectic and melting temperatures [11-16]. DSC and DTA allow for precise measurements with high sensitivity and reproducibility giving rise to results that are typically more accurate than visual observations. [17] Re-evaluating the literature values of the eutectic by removing data collected by visual examinations, and only taking into consideration the data from DSC, DTA, and calculations, the literature gives a eutectic composition of 58.2-59.5 mol% LiCl and a temperature between 625-627 K. Since the most recent assessments of the LiCl-KCl phase diagram [11-16] are in very good agreement, re-investigation of this system was not deemed necessary.

5.2.2. LiCl-UCl₃

There is much less information available for the LiCl-UCl₃ system. The first known phase diagram for this system was produced by Barton *et al.* in 1959. Barton reported studying 17 samples of various LiCl-UCl₃ compositions using a method of thermal analysis not discussed.[18] A single eutectic at 25 mol% UCl₃, with a melting temperature of 763 ± 5 K was reported. Desyatnik *et al.* used cooling curve data from DTA studies to develop a phase diagram for this system, and reported a eutectic composition at 26.5 mol% UCl₃ with a melting temperature of 763 ± 2 K.[19] Ghosh *et al.* used Barton and Desyatnik's data with Gibbs energy modelling to model the LiCl-UCl₃ phase diagram. A single eutectic at 24.2 mol% UCl₃ with a melting temperature of 765 K was reported.[16] While the phase diagrams available for the LiCl-UCl₃ system are relatively consistent, the limited experimental information available on the LiCl-UCl₃ system led us to re-evaluate the system.

5.2.3. KCl-UCl₃

Literature available for the KCl-UCl₃ system is very inconsistent. The phase diagrams available for this system display contradictory eutectics, congruently and incongruently melting compositions, and number of phases formed. This system was first studied by Kraus in 1943.[20] Kraus slowly cooled samples and recorded the temperatures with a recording potentiometer to determine phase transitions. Kraus reported a considerable amount of error in the freezing points of a few samples due to supercooling. For the eutectic transitions, however, Kraus reported that most samples only contained a ± 5 K error. Small quantities, < 0.5%, of UCl₄ were reported in some of the samples of UCl₃. Kraus reported two eutectic compositions, one, e₁, at 20 mol % UCl₃ with a melting temperature of 863 ± 5 K, and another, e₂, at 50 mol % UCl₃ with a melting temperature at 818 ± 5 K. Kraus reported the appearance of additional thermal effects upon cooling at compositions consisting of less than 33.3 mol % UCl₃. It was reported that this second thermal effect was the transition of K₃UCl₆ to K₂UCl₅. The additional thermal effect was seen to have a marked maximum at 25 mol % UCl₃. [20, 21]

Thoma *et al.* studied this system, reporting significant differences with respect to Kraus' diagram. Thoma reported using thermal analysis and thermal gradient quenching to construct the KCl- UCl_3 phase diagram. Excess uranium metal was introduced to the compositions of KCl- UCl_3 studied to minimize the presence of U^{4+} , which Thoma concluded was the cause of the K_3UCl_6 phase in Kraus' diagram. Thoma concluded the phase Krause was calling K_3UCl_6 , was actually K_2UCl_6 . Samples without excess uranium metal were reported to behave identical to the samples studied by Kraus. Thoma reported two eutectics, e_1 , at 19 mol % UCl_3 melting at 833 K, and e_2 , at 55 mol % UCl_3 melting at 826 K. The phase K_3UCl_6 was not seen in experiments performed by Thoma. A "eutectic break" was however, reported to occur in sample compositions with UCl_3 greater than 55 mol %. The reason for this "eutectic break" was unknown. [94] Due to the addition of U metal to the system, Thoma was actually studying the KCl- UCl_3 -U ternary system thus, ~~Desyatnik may not be depicting the KCl- UCl_3 system by DTA and X-ray diffraction (XRD).~~ Desyatnik did not discuss whether heating or cooling data were used for phase transition temperature determination. Previous phase diagram experiments performed by Desyatnik used cooling data from DTA; therefore, it is assumed that cooling data was used for this diagram as well. [21] Desyatnik reported the existence of K_2UCl_5 and two eutectic compositions. A eutectic, e_1 , was found at 16 mol % UCl_3 with melting at 863 ± 2 K, and e_2 at 50 mol % UCl_3 with melting at 813 ± 2 K. [22]

Suglobova *et al.* used thermographic methods and XRD to study systems of alkali metal (M) chlorides with UCl_3 . Samples were analyzed in quartz ampoules, and cooling curves were used to determine phase transition information. After thermal analysis, the samples were analyzed by XRD to identify the phases present in the sample. Suglobova described that the congruently melting hexahalouranates (M_3UCl_6) decomposed to the pentahalouranates (M_2UCl_5) and an alkali halide at temperatures below 743 K. Suglobova's diagram suggests solid solution formation for K_3UCl_6 and decomposition of that phase to K_2UCl_5 and KCl at low temperature. If this decomposition occurs, an invariant line must extend from KCl past the decomposition point of K_3UCl_6 to the K_2UCl_5 phase. As drawn, this diagram violates phase rules. If the line separating the two two-phase regions is a boundary line, then this line cannot be horizontal. In addition, two two-phase regions cannot bound each other because a degree of freedom is

introduced by this line. [23] Suglobova reported two eutectics, e_1 at 22 mol % UCl_3 with melting at 863 K and e_2 at 50 mol % UCl_3 with melting at 813 K. The K_2UCl_5 phase was characterized by XRD and its melting point, 635 K. No such data existed for the K_3UCl_6 phase making its existence questionable. [24]

Ghosh *et al.* used Kraus', Suglobova's, and Thoma's data to reexamine the KCl-UCl_3 system using computer coupling of phase diagrams (i.e., CALPHAD approach). Ghosh determined that the K_3UCl_6 phase did not exist due to the lack of XRD data, and did not include K_3UCl_6 in the calculations. Ghosh calculated two eutectic compositions, e_1 at 18.6 mol % UCl_3 melting at 847 K and e_2 at 54 mol % UCl_3 melting 831 K. [16]

While the literature does agree on the presence of two eutectics in the KCl-UCl_3 system, the exact composition of these eutectics and their melting temperatures are inconsistent. Furthermore, the existence of the K_3UCl_6 phase is inconclusive. These discrepancies result in the need for the KCl-UCl_3 system to be reexamined experimentally using newer, more accurate techniques such as DSC.

5.2.4 LiCl-KCl-UCl₃

There is very limited information available for the ternary system. The LiCl-KCl-UCl_3 system was first investigated by Thamer. He used cooling curve data from DTA to determine the temperatures of the phase transitions within the system. Thamer addressed supercooling by agitating the samples above 973 K through an arc of 30 K at two cycles per second. Additional uranium metal in a ratio of $\text{U}^0/\text{U(III)} = 0.20$ was also added to ensure the absence of UCl_4 . Thamer's objective was to investigate molten salt samples that would lead to high breeding ratios in a reactor therefore only samples with high uranium concentrations were investigated. He only reported one eutectic in the high uranium concentration region of the diagram at 46% LiCl - 24% KCl - 30% UCl_3 with melting at 691 ± 2 K and the solidifying phases including LiCl , UCl_3 , and K_2UCl_5 . [25] Again, because of the additional U metal introduced to the system, Thamer was studying the $\text{LiCl-KCl-UCl}_3\text{-U}$ system rather than the LiCl-KCl-UCl_3 system that was reported.

Desyatnik *et al.* also studied the ternary system. Samples of various compositions were heated in closed quartz tubes until the samples were melted. The processes occurring during cooling, at a cooling rate of $3\text{-}6 \text{ K min}^{-1}$, were simultaneously recorded

on photographic paper. Liquidus transitions of the LiCl-KCl [20], LiCl-UCl₃ [32], and KCl-UCl₃ [30] binary phase diagrams were used along with the experimental results to calculate the ternary system. Four solidifying phases were determined consisting of LiCl, KCl, K₂UCl₅ and UCl₃. This ternary diagram could be divided into two secondary subsystems by a triangulating section of LiCl-K₂UCl₅, which consisted of LiCl-K₂UCl₅-UCl₃, and LiCl-KCl-K₂UCl₅. The LiCl-KCl-K₂UCl₅ system was reported to contain a simple eutectic with a composition of 29.5 mol% LiCl, 58.5 mol% KCl, 12 mol% UCl₃ melting at 608 ± 2 K. The LiCl-K₂UCl₅-UCl₃ system was reported to also have a simple eutectic with a composition of 38 mol% LiCl, 30.5 mol% KCl, and 31.5 mol% UCl₃ melting at 668 ± 2 K. [26]

Nakayoshi *et al.* studied the LiCl-KCl eutectic-UCl₃ system, and developed a partial phase diagram for the LiCl-KCl-UCl₃ system. The objective of Nakayoshi's work was to investigate accidental cooling of an electrorefiner salt that is, to determine the temperature at which the salt would begin to freeze. Nakayoshi studied 20 samples by analyzing heating curves from DTA and phase information from XRD. The diagram was said to consist of two boundary lines, one connecting to the LiCl-K₂UCl₅ system, and the other line connecting to the LiCl-KCl eutectic-17mol% UCl₃. Nakayoshi examined the samples for the existence of the two eutectics Desyatnik reported. There was no evidence of the first eutectic Desyatnik reported, and the second eutectic reported was reported to have a slightly different composition and a melting temperature not corresponding to the temperature reported by Desyatnik's. Because the scope of this work was to determine the temperature at which the electrolyte would crystallize during accidental cooling of the electrorefiner, the exact eutectic temperatures and compositions were not of interest, and thus were not reported. [27]

Ghosh reported [27] Nakayoshi's, and Thamer's data in CALPHAD simulations along with two compositions of the LiCl-KCl eutectic with different concentrations of UCl₃ that were examined by heating curves of DTA and DSC to calculate a ternary diagram. Ghosh reported the projected liquidus diagram, which was said to be close to Desyatnik's and Nakayoshi's findings. Two eutectic compositions were reported, E₁, at 45.6 mol% LiCl, 21.5 mol% KCl, 33.1 mol% UCl₃ melting at 702 K, and E₂ at 57.6 mol% LiCl, 41.9 mol% KCl, 0.468 mol% UCl₃ at 625 K. Ghosh also reported a monovariant eutectic reaction at 746 K with the LiCl-KCl eutectic and 18 mol% UCl₃. [16]

While all reports agree that the liquidus ternary diagram consists of two boundary lines, one for the LiCl-K₂UCl₅-UCl₃ system, and the other of the LiCl-KCl-K₂UCl₅ system, the eutectic compositions and temperatures reported for these systems are contradictory. This ternary system is of importance in understanding the behavior of the electrolyte used in the electrorefiner so we experimentally studied the region of the diagram important to electrorefiner operation. However before we studied the ternary system, the binary systems of LiCl-UCl₃ and KCl-UCl₃ had to be reassessed.

5.3. Experimental

5.3.1. UCl₃ Synthesis

Uranium trichloride synthesis was performed in an argon glovebox. Uranium dendrites from previous electrorefining tests and 99.99% NH₄Cl (Sigma Aldrich) were loaded into a reaction vessel consisting of a closed-end quartz tube. The tube was placed in a furnace with a thermocouple situated next to the sample located in the tube and near the reaction zone. The open end of the quartz tube was connected to a large Pyrex tube. The Pyrex tube was connected to a vacuum via a hose to trap any vapors produced during the reaction, allowing for gas evolution without over-pressurizing the system. A Viton O-ring sealed the quartz tube and the Pyrex tube. The O-ring was designed to leak in the case of over-pressurization. The dendrites and excess ammonium chloride were loaded into the vessel in a ratio of about 6 NH₄Cl: 1 UCl₃. The vessel was evacuated and heated to 573 K for 30 hours. At this point a bright green (NH₄)₂UCl₆ was synthesized and sampled for characterization by DSC and thermogravimetric analysis (TGA). DSC and TGA revealed that the (NH₄)₂UCl₆ decomposed to UCl₄ at 608 K. The product was then heated under vacuum at 623 K for 10 hours. The NH₄Cl sublimed from the sample leaving an olive green UCl₄ product, which was confirmed by XRD and DSC. Uranium dendrites and the UCl₄ were then loaded into a nickel crucible, which was loaded into the reaction vessel and heated under a vacuum at 823 K for 10 hours to allow the dendrites to reduce the UCl₄ to UCl₃. The reduction was previously attempted in the quartz tube without the nickel crucible; however, the final product contained substantial oxychloride contamination. The final UCl₃ product was analyzed by DSC and XRD.

5.3.2. DSC-TGA

Several different mixtures of high purity LiCl and/or KCl with the UCl_3 were ground together with a mortar and pestle in an argon atmosphere glovebox. Samples of about 10-20 mg were loaded into gold cells, and hermetically sealed using a cell press. The samples were thermally analyzed on a Netzsch STA 449 C Jupiter. The simultaneous thermal analysis (STA) combines the capabilities of the DTA, DSC and TGA. The sample crucible and an empty reference crucible were situated on a platinum sample carrier with a type S thermocouple. The samples were initially thermally cycled at a rate of 20 K min^{-1} to initiate melting, and ensure homogenization. The following two thermal cycles were run at a rate of 5 K min^{-1} , which allowed for the identification of the transition temperatures of the material. The data was analyzed using the Netzsch Proteus Analysis software. Data from the heating curves were used for transition temperatures determination, as the cooling curves displayed a large degree of supercooling.

5.3.3. ICP-OES

Inductively coupled plasma optical emission spectrometry (ICP-OES) was used to determine ratio of U:Li:K in the samples after they were thermally cycled. After thermal analysis, the samples were removed from the glove box, and dissolved in nitric acid. The samples were analyzed with the Perkin Elmer Optima 8300 ICP-OES to determine the U: K: Li ratios.

5.3.4. XRD

Several samples were analyzed by XRD to determine the phases formed during thermal cycling. After a sample was thermally cycled, the sealed cell was cut open, and the sample was loaded onto a single well glass slide coated with two layers of double-sided tape inside of the argon glovebox. A Kapton film was placed onto the slide to envelop the slide and sample. The slide was removed from the glovebox, and analyzed on the XRD.

5.4. Results and Discussion

5.4.1. LiCl- UCl_3 System

Samples of varying compositions of LiCl- UCl_3 were thermally cycled on the DSC. After thermal analysis was completed, the samples were analyzed for the U:Li ratio by ICP-OES. The phase diagram drawn from the DCS heating curves with the actual data points from DSC is given

in figure 5.1. In figure 5.2, data from the LiCl-UCl₃ phase diagrams developed by Barton *et al.* [18], Desyatnik *et al.* [19], and Ghosh *et al.* [16] are compared against the phase diagram developed from the ten samples analyzed in this study. The phase diagram based on our experimental data is in very good agreement with the literature. As shown in figure 5.1, the samples exhibited a solidus transition at 763 ± 2 K, which is consistent with the eutectic melting temperature found by Desyatnik, Barton and Ghosh. The eutectic composition was 24.6 mol % UCl₃ and 75.4 mol% LiCl, which is consistent with the composition cited by Barton, Desyatnik, and Ghosh. The compositions and temperatures found for the eutectic transition are compiled in table 5.1. Figure 5.3 displays a DSC curve for a sample 13.24 ± 0.03 mol% UCl₃. The eutectic temperature was found by extrapolating the onset temperature of the eutectic peak. The onset temperature is extrapolated from the auxiliary line that ascends from the peak slope and intersects the baseline. [17] The liquidus temperature was taken as the onset temperature of the baseline shift [17, 27]. As shown in figure 5.3, there is a large degree of supercooling (20-25 K) for the data collected from the DSC cooling curve thus we used data from heating curves for phase transition temperature determinations. These results validated the thermal analysis technique of finding the solidus transition from the intersection of the tangents of the baseline and endothermic peak, and the liquidus transition from the extrapolation of the endpoint of the second broad peak. [17] Overall, our data confirms Barton's, Desyatnik's, and Ghosh's phase diagrams for the LiCl-UCl₃ system.

5.4.2. KCl-UCl₃ System

Twenty samples of varying compositions of KCl-UCl₃ were thermally cycled on the DSC. After thermal analysis was complete, the samples were analyzed for the U:K ratio by ICP-OES, or analyzed for their crystal structures by XRD. The phase diagram drawn from the DSC heating curve data points is given in figure 5.4. Figure 5.5 displays the phase diagram with the literature data points overlaid on the phase diagram. Our phase diagram is similar to Ghosh's phase diagram in that there are two eutectics and a congruently melting compound. We found a eutectic to occur at 19.25 ± 0.12 mol% UCl₃ with melting at 827 ± 3 K, and another eutectic to occur at 56.70 ± 0.53 mol% UCl₃ with

melting at 805 ± 4 K. The compositions and temperatures found for the eutectic transitions compared to the literature values are given in table 5.2.

The eutectic transitions observed in this study appear to be in agreement with Thoma's data. Thoma used nickel crucibles that do not interact with the KCl- UCl_3 system. It is possible, due to the interaction of quartz and UCl_3 at these high temperatures, that Suglobova and Desyatnik had oxychloride contaminants in their samples. The K_3UCl_6 phase was reported by Kraus and Suglobova in areas of low UCl_3 concentrations (<25 mol%). Both Kraus and Suglobova used cooling data to develop their phase diagrams and reported an extra thermal effect to be the existence of the K_3UCl_6 phase [20, 24].

Figure 5.6 displays the XRD analysis of a sample of 10 mol% UCl_3 -KCl after the sample was thermally cycled by DSC. As seen in Figure 5.6, this data shows the KCl and K_2UCl_5 phases, with no additional phase such as K_3UCl_6 . Thoma reported this second thermal effect to be the byproduct of the disproportionation of UCl_3 to U and UCl_4 upon melting. Samples of 11 mol% UCl_3 -KCl with and without excess uranium metal were heated in a Ni crucible to 1073 K to determine if the proposed disproportionation reaction was occurring in the system. After heating to 1073 K and cooling to room temperature, the samples were analyzed by XRD to determine if evidence of the disproportionation, such as K_2UCl_6 or U metal, existed. For the sample with the excess uranium metal, the uranium dendrite was removed before XRD analysis. Neither sample contained K_3UCl_6 , K_2UCl_6 , or U. According to Thames and Thoma, if disproportionation was to occur, it would have happened in the sample without the excess U metal, and U metal would have been seen in the XRD of our sample as a byproduct. Because U metal was not seen in the sample without excess U-metal, and because additional thermal effects were not seen during the heating cycle of the DSC analysis of this sample, we believe that disproportionation is negligible.

Additional experiments were performed to synthesize K_3UCl_6 . Samples consisting of 10 mol% UCl_3 and 90 mol% KCl were heated in the furnace past the melting point for that composition, cooled to a temperature below the eutectic temperature, and held at this temperature overnight. The sample was cooled and a sample evaluated on the XRD to observe the phases formed. Only K_2UCl_5 and KCl were seen in this sample. Similarly, a sample was prepared and quenched, and then evaluated by XRD. Again, no evidence of K_3UCl_6 was found.

in the diffraction pattern. A test was performed on the DSC to see if the K_3UCl_6 transition could be seen after a long anneal. Only the eutectic and liquidus transitions were seen on both heating and cooling, giving no evidence of the K_3UCl_6 .

Five of the total twenty samples studied displayed additional thermal effects upon cooling. An example of a sample displaying an additional thermal effect is displayed in Figure 5.7. The sample was thermally cycled at a rate of 5 K min^{-1} , and two distinguishable peaks appeared for the eutectic transition while the crystallization peak also showed additional thermal effects. The same sample was thermally cycled at a rate of 2 K min^{-1} . When the heating and cooling rates were 2 K min^{-1} , the additional peaks displayed on the cooling curves appeared to merge into a single peak. Upon further investigation of the samples displaying added thermal effects upon cooling, it was noted that all of these samples weighed less than 10 mg. In such small samples, it is possible that when the sample melts, the liquid forms individual droplets that upon cooling display individual degrees of supercooling. When the cooling rate is slowed down, the effects of supercooling are reduced. Decreasing the effects of supercooling limits the degree of supercooling exhibited by the individual droplets, which could explain the reason that individual peaks during cooling form one peak as the cooling rate is decreased.

The diagram reported in figure 5.4 is the most up-to-date phase diagram for the $KCl-UCl_3$ system developed from experimental data. Since this diagram was developed using DSC heating curve data to avoid supercooling or nucleation effects and samples were analyzed by ICP-OES and XRD, it is the most up-to-date experimentally determined diagram for the $KCl-UCl_3$ system.

5.4.3. LiCl-KCl- UCl_3 System

The ternary phase diagram in figure 5.8 was drawn from the Sangster's LiCl-KCl binary diagram [12], and the LiCl- UCl_3 and KCl- UCl_3 binary diagrams generated in this study. Ten samples of varying compositions of LiCl-KCl- UCl_3 were thermally cycled on the DSC, and their heating curves were used to verify the features of this diagram. After the samples were thermally analyzed, they were analyzed by ICP-OES for the Li:K:U ratios. Two ternary eutectics were identified. A eutectic was found at 32.7 mol% UCl_3 , 41.96 mol% LiCl, and 25.34 mol % KCl with melting at $681.1 \pm 5.9\text{ K}$. Another eutectic

was found at 7.85 mol % UCl_3 , 50.02 mol % LiCl , and 42.13 mol % KCl with melting at 619.3 ± 1.1 K. Figure 5.9 displays the ten samples thermally analyzed, as well as data from Thamer [25] and Nakayoshi [27]. In general, both Thamer's and Nakayoshi's data were consistent with our phase diagram.

Table 5.3 compares the eutectics found in this study, to those in the literature. Eutectic, E1, is very similar to the eutectic reported by Thamer. The other eutectic, E2, has a composition and melting temperature that varies from the reported literature values, however, the compositions and melting temperatures found in the literature are not in agreement with one another. In the current experiments, this eutectic transition was very precise in that the results only varied by 1.1 K. While Nakayoshi studied samples that displayed this eutectic transition, the exact temperature at which this ternary eutectic was seen in his samples was never reported; however, in his phase diagram, it appeared that this ternary eutectic occurred at 820 K.

Figure 5.10 displays the DSC heating curve for a sample off a eutectic composition of 67.85 mol% UCl_3 , 4.8 mol % LiCl , and 27.35 mol% KCl . Notice that the sample displays two endothermic peaks, and a baseline shift. The first endothermic peak is the E₁ ternary eutectic transition. This transition is the eutectic transition. The second endothermic transition occurring at 806 K is the result of the melting of UCl_3 and K_2UCl_5 in equilibrium with the liquid. The baseline shift is the melting of K_2UCl_5 in equilibrium with the sample of the rest of the sample. All samples on the right of the alkemade line, the line extending from K_2UCl_5 to LiCl , will display E₁ transition. All samples to the left of the alkemade line will inhibit the E₁ transition.

A sample of about 20 mol% LiCl , and 68 mol% KCl was analyzed by XRD after the sample was thermally cycled. As seen in figure 5.11, the sample very clearly displays K_2UCl_5 , KCl , and LiCl . There are no additional phases that appear.

Figures 5.12 and 5.13 show the isothermal projection of the LiCl-KCl-UCl_3 system at 773 K and 823 K, respectively, which is within the normal operating temperature for electrorefining. During uranium polarization experiments related to electrorefining studies, a K_2UCl_5 film formed on the anode that reduced the current density and caused a passive region of overpotential at the anode. [135] As shown in figures 5.12 and 5.13, the phase K_2UCl_5 participates in all equilibria at high uranium concentrations. Specifically, the liquid salt – K_2UCl_5 two-phase equilibria is consistent with the behavior observed at the uranium anode – electrolyte

interface during uranium electrorefining. In addition, the binary diagram shown in Figure 5.4 shows that K_2UCl_5 is a solid at the temperatures below approximately 900 K.

5.5. Summary

This ternary phase diagram, developed from experimental data for the LiCl-KCl- UCl_3 system, is the most accurate for the LiCl-KCl- UCl_3 system due to the combined use of DSC measurements, using heating data to avoid supercooling or nucleation effects, and sample analysis by ICP-OES and XRD.

The fundamental phase behavior of the LiCl-KCl- UCl_3 system is important for predicting the behavior of the electrolyte at the electrode-electrolyte interface during electrorefining used nuclear fuel. This study re-evaluated the two binary systems, LiCl- UCl_3 and KCl- UCl_3 . The LiCl- UCl_3 system displayed a eutectic transition at 24.6 mol % UCl_3 and 75.4 mol% LiCl with melting at 763 ± 2 K. The resulting phase diagram is consistent with the literature. The LiCl- UCl_3 system displayed two eutectic transitions. A eutectic was seen at 19.25 mol% UCl_3 and 80.75 mol % KCl with melting at 827 ± 3 K. Another eutectic was seen at 56.70 mol% UCl_3 and 43.3 mol % KCl with melting at 805 ± 4 K. The K_2UCl_5 transition was observed melting at 635 K in DSC and XRD. No evidence of a K_3UCl_6 phase was observed. The LiCl-KCl- UCl_3 system displayed two ternary eutectics. A eutectic, E_1 , was seen at 32.7 mol % UCl_3 , 41.96 mol% LiCl, and 25.34 mol % KCl with melting at 681.1 ± 5.9 K. Another eutectic, E_2 , was seen at 7.85 mol % UCl_3 , 50.02 mol % LiCl, and 42.13 mol % LiCl with melting at 619.3 ± 1.1 K.

5.6. Acknowledgements

The submitted manuscript has been created by U Chicago Argonne, LLC, Operator of Argonne National Laboratory (“Argonne”). Argonne, a U.S. Department of Energy Office of Science laboratory, is operated under Contract No. DE-AC02-06CH11357. The U.S. Government retains for itself, and others acting on its behalf, a paid-up nonexclusive, irrevocable worldwide license in said article to reproduce, prepare derivative works, distribute copies to the public, and perform publicly and display publicly, by or on behalf of the Government. Argonne National Laboratory’s work was supported by the U.S. Department of Energy, Office of Nuclear Energy, under contract DE-AC02-06CH11357.

5.7. References

1. Laidler, J.J., et al., *Development of pyroprocessing technology*. Progress in Nuclear Energy, 1997. **31**(1): p. 131-140.
2. Williamson, M.A. and J.L. Willit, *Pyroprocessing Flowsheets for Recycling Used Nuclear Fuel*. Nuclear Engineering and Technology, 2011: p. Medium: X; Size: 329-334.
3. McPheeters, C.C., R.D. Pierce, and T.P. Mulcahey, *Application of the pyrochemical process to recycle of actinides from LWR spent fuel*. Progress in Nuclear Energy, 1997. **31**(1): p. 175-186.
4. Zemczuzny, S. and F. Rambach, *Schmelzen der Alkalichloride*. Zeitschrift für anorganische Chemie, 1910. **65**(1): p. 403-428.
5. Richards, T.W. and W.B. Meldrum, *THE MELTING POINTS OF THE CHLORIDES OF LITHIUM, RUBIDIUM AND CAESIUM, AND THE FREEZING POINTS OF BINARY AND TERNARY MIXTURES OF THESE SALTS, INCLUDING ALSO POTASSIUM AND SODIUM CHLORIDE*. Journal of the American Chemical Society, 1917. **39**(9): p. 1816-1828.
6. Schaefer, W., Neues Jahrb. Mineral., Geol., Paleontol., Beil, 1920. **43**: p. 132.
7. Keitel, H., *Über die ternären Systeme aus Lithium-, Kalium-, Rubidiumchlorid und Kalium-,Rubidium, Cäsiumchlorid*. Neues Jahrb. Mineral., Geol., Paleontol., Beil, 1925. **52**: p. 378-423.
8. Elchardus, E. and P. Laffitte, *Etude thermique des systJmes KCl-BaCl₂ et KCl-LiCl*. Bull. Soc. Chim.(France), 1932. **51**: p. 1572-9.
9. Unzakov, G.M., DAN SSSR. . **87**: p. 791.
10. Bergman, E.K.A.A.G., Izv. SFKhA, 1954: p. 255.
11. Cook, E.L.W., Phase Diagram for Ceramists, 1989. **7**(The Am, Soc. Inc.).
12. Sangster, J. and A.D. Pelton, *Phase diagrams and thermodynamic properties of the 70 binary alkali halide systems having common ions*. Journal of physical and chemical reference data, 1987. **16**(3): p. 509-561.
13. Kaplun, A.B. and A.B. Meshalkin, *Study of phase equilibria in salt and oxide systems by the oscillation method of phase analysis*. Journal of Thermal Analysis and Calorimetry, 2008. **92**(3): p. 687-690.
14. Basin, A.S., et al., *The LiCl-KCl binary system*. Russian Journal of Inorganic Chemistry, 2008. **53**(9): p. 1509-1511.
15. Korin, E. and L. Soifer, *Thermal analysis of the system KCL-LiCl by differential scanning calorimetry*. Journal of thermal analysis, 1997. **50**(3): p. 347-364.
16. Ghosh, S., et al., *Experimental investigations and thermodynamic modelling of KCl-LiCl-UCl 3 system*. Calphad, 2014. **45**: p. 11-26.
17. Hörne G., H.W.F., Flammersheim H.J., *Differential Scanning Calorimetry*, ed. S.-V.B. Heidelberg. 2003.
18. C.J. Barton, A.B.W., W.R. Grimes, *Phase Diagrams of Nuclear Reactor Materials*, in U.S.A.E.C., Report No. ORNL-2548 Contract No. W-7405. 1959, Oak Ridge National Laboratory: Oak Ridge, Tennessee.

19. Desyatnik, V.N., et al., *Fusibility diagrams of systems involving lithium chloride, uranium trichloride, and uranium tetrachloride*. Soviet Atomic Energy, 1972. **32**(6): p. 563-564.
20. Kraus, C.A., *Phase Diagram of Some Complex Salts of Uranium with Halides of the Alkali and Alkaline-Earth Metals*, in *Manhattan Project Report- 'No. 251*. July 13, 1943.
21. R.E. Thoma, H.I., H. A. Friedman, G. D. Brunton, G. M. Hebert, T. N. McVay, *Reactor Chemistry Division Annual Progress Report ORNL- 3789*, W.R. Grimes, Editor. 1965.
22. Desyatnik V.N. , D.V.B., Raspopin S.P. , *Interaction of Uranium Trichloride with Alkali Metal Chlorides*. Russian Journal of Physical Chemistry, 1973. **47**(10): p. 1538-1539.
23. Okamoto, H. and T.B. Massalski, *guidelines for binary phase diagram assessment*. Journal of Phase Equilibria, 1993. **14**(3): p. 316-335.
24. Chirkst, I.G.S.a.D.E., *Phase Diagrams of Uranium Trichloride- Alkali Metal Chloride Systems*. Koordinatsionnaya Khimiya, 1981. **7**(1): p. 97-102.
25. B.J., T., *Freezing Points of Some Ternary Mixtures Derived from 55 mol% UCl₃-45 mol% KCl*, in *Technical Report, LA-3579-MS*, L.A.N. Laboratory, Editor. 1966.

26. V.N. Desyatnik, B.V.D., *Thermographic Study of the Ternary Systems Formed by Lithium Chlorides, Sodium Chloride, Potassium Chloride, Uranium Trichlorides, And Uranium Tetrachloride*. Zhurnal Prikladnoi Khimii 1975. **48**(4): p. 885-887.
27. Nakayoshi, A., et al., *Investigation of a LiCl–KCl–UCl₃ system using a combination of X-ray diffraction and differential thermal analyses*. Journal of Nuclear Materials, 2013. **441**(1–3): p. 468-472.
28. Rose, M.A., M.A. Williamson, and J. Willit, *Investigation of residual anode material after electrorefining uranium in molten chloride salt*. Journal of Nuclear Materials, 2015. **467**, Part 2: p. 576-581.

5.8. Figures

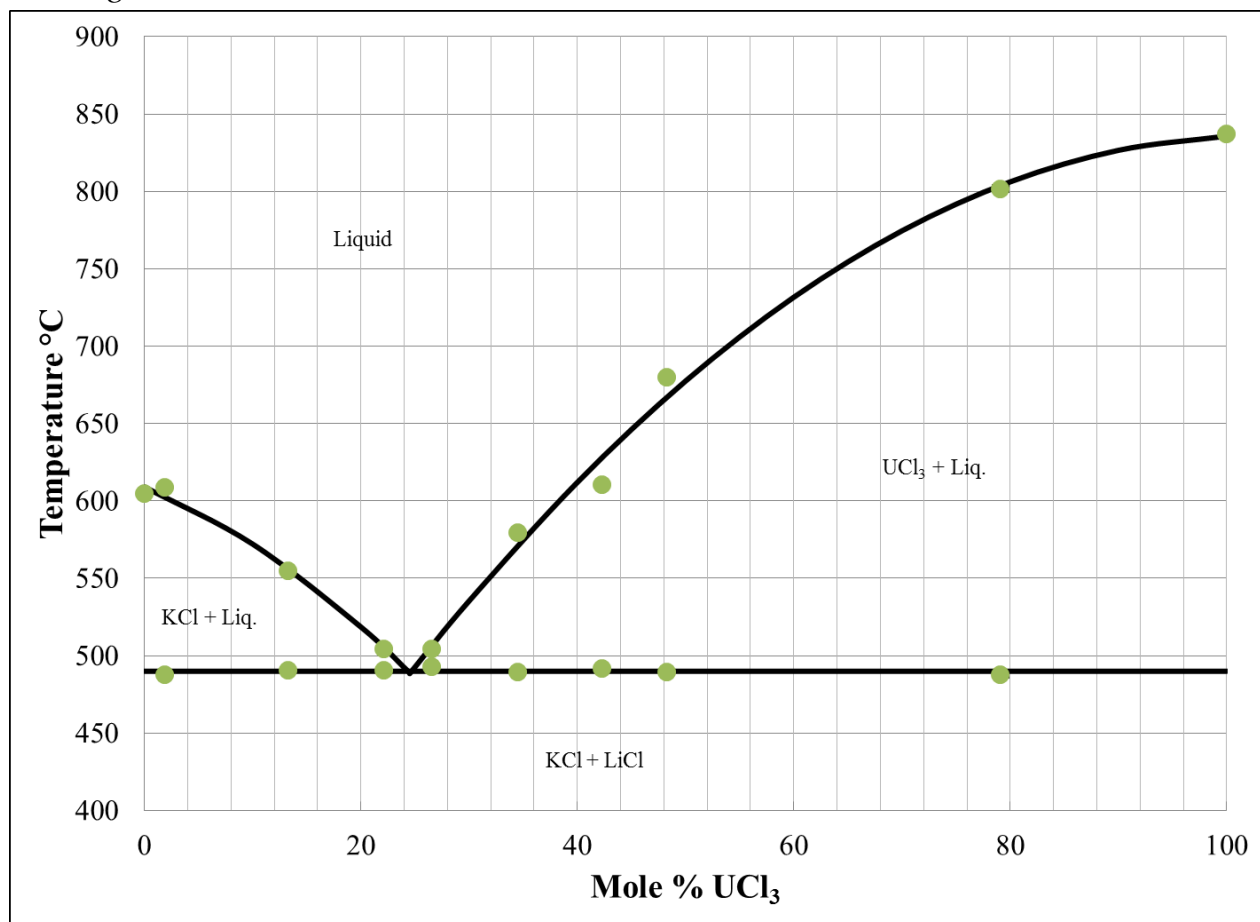


Figure 5.1 LiCl-UCl₃ phase diagram drawn from DSC heating curve data with actual data points overlaid.

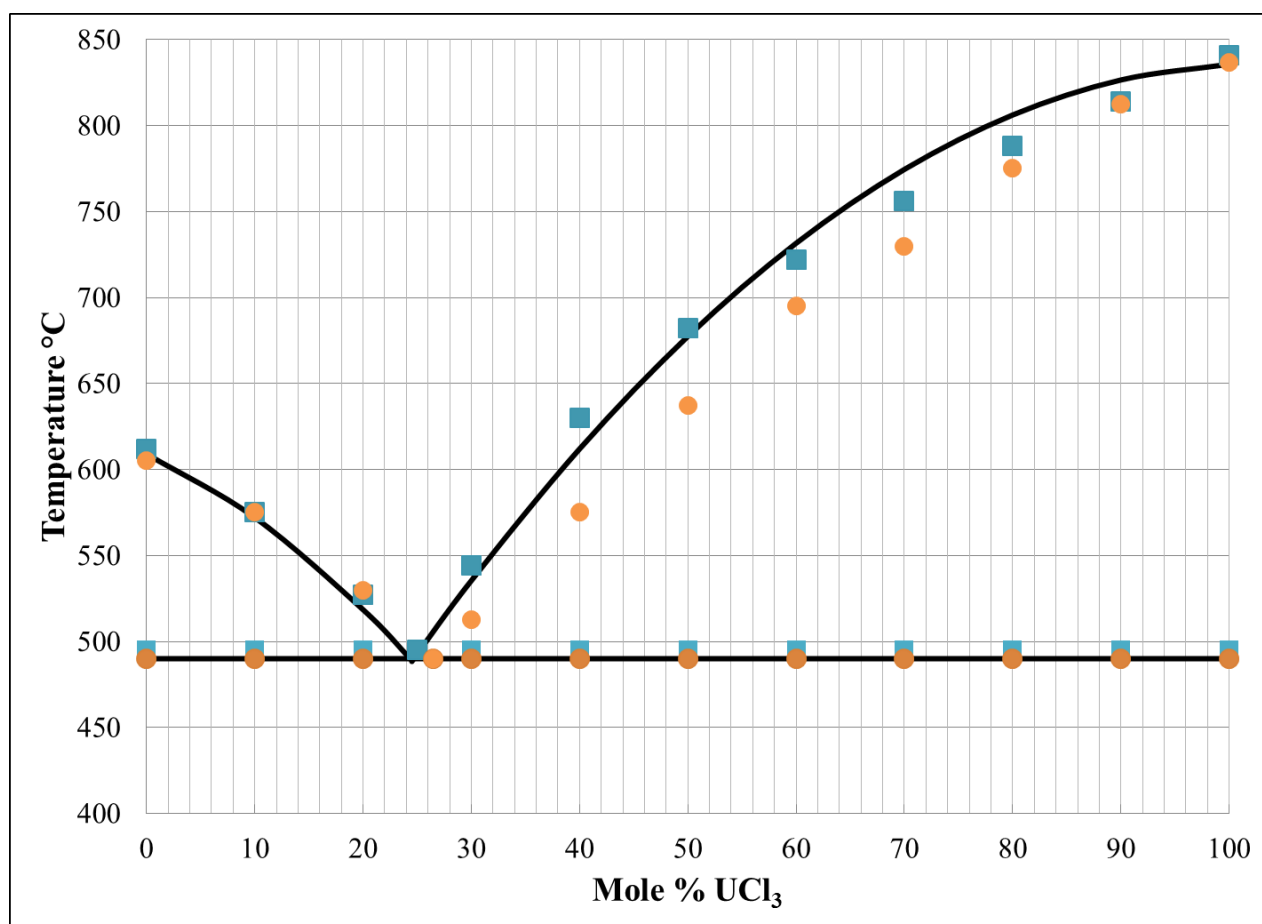


Figure 5.2 LiCl-UCl₃ phase diagram drawn from DSC heating curve data with data points from previous phase diagrams by Barton (blue squares) [18], and Desyatnik (orange circles) [19], and Ghosh (green triangles) [16].

Reference	Eutectic Composition (mol% UCl ₃)	Eutectic Transition Temperature (K)
Desyatnik [19]	26.5	763 ± 2
Barton [18]	25	768 ± 5
Ghosh [16]	24.2	765
This study	24.6 ± 0.6	763 ± 2

Table 5.1 Experimental results and literature values of eutectic composition and melting temperature for the LiCl-UCl₃ system

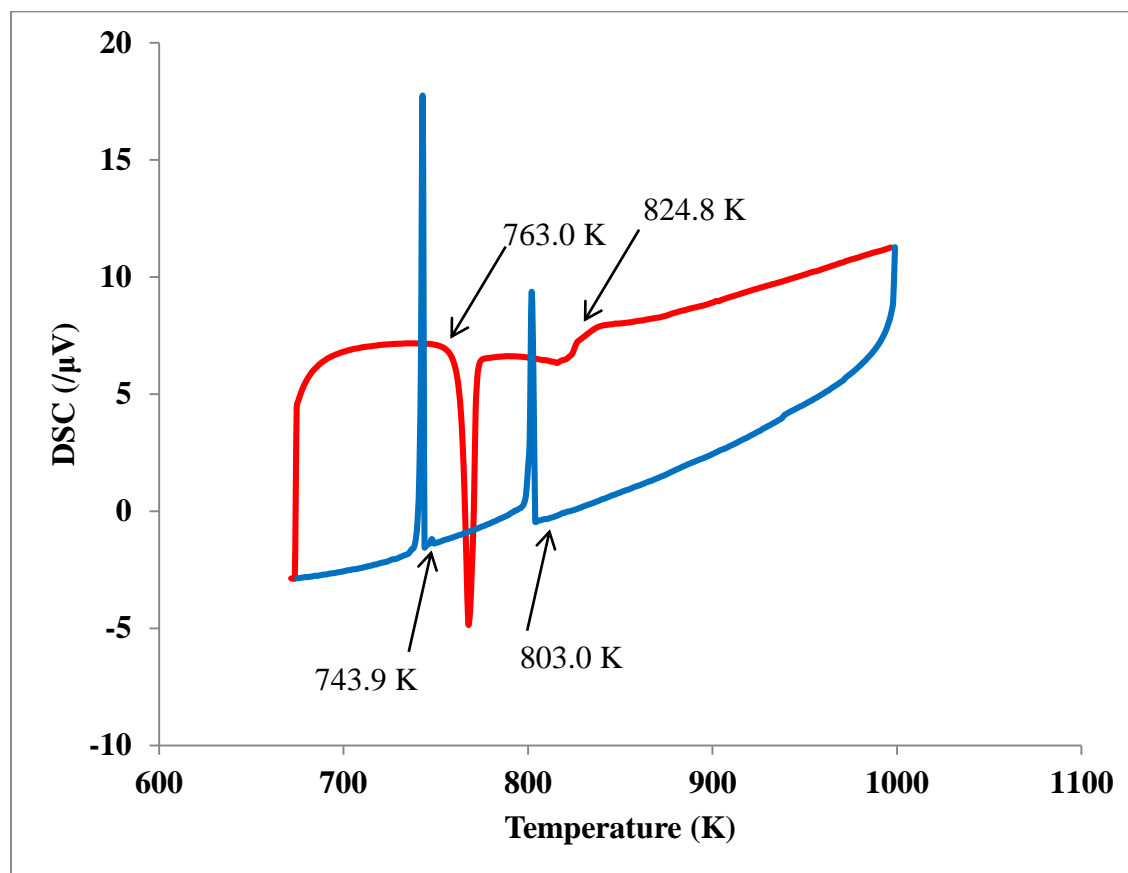


Figure 5.3 DSC curves for a sample of 13.24 ± 0.03 mol% UCl_3 . The heating curve is shown in red, while the cooling curve is shown in blue.

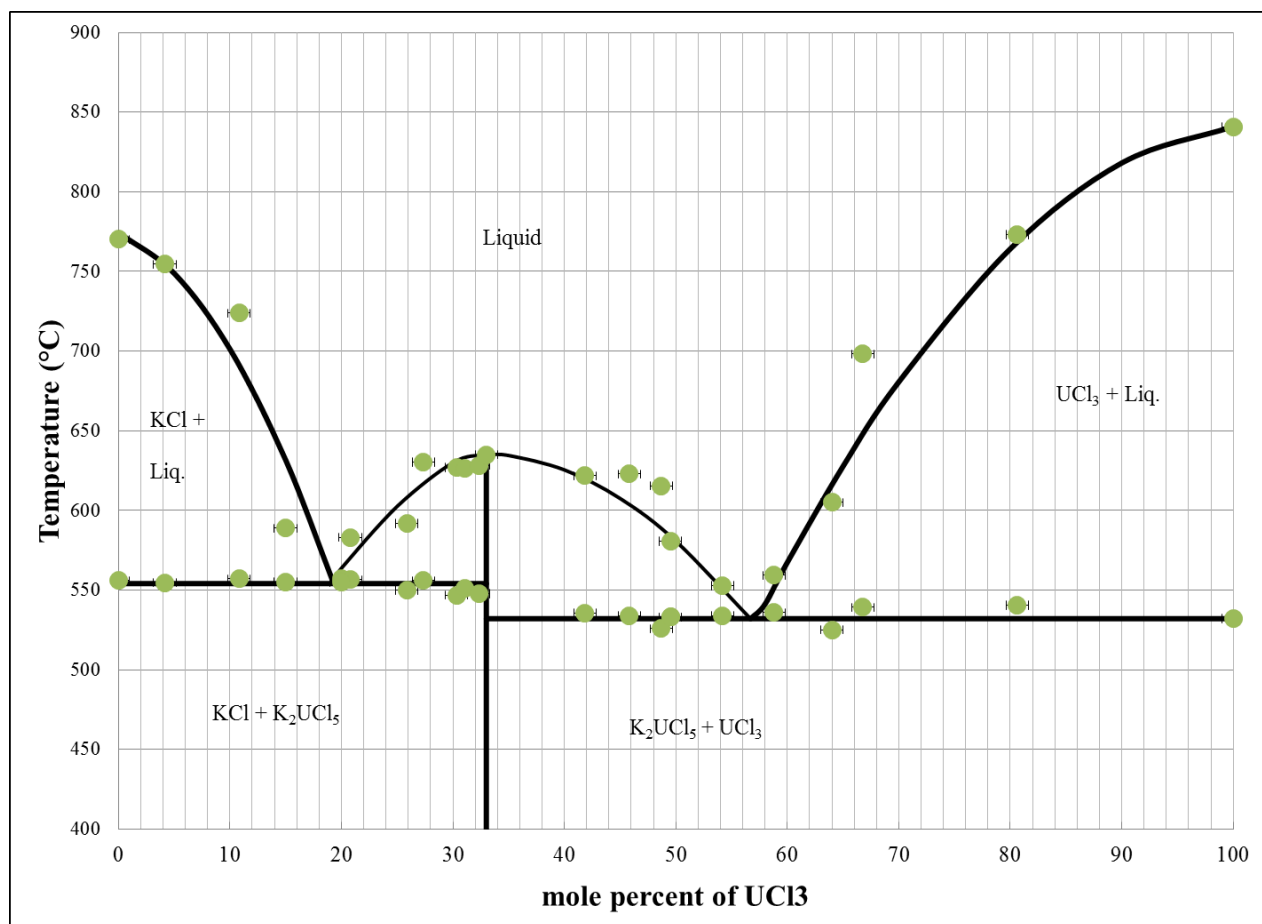


Figure 5.4 KCl-UCl₃ phase diagram drawn from DSC heating curve data with actual data points overlaid.

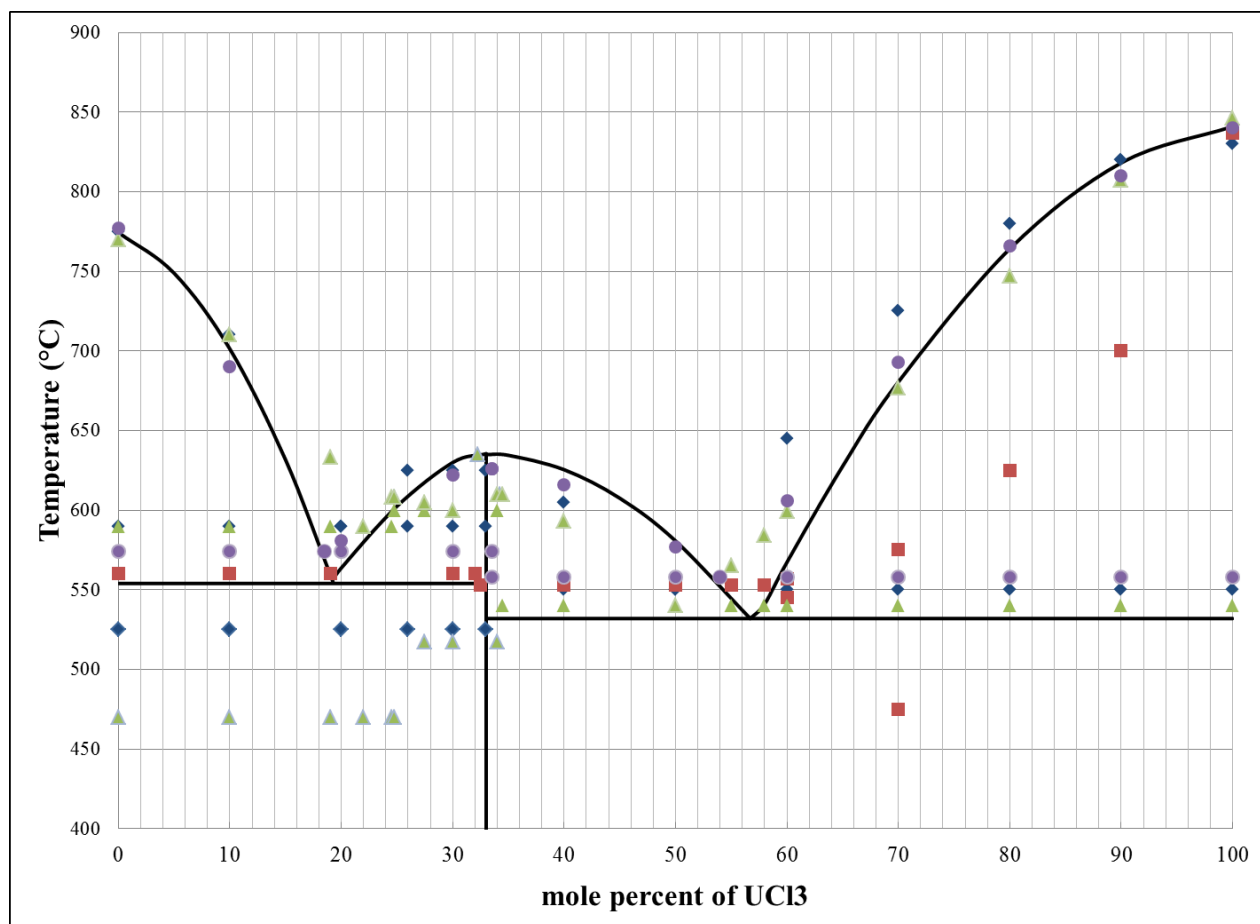


Figure 5.5 KCl-UCl₃ phase diagram drawn from DSC heating curve data with data points from previous phase diagrams by Kraus (blue diamonds)[20], Thoma (red squares)[21], and Suglobova (green triangles)[24], and Ghosh (purple circles)[16].

Reference	Eutectic 1 (UCl ₃ mol %)	Eutectic 1 melting temperature (K)	Eutectic 2 (UCl ₃ mol%)	Eutectic 2 melting temperature (K)
Kraus [20]	20	863 ± 5	50	818 ± 5
Thoma [21]	19	833	55	826
Desyatnik [22]	16	863 ± 2	50	816 ± 2
Suglobova [24]	22	863	50	813
Ghosh [16]	18.6	847	54	831
This study	19.25 ± 0.12	827 ± 3	56.70 ± 0.53	805 ± 4

Table 5.2 Experimental results and literature values for eutectic compositions and melting temperatures in the KCl-UCl₃ system

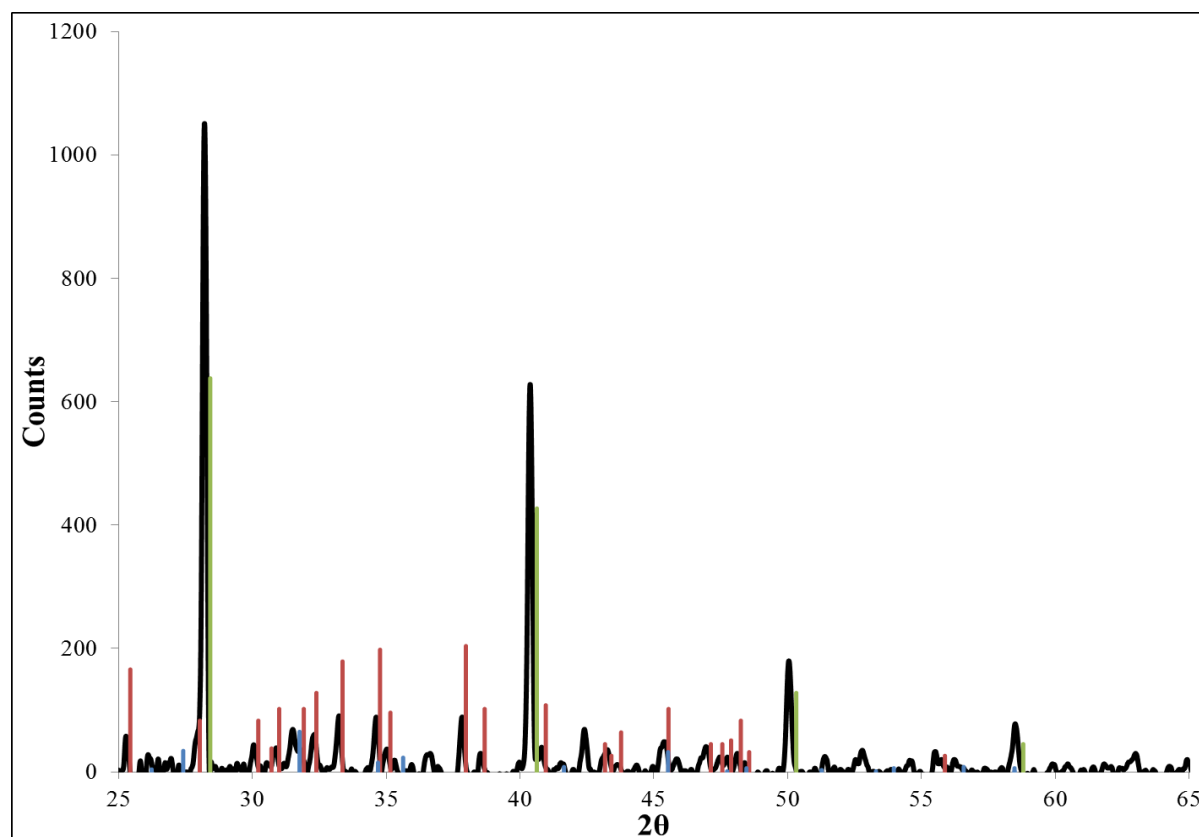


Figure 5.6 The XRD results for a sample of 10 mol % UCl₃-KCl after thermally cycling by DSC. The XRD scan is in black, the KCl pattern is green, the K₂UCl₅ pattern is red, and the K₃UCl₆ pattern is blue.

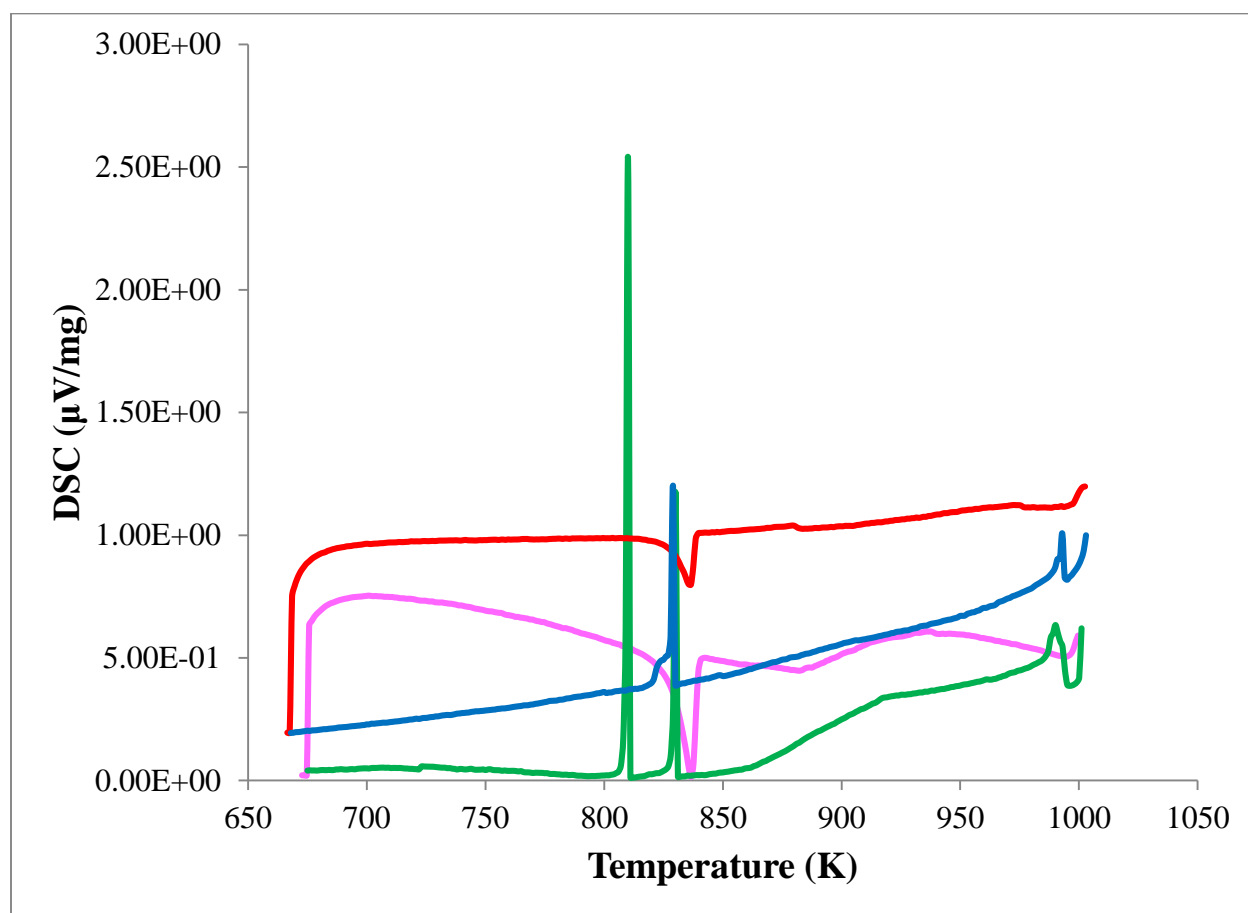


Figure 5.7 DSC curves for a sample of 10.81 ± 0.03 mol% $\text{UCl}_3\text{-KCl}$. For the rate of 5 K min^{-1} , the heating curve is shown in pink, while the cooling curve is shown in green. For the rate of 2 K min^{-1} , the heating curve is shown in red, while the cooling curve is shown in blue.

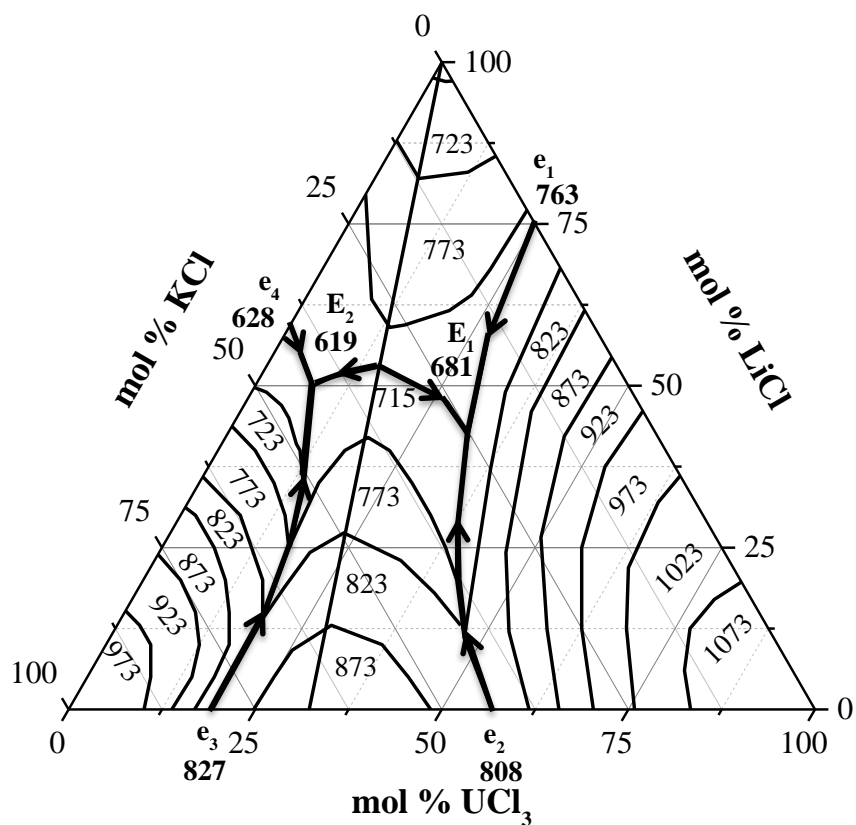


Figure 5.8 LiCl-KCl-UCl₃ liquidus projection drawn from LiCl-KCl [12], and the experimental binaries of LiCl-UCl₃, and KCl-UCl₃ from this study. Please note the liquidus lines should be smooth however, the software used to produce ternary diagrams was unable to adequately smooth these lines.

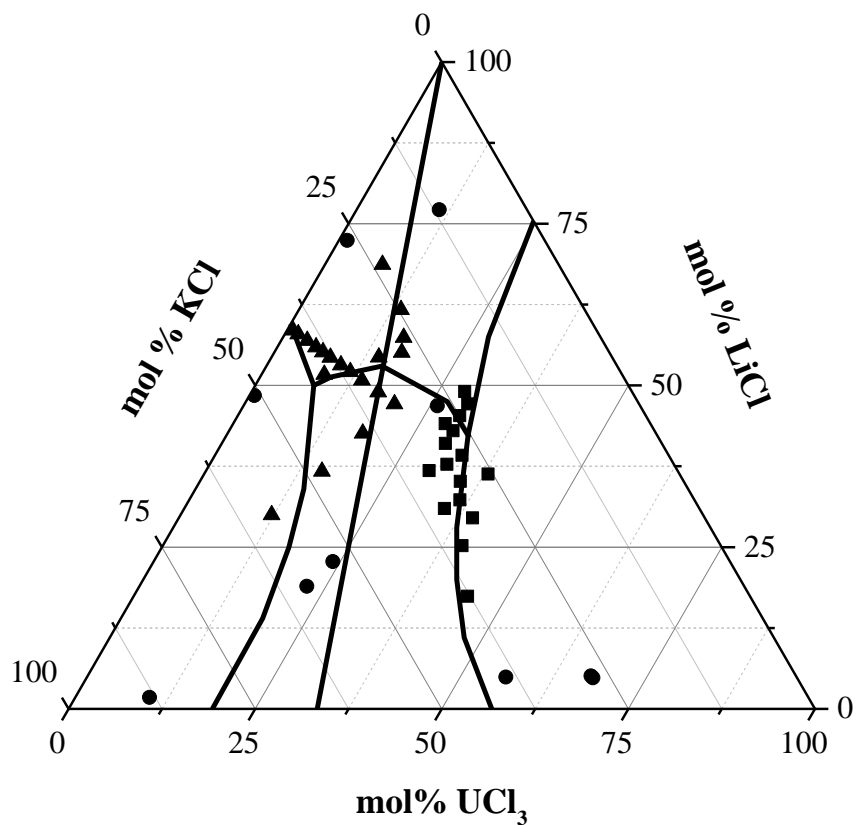


Figure 5.9 LiCl-KCl-UCl₃ liquidus projection of the isotherms with experimental data from this study (circles), Thamer [25] (squares), and Nakayoshi (triangles) [27]

Reference	Temperature K	mol % UCl ₃	mol% LiCl	mol % KCl
Eutectic 1 (E₁)				
Thamer [25]	691	30	46	24
Desyatnik [26]	668	31.5	38	30.5
Ghosh [26]	702	33.1	45.6	21.3
This study	681.1 ± 5.9	32.7	41.96	25.34
Eutectic 2 (E₂)				
Desyatnik [26]	608	12	29.5	58.5
Ghosh [16]	625	4.68 E ⁻³	57.6	42.395
This study	619.3 ± 1.1	7.85	50.02	42.13

Table 5.3 Experimental results and literature values of eutectic compositions and melting temperatures for the LiCl-KCl-UCl₃ system

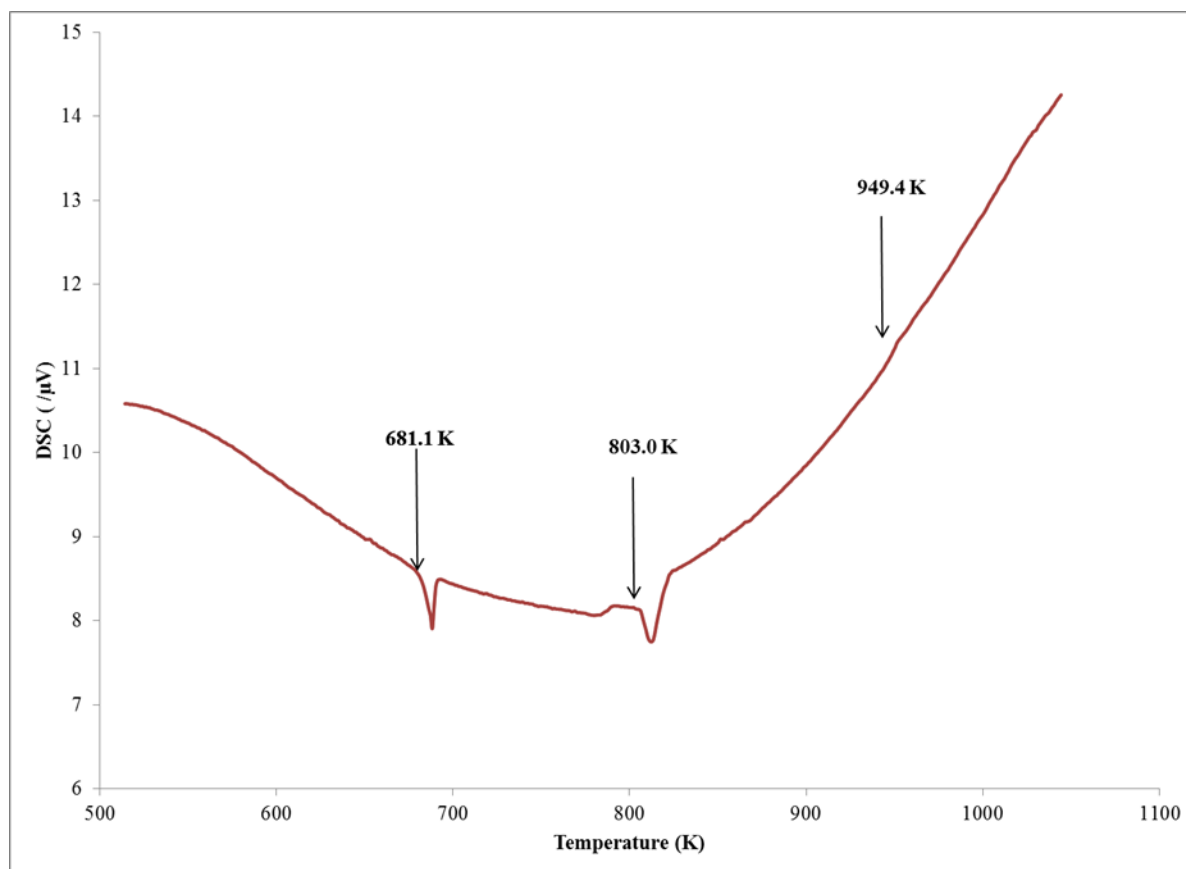


Figure 5.10 DSC heating curve for a sample of 67.85 mol% UCl_3 , 4.8 mol % LiCl , and 27.35 mol% KCl

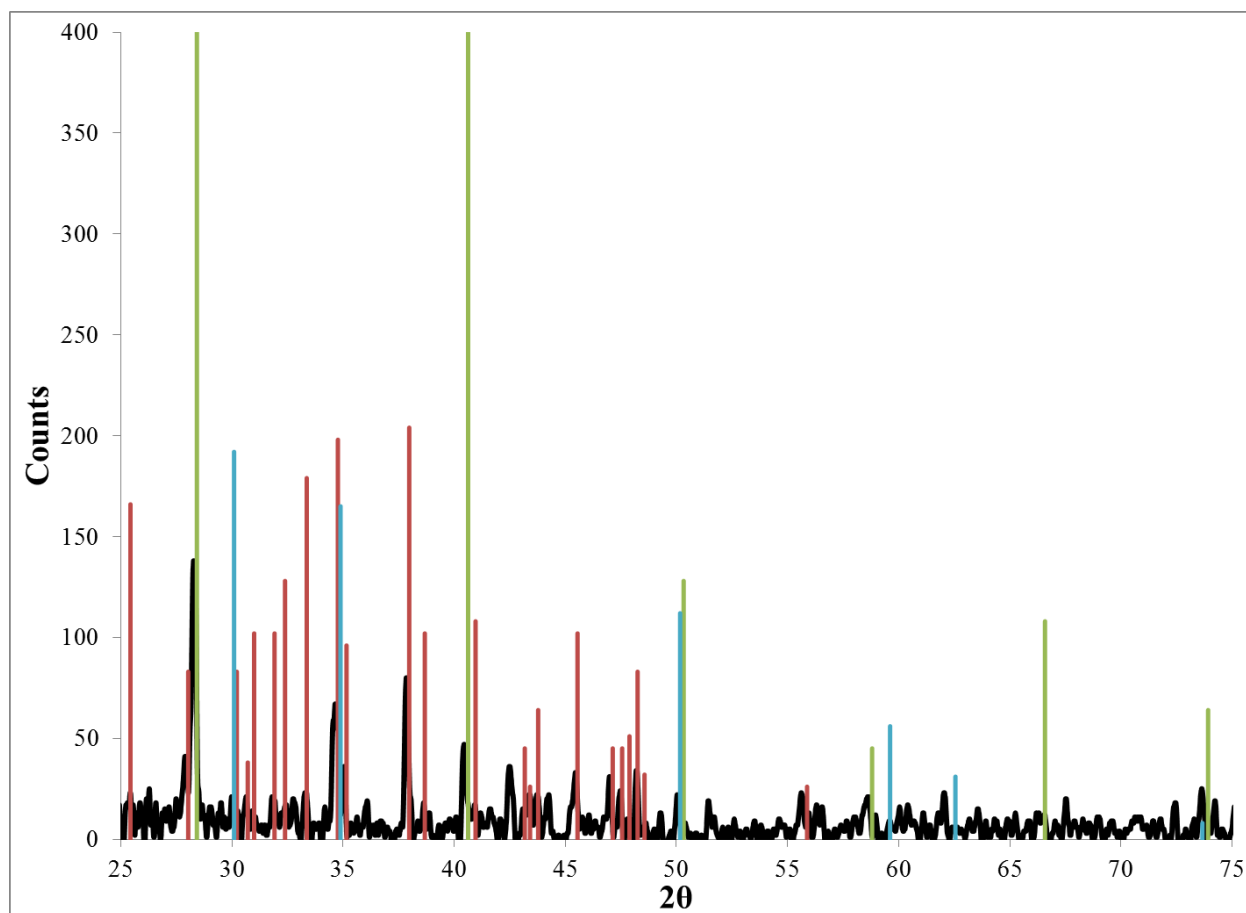


Figure 5.11 The XRD results for a sample of about 20 mol% UCl_3 , 12 mol% LiCl , and 68 mol% KCl after thermally cycling by DSC. The XRD scan is in black, the KCl pattern is green, the K_2UCl_5 pattern is red, and the LiCl is blue.

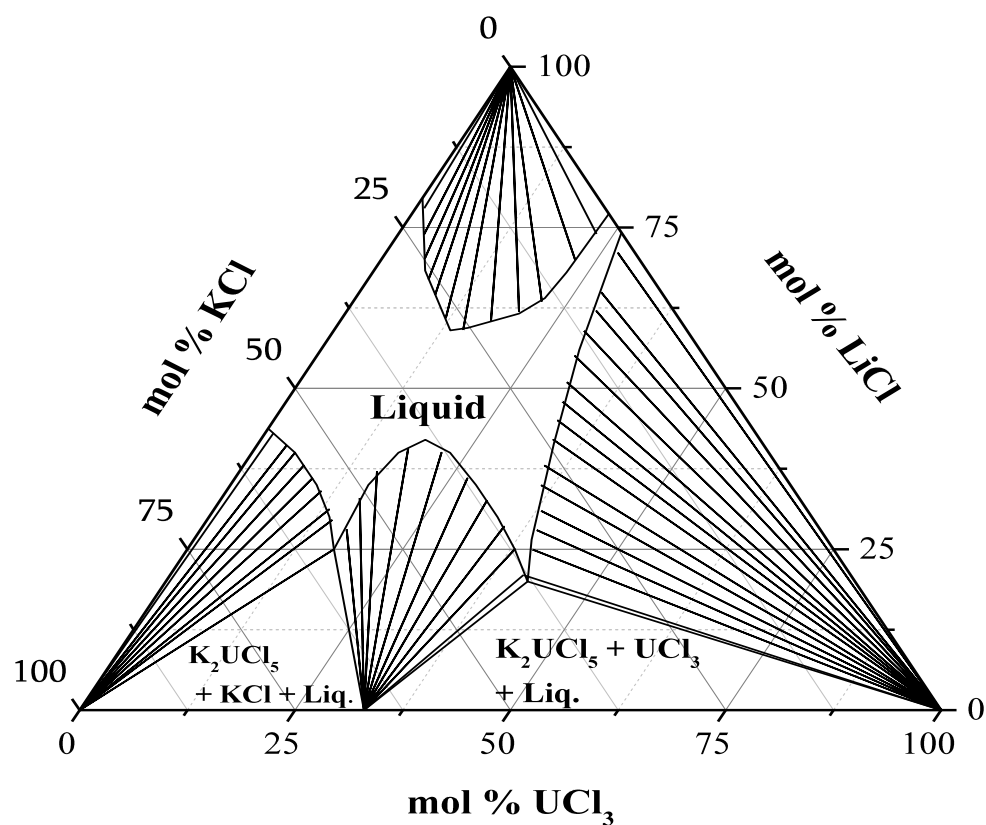


Figure 5.12 Isothermal projection of the LiCl-KCl-UCl₃ system at 773 K. Please note the liquidus lines should be smooth however, the software used to produce ternary diagrams was unable to adequately smooth these lines.

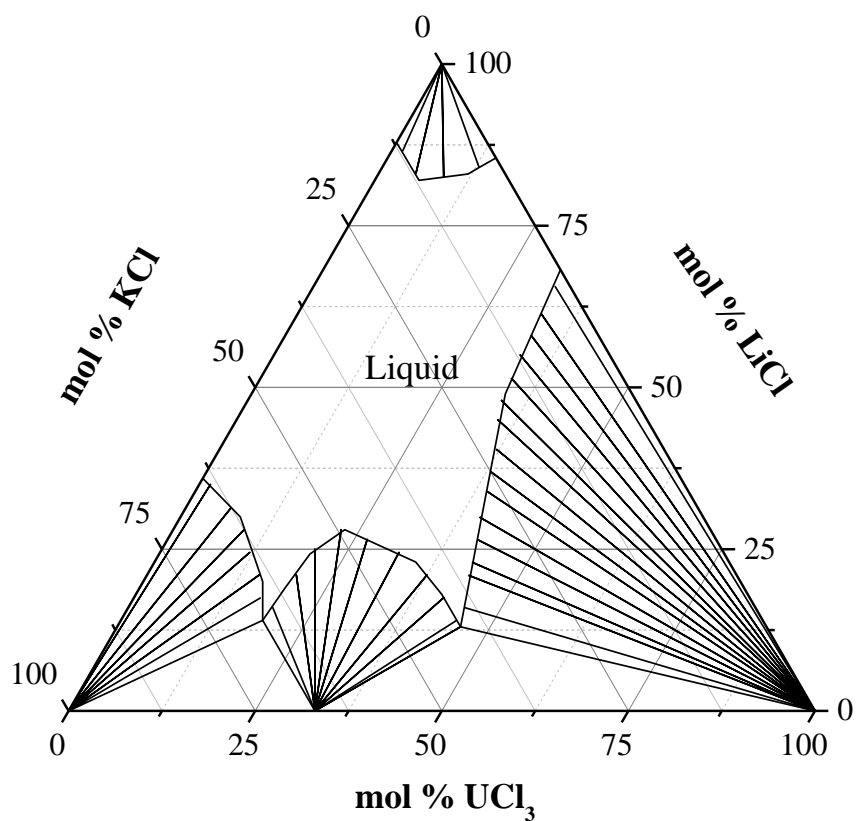


Figure 5.13 Isothermal projection of the LiCl-KCl-UCl₃ system at 823 K. Please note the liquidus lines should be smooth however, the software used to produce ternary diagrams was unable to adequately smooth these lines.

Chapter 6

Phase Equilibria Studies of the KCl-NpCl₃ System

Amber L. Hames^{1,2}, Alena Paulenova¹, James L. Willit², and Mark A. Williamson²

1. Oregon State University 1500 SW Jefferson St. Corvallis, OR 97331

2. Argonne National Laboratory 9700 S Cass Ave. Argonne, IL 60439

To be submitted to a journal

6.1. Abstract

This study experimentally evaluated the KCl-NpCl₃ binary phase diagram up to approximately 50 mol% NpCl₃. Because there is a limited concentration of neptunium in used nuclear fuel, only areas of low NpCl₃ concentrations where significant features may exist in the diagram were studied. Samples were evaluated using DSC, XRD, and ICP-MS. This system displayed a eutectic transition at 16 mol% NpCl₃, at 863 ± 3 K, a peritectic decomposition of K₂NpCl₅ at 845 K and evidence for a eutectic between K₂NpCl₅, NpCl₃ and liquid at 779 K. The K₃NpCl₆ phase congruently melted at 958 K, and the K₂NpCl₅ phase decomposed at 845 K.

6.2. Introduction

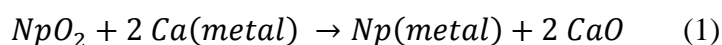
Pyroprocessing is an advanced technology for the recovery and recycle of actinides, especially transuranics, from used nuclear fuel. The main step in this technology is electrorefining, in which metallic uranium and transuranic elements (TRU) are dissolved at the anode in a molten chloride electrolyte, and electrodeposited at two different cathodes – one for U and another for a U/TRU product.[1-3] Complex phases containing transuranics could impact the performance of the electrorefining system by influencing the chemical activity of the actinides in the molten salt electrolyte and thus the redox potentials of the actinide chlorides in the molten salt solution. The thermodynamic activity of the transuranic elements will also affect the transuranic element-lanthanide element separation factors thus, studies performed on the behavior of transuranics are essential for predictive modeling and interpretation of the results of electrorefining experiments. Limited experimental thermodynamic studies have been performed regarding the behavior of the transuranic elements in the LiCl-KCl electrolyte system. While the phase equilibria of uranium and plutonium chlorides in LiCl and KCl have been previously studied [4-16], no such literature exists for NpCl₃ in LiCl or KCl. Unlike uranium and plutonium chlorides the thermodynamic properties of neptunium chlorides have not been extensively studied, and most of the data is extrapolated from thorium, uranium, and plutonium compounds. To predict the behavior of the NpCl₃-LiCl phase equilibria, it is adequate to assume that the system is similar to the UCl₃-LiCl and PuCl₃-LiCl systems, which only contain simple eutectic compositions of similar actinide trichloride concentrations (25 mol% UCl₃ and 28 mol% PuCl₃), and eutectic temperatures (763 K for UCl₃ and 734 for PuCl₃)[4, 15, 17]. The phase equilibria for the NpCl₃-KCl system cannot be predicted from the UCl₃-KCl and PuCl₃-KCl systems because these systems display varying

eutectic and peritectic features, and congruent and incongruent melting compounds [9-12, 15, 17]. The discrepancies in the $\text{UCl}_3\text{-KCl}$ system and limited experimentally determined information for $\text{PuCl}_3\text{-KCl}$ system presented the need for experimental analysis of NpCl_3 in KCl . The goal of this work was to determine the phase equilibria of the $\text{NpCl}_3\text{-KCl}$ system.

6.3. Experimental

6.3.1. NpCl_3 Synthesis

Neptunium trichloride was synthesized in an argon atmosphere glovebox. NpO_2 was chemically reduced to Np metal in a CaCl_2 melt with Ca metal based on the following reaction:



This process of direct chemical oxide reduction was first implemented for PuO_2 reduction. [18-21] In addition, it was recently used to reduce NpO_2 to Np metal. [22] Before the reduction, the neptunium nitrate was calcined in a Pt crucible at 973 K to give a neptunium oxide product. The NpO_2 was further calcined in a MgO crucible at 973 K. The CaCl_2 was dried in a MgO crucible at 823K to eliminate waters of hydration. For the reduction, a small portion of the CaCl_2 was loaded into the MgO crucible, excess calcium metal was then added to ensure the complete reduction of NpO_2 . The NpO_2 was placed directly on top of the calcium metal. The crucible was then filled with enough CaCl_2 to allow for the resulting CaO to be soluble (approximately 20 mol% CaO at 1130K). The crucible was heated in a small jeweler's furnace. When the melt reached 1130 K, a Ta stirrer was inserted to allow for constant contact of the NpO_2 and Ca metal. The system was stirred for two hours at 1130 K to allow for the chemical reduction of the NpO_2 . The stirrer was then removed, and the system was continuously heated for another three hours to allow for the Np metal to coalesce. The system was cooled overnight.

The recovered Np metal and 99.99% NH_4Cl (Sigma Aldrich) were reacted in a method that has been previously used to synthesize UCl_3 . [17] The reactants were loaded into a reaction vessel consisting of a quartz tube closed at one end that was placed in a furnace with a thermocouple situated next to the quartz tube near the reaction zone. The open end of the quartz tube was fastened to a large Pyrex tube. The Pyrex tube was connected to a vacuum via a hose to trap any vapors produced during the reaction, allowing for gas evolution without over

pressurizing the system. A Viton O-ring created the seal, which is designed to leak in the case of over-pressurization, between the quartz tube and the Pyrex top. The Np metal and excess ammonium chloride were loaded into the vessel in a ratio of about 6:1 $\text{NH}_4\text{Cl}:\text{Np}$. The vessel was evacuated and heated to 573 K for 30 hours. The resulting gray product was then heated under vacuum at 700 K for 10 hours. The gray product decomposed leaving an apple green product, which could be a mixture of NpCl_3 and NpCl_4 . Zinc metal and the neptunium chloride were then loaded into the quartz reactor and heated under a vacuum at 923 K for 12 hours to allow the Zn metal to reduce any NpCl_4 to NpCl_3 . At this temperature, the resulting ZnCl_2 , and residual Zn sublimed away from the final product. The final product of NpCl_3 was analyzed by differential scanning calorimetry (DSC) and X-ray diffraction (XRD).

6.3.2. DSC

Several different mixtures of high purity KCl and NpCl_3 were ground together with a mortar and pestle in an argon atmosphere glovebox. Samples of about 10 mg were loaded into gold cells, and hermetically sealed using a cell press. The Netzsch STA 449 C Jupiter was used for thermal analysis. Simultaneous thermal analysis (STA) combines the capabilities of differential thermal analysis (DTA), DSC and thermogravimetric analysis (TGA). An empty reference crucible and the sample crucible were situated on a platinum sample carrier of the type S thermocouple. The samples were initially thermally cycled at a rate of 20 K min^{-1} to initiate melting, and ensure homogenization. The samples were then held with a 48 hour anneal at 753 K to allow the phases to equilibrate. The following thermal cycles were run at a rate of 5 K min^{-1} , which allowed for the identification of the transition temperatures of the material. Heating curve data was used for transition temperatures determination, as the cooling curve data displayed a large degree of supercooling. The onset temperatures of the transitions were analyzed using the Netzsch Proteus Thermal Analysis software.

6.3.3. XRD

After thermal analysis, samples were analyzed by XRD to determine the phases formed during thermal cycling. Upon completion of the anneal and thermal analysis cycle, the sealed cells were cut open inside of the argon glove box, and the sample was loaded onto a single well glass slide coated with two layers of double sided tape. A Kapton film was placed onto the slide

to envelop the slide and sample. The finished slide was removed from the glove box, and the sample was analyzed on the Bruker D5000 X-ray powder diffraction system.

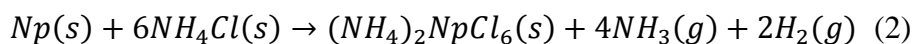
6.3.4. ICP-MS

Inductively coupled plasma mass spectrometry (ICP-MS) was used to determine ratio of Np:K in the samples. Samples of various compositions were removed from the glove box, and dissolved in nitric acid prior to ICP-MS analysis. The samples were analyzed with the Perkin Elmer/Sciex ELAN DRC II ICP-MS to determine the Np: K ratios. Sample compositions were reported to within ± 3 mol% NpCl₃.

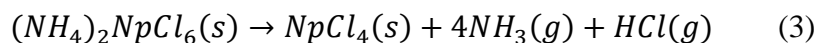
6.4. Results and Discussion

6.4.1. Neptunium Chloride Synthesis

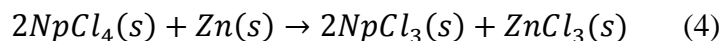
The neptunium metal had adhered to the Ta stir rod after the NpO₂ reduction experiment. A section of the metal removed from the rod is pictured in table 6.1. The Np metal and NH₄Cl were heated to 573 K for 30 hours to allow for the following reaction to occur:



At this point, a gray product, pictured in table 6.1, formed which was believed to be (NH₄)₂NpCl₆. This product was believed to decompose at 700 K by the following reaction:



Based on the XRD and DSC results for this product, it was believed that the (NH₄)₂NpCl₆ decomposed to a mixture of NpCl₄ and NpCl₃. This product was then reduced with Zn at 923 K based on the following reaction:



The final NpCl₃ product is shown in table 6.1. The NpCl₃ was analyzed by XRD, figure 6.1, and showed very good agreement with the NpCl₃ pattern. The product was also analyzed by DSC, shown in figure 6.2. The sample melted at 1072.8 K, which agrees with the known melting point of 1073 K. [105] The DSC did not show any other transitions over the temperature range studied, which indicates no contamination in the final NpCl₃ product.

6.4.2 Phase Equilibria Results

Nine samples of varying compositions of KCl-NpCl₃ with compositions below 50 mol% NpCl₃ were thermally cycled on the DSC. The phase diagram drawn from the DSC heating curve data points is given in figure 6.3. Our phase diagram is similar to the phase diagram found for the KCl-PuCl₃ system developed by Benz *et al.*[15] in that there are two eutectics, a peritectic, a congruently melting compound of K₃NpCl₆, and an incongruently melting compound of K₂NpCl₅.

We found the first eutectic, e₁, to occur at 16 ± 3.4 mol% NpCl₃ melting at 863 ± 3 K. We expect the second eutectic to occur near 56 mol %, as both the UCl₃ and PuCl₃ systems displayed a second eutectic, e₂, near 56 mol % AnCl₃ [15,17]. We consistently saw the second eutectic transition occur at 778 ± 1 K.

The K₃NpCl₆ phase was found to melt at 958 K, and the K₂NpCl₅ phase was found to decompose at 845 K. Figure 6.4 shows the XRD pattern of the sample consisting of 12.4 mol% NpCl₃. The XRD clearly displays the K₃NpCl₆ and KCl phases, as well as K₂NpCl₅. As shown in figure 6.5, this sample only displayed the eutectic transition at 858 K and the liquidus transition at 984 K.

Figure 6.6 displays the XRD pattern for the sample consisting of 31.0 mol % NpCl₃. This sample exhibits the K₃NpCl₆, K₂NpCl₅ and KCl phases. As seen in figure 6.7, this sample displayed a eutectic transition at 777 K, a peritectic transition at 846 K and a melting transition at 931 K.

According to the phase diagram in figure 6.3, the sample at 12.4 mol% NpCl₃ should not contain K₂NpCl₅, and the sample at 31 mol% should not contain KCl. When the samples were first thermally cycled without the long anneal, transitions consistent with K₂NpCl₅ were observed in samples consisting of less than 25 mol% NpCl₃. After holding the sample for a long anneal, the K₃NpCl₆ phase had time to nucleate, overcome sluggish nucleation kinetics, and the transitions associated with K₂NpCl₅ disappeared in the DSC curve. After the samples were cooled to about 500K, the samples were quenched to room temperature. It appears that in quenching these samples, the sluggish nucleation kinetics of the K₃NpCl₆ phase resulted in formation of K₂NpCl₅. Similarly, the behavior of the sample with a starting composition of 31 mol% contained KCl due to the slow nucleation rate for K₃NpCl₆.

The experimentally determined phase diagram for the KCl-NpCl₃ system displays behavior similar to the KCl-PuCl₃ [15] system rather than the KCl-UCl₃ system [17]. This behavior is likely due to the actinide contraction. For the actinides, especially the An³⁺, the radius decreases due to the diminished shielding of the nucleus, which is a result of the inclusion of the 5*f* electrons. This causes a contraction of the outer electron shell, which causes a larger cationic charge density and allows for more complex formation. [24] Thus, the plutonium and neptunium systems form K₂AnCl₅ and K₃AnCl₆, while the uranium system only forms K₂AnCl₅.

6.5. Conclusion

This binary phase diagram developed from experimental data is the only phase diagram ever established for the KCl-NpCl₃ system. DSC measurements using heating data to avoid supercooling, XRD analysis, and sample analysis by ICP-MS were employed for the evaluation of this system. NpCl₃ was synthesized from neptunium nitrate by calcining the neptunium nitrate to neptunium oxide, reducing neptunium oxide with calcium to metallic neptunium, and reacting this metal with ammonium chloride to produce the NpCl₄. Finally, the NpCl₄ was reduced to NpCl₃ with Zn, and the product was characterized with XRD and DSC. Only compositions below 50 mol % NpCl₃ were studied, because this region is of interest for electrorefining. A eutectic transition was seen at 16 mol % NpCl₃ at 863 K. The congruently melting phase K₃NpCl₆ with melting at 958 K, and incongruently melting phase of K₂NpCl₅ melting at 845 K were identified, and characterized by XRD.

6.6. Acknowledgements

The submitted manuscript has been created by U Chicago Argonne, LLC, Operator of Argonne National Laboratory (“Argonne”). Argonne, a U.S. Department of Energy Office of Science laboratory, is operated under Contract No. DE-AC02-06CH11357. The U.S. Government retains for itself, and others acting on its behalf, a paid-up nonexclusive, irrevocable worldwide license in said article to reproduce, prepare derivative works, distribute copies to the public, and perform publicly and display publicly, by or on behalf of the Government. Argonne National Laboratory’s work was supported by the U.S. Department of Energy, Office of Nuclear Energy, under contract DE-AC02-06CH11357.

6.6. References

1. Williamson, M.A. and J.L. Willit, *Pyroprocessing Flowsheets for Recycling Used Nuclear Fuel*. Nuclear Engineering and Technology, 2011: p. Medium: X; Size: 329-334.
2. Laidler, J.J., et al., *Development of pyroprocessing technology*. Progress in Nuclear Energy, 1997. **31**(1): p. 131-140.
3. McPheeters, C.C., R.D. Pierce, and T.P. Mulcahey, *Application of the pyrochemical process to recycle of actinides from LWR spent fuel*. Progress in Nuclear Energy, 1997. **31**(1): p. 175-186.
4. C.J. Barton, A.B.W., W.R. Grimes, *Phase Diagrams of Nuclear Reactor Materials*, in U.S.A.E.C., Report No. ORNL-2548 Contract No. W-7405. 1959, Oak Ridge National Laboratory: Oak Ridge, Tennessee.
5. V.N. Desyatnik, B.V.D., *Thermographic Study of the Ternary Systems Formed by Lithium Chlorides, Sodium Chloride, Potassium Chloride, Uranium Trichlorides, And Uranium Tetrachloride*. Zhurnal Prikladnoi Khimii 1975. **48**(4): p. 885-887.
6. Desyatnik V.N. , D.V.B., Raspopin S.P. , *Interaction of Uranium Trichloride with Alkali Metal Chlorides*. Russian Journal of Physical Chemistry, 1973. **47**(10): p. 1538-1539.
7. Desyatnik, V.N., et al., *Fusibility diagrams of systems involving lithium chloride, uranium trichloride, and uranium tetrachloride*. Soviet Atomic Energy, 1972. **32**(6): p. 563-564.
8. F. D. Sutherland, A.L.Hames , R.J. Blaskovitz, J.L. Willit, M.A. Williamson. *LiCl-KCl-UCl₃ Phase Diagram Studies*. in *International Pyroprocessing Research Conference 2012*. 2012.
9. Kraus, C.A., *Phase Diagram of Some Complex Salts of Uranium with Halides of the Alkali and Alkaline-Earth Metals*, in *Manhattan Project Report- 'No. 251*. July 13, 1943.
10. R.E. Thoma, H.I., H. A. Friedman, G. D. Brunton, G. M. Hebert, T. N. McVay, *Reactor Chemistry Division Annual Progress Report ORNL- 3789*, W.R. Grimes, Editor. 1965.
11. Chirkst, I.G.S.a.D.E., *Phase Diagrams of Uranium Trichloride- Alkali Metal Chloride Systems*. Koordinatsionnaya Khimiya, 1981. **7**(1): p. 97-102.
12. Ghosh, S., et al., *Experimental investigations and thermodynamic modelling of KCl-LiCl-UCl₃ system*. Calphad, 2014. **45**: p. 11-26.
13. B.J., T., *Freezing Points of Some Ternary Mixtures Derived from 55 mol% UCl₃-45 mol% KCl*, in *Technical Report, LA-3579-MS*, L.A.N. Laboratory, Editor. 1966.
14. Nakayoshi, A., et al., *Investigation of a LiCl-KCl-UCl₃ system using a combination of X-ray diffraction and differential thermal analyses*. Journal of Nuclear Materials, 2013. **441**(1-3): p. 468-472.

15. Benz, R., M. Kahn, and J.A. Leary, *Phase Equilibria of the Binary System PuCl₃–KCl*. The Journal of Physical Chemistry, 1959. **63**(11): p. 1983-1984.
16. Bjorklund, C.W., et al., *Phase Equilibria in the Binary Systems PuCl₂–NaCl and PuCl₂–LiCl*. The Journal of Physical Chemistry, 1959. **63**(10): p. 1774-1777.
17. A.L. Hames, A. Paulenova, J.L. Willit, M.A. Williamson, *Phase Equilibria Studies of the LiCl-KCl-UCl₃ System*. 2017: In Production.
18. COOPS, M.S., J.B. KNIGHTON, and L.J. MULLINS, *Pyrochemical processing of plutonium*. 1983, ACS Publications.
19. Mullins, L., D. Christensen, and B. Babcock, *Fused salt processing of impure plutonium dioxide to high-purity plutonium metal*.
20. Perry, G.S. and L.G. Macdonald, *Role of CaCl₂ in the reduction of PuO₂*. Journal of Nuclear Materials, 1985. **130**: p. 234-241.
21. Moser, W.S. and J.D. Navratil, *Review of major plutonium pyrochemical technology*. Journal of the Less Common Metals, 1984. **100**: p. 171-187.
22. Squires, L.N. and P. Lessing, *Direct chemical reduction of neptunium oxide to neptunium metal using calcium and calcium chloride*. Journal of Nuclear Materials, 2016. **471**: p. 65-68.
23. Fried, S., *METHODS OF MAKING-NEPTUNIUM*. 1951, Google Patents.
24. Choppin, G.R., J.O. Liljenzin, and J. Rydberg, *Radiochemistry and Nuclear Chemistry*. 2002: Butterworth-Heinemann.

6.8. Figures

Product	Temperature (K)	Hold Time (h)	Notes	Picture
Np	1130	2	Stirring	
$(\text{NH}_4)_2\text{NpCl}_6$	573	30		
NpCl_4	700	10	Vacuum	
NpCl_3	923	12	Vacuum	

Table 6.1 Experimental parameters and product of each step of the NpCl_3 synthesis

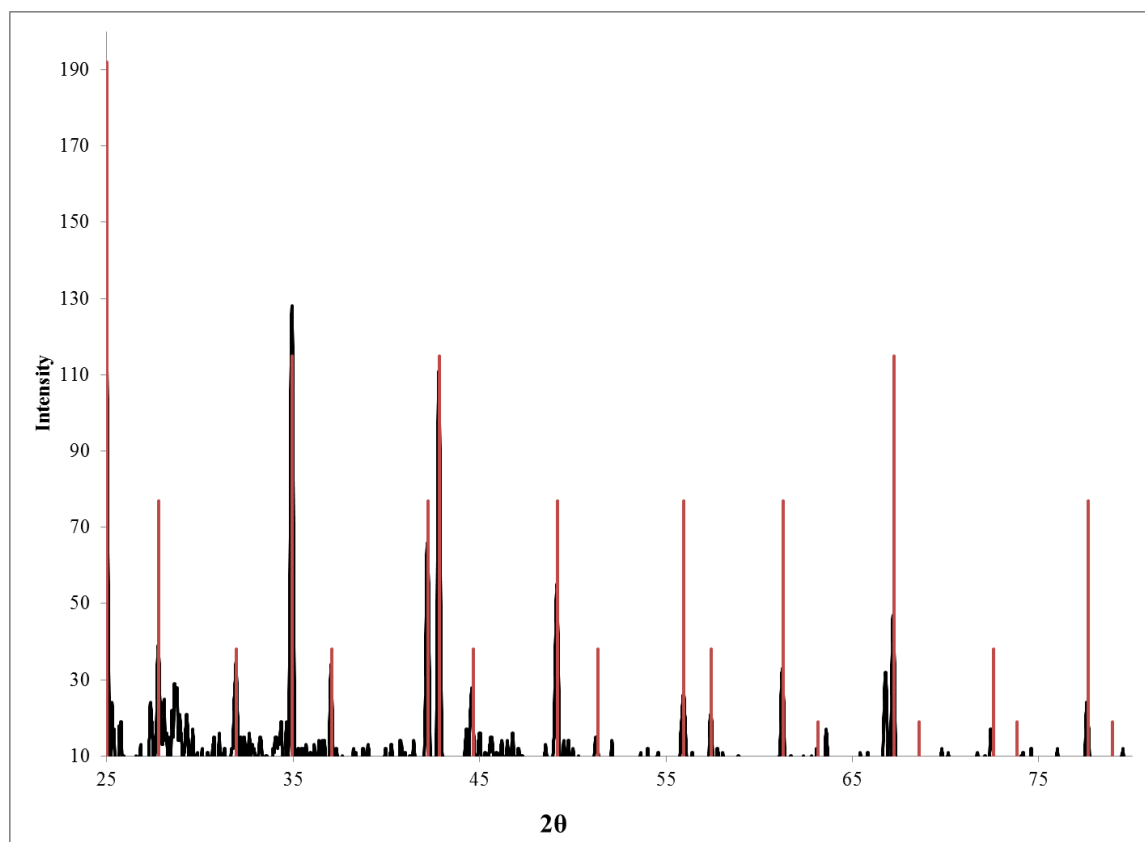


Figure 6.1 The XRD scan for NpCl_3 product (black) with NpCl_3 pattern (red).

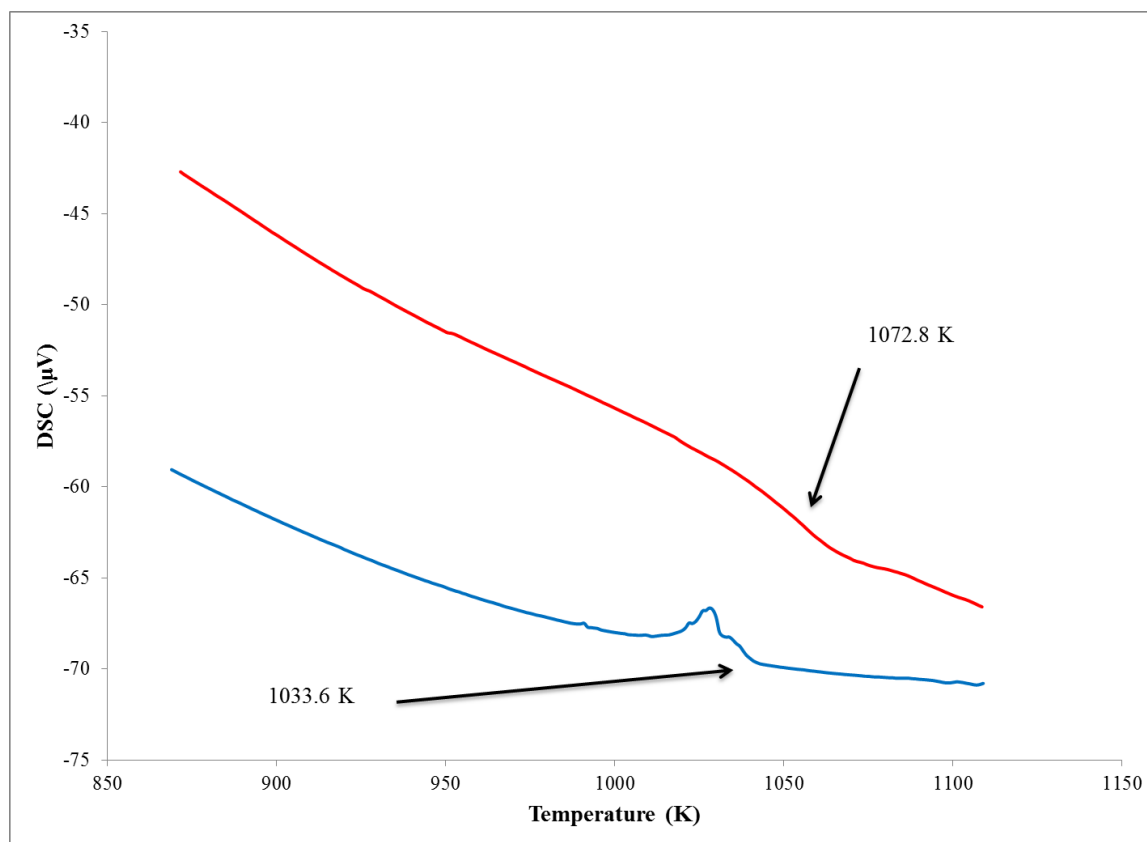


Figure 6.2 DSC of heating (red) and cooling (blue) of the NpCl_3 product.

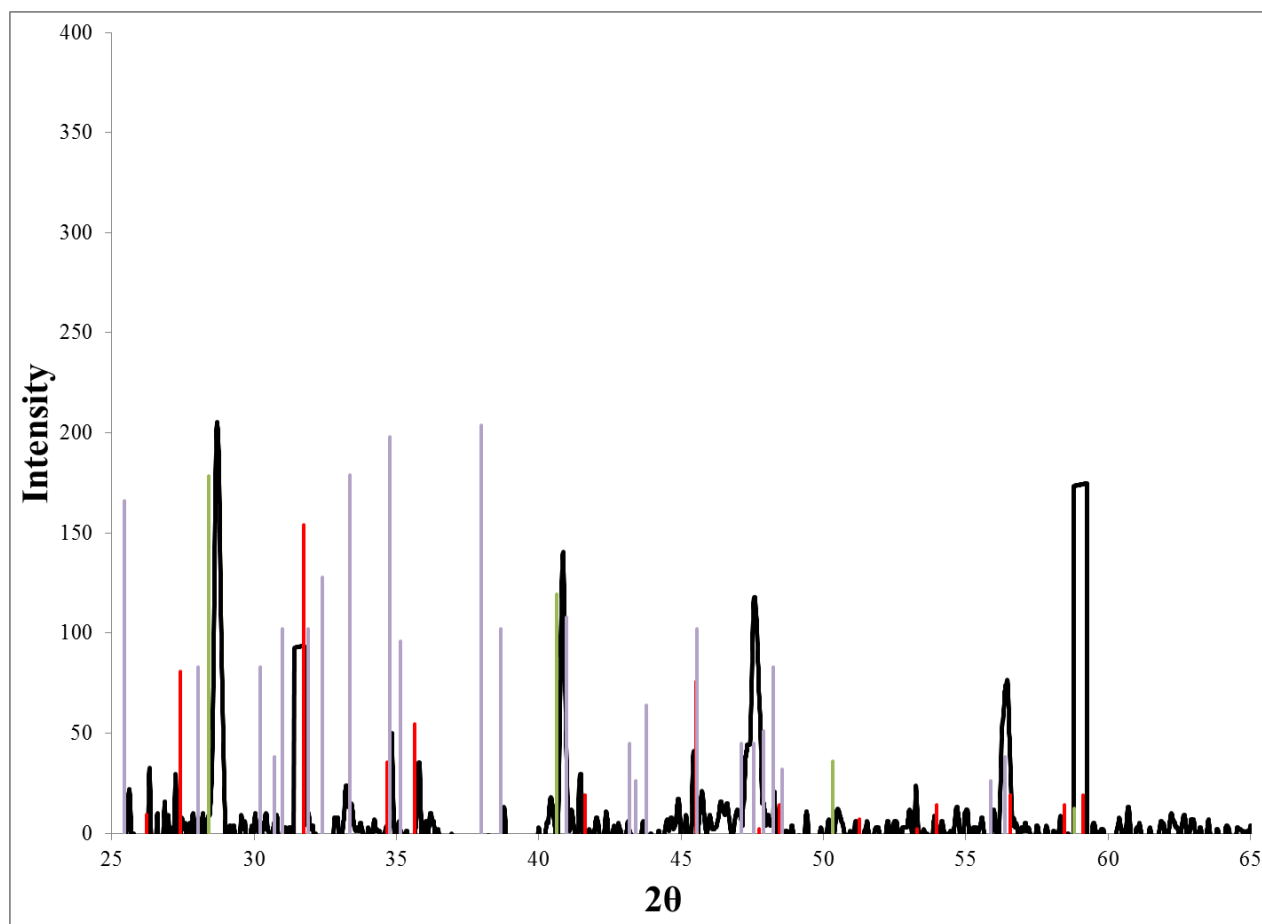


Figure 6.4 The XRD scan for a sample containing 12.4 mol% NpCl_3 after thermally cycling by DSC. The sample scan is in black, KCl is displayed in green, K_3NpCl_6 is displayed in red, and K_2NpCl_5 is displayed in purple. Please note, the K_3NpCl_6 peaks were scaled using a constant scaling factor, based on the ratio of the largest peak in the calculated pattern to the actual peaks in the sample.

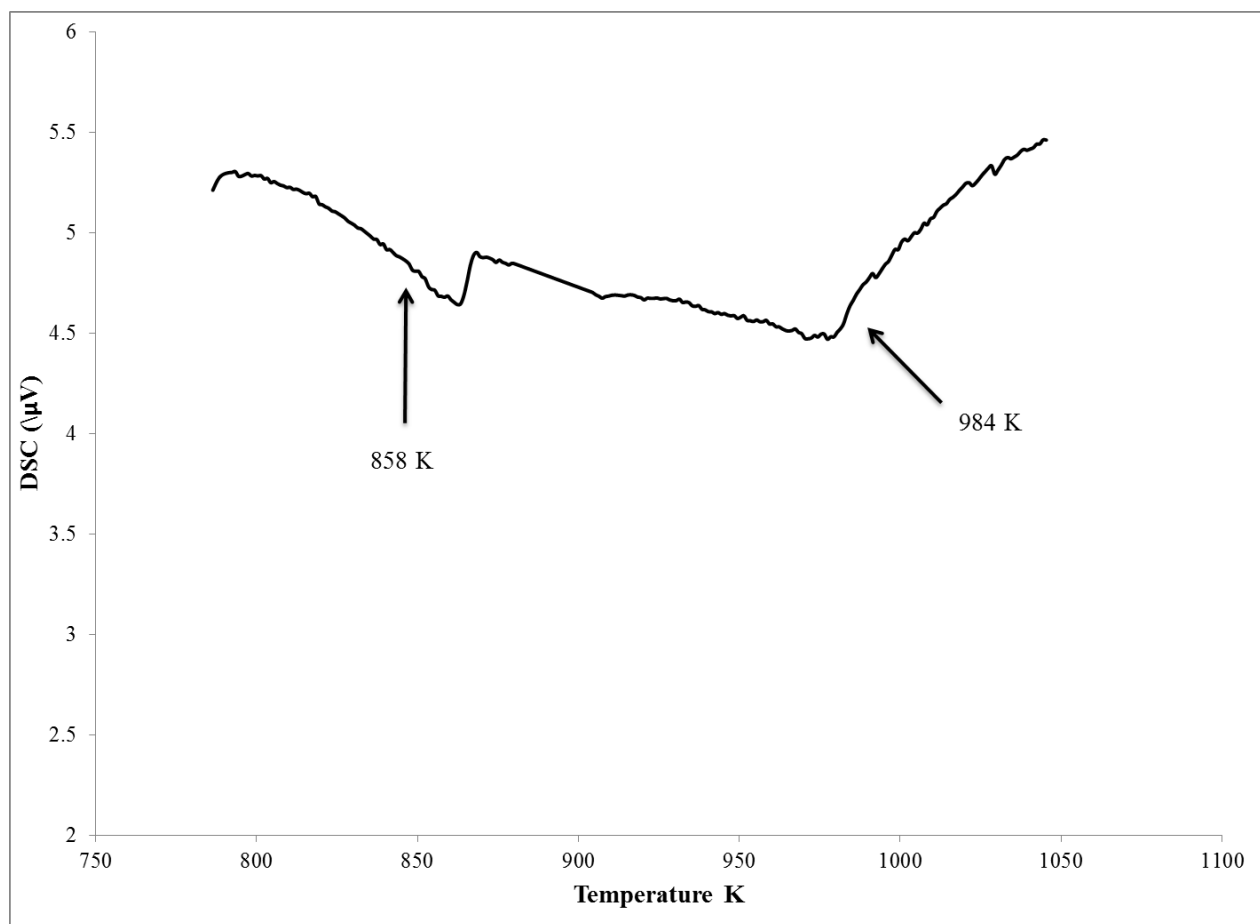


Figure 6.5 DSC heating curve for a sample containing 12.4 mol% NpCl_3 after annealing for 48 hours.

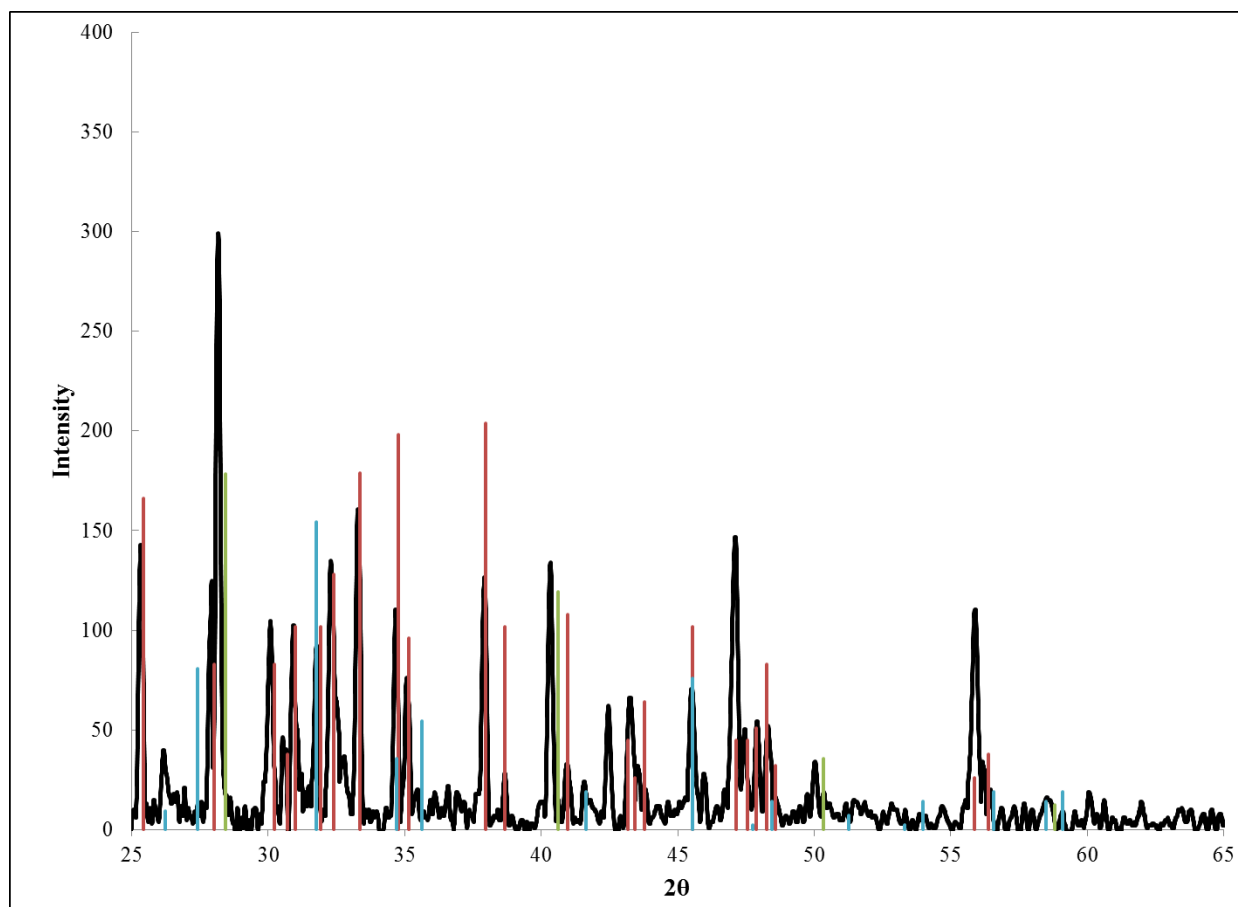


Figure 6.6 The XRD results for a sample of 31.0 mol % NpCl_3 after thermally cycling by DSC. The XRD scan is in black, the KCl pattern is green, the K_2NpCl_5 pattern is red, and K_3NpCl_6 pattern is blue. Please note, the K_3NpCl_6 peaks were scaled using a constant scaling factor, based on the ratio of the largest peak in the calculated pattern to the actual peaks in the sample.

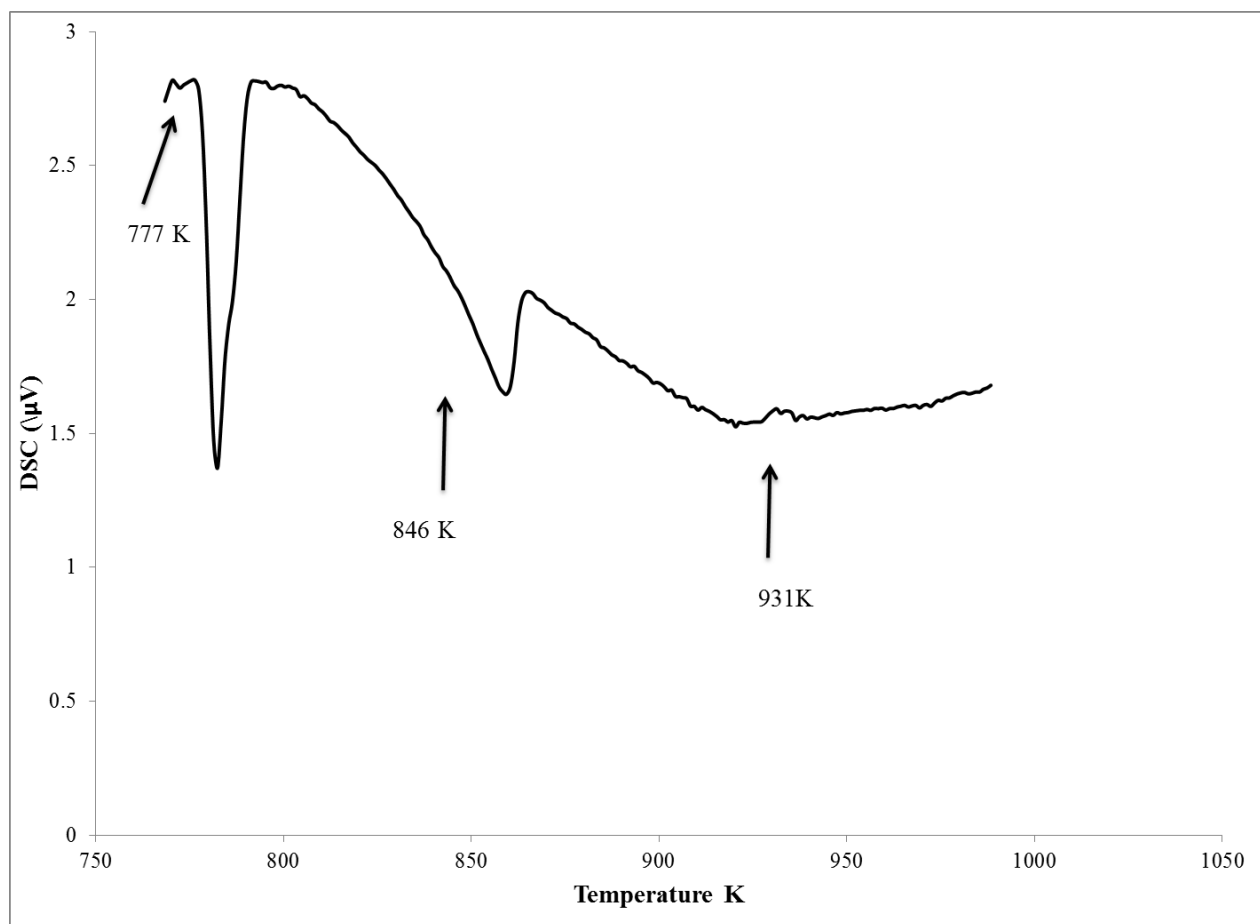


Figure 6.7 DSC heating curve for a sample containing 31 mol% NpCl_3 after annealing for 48 hours.

7. Conclusion

The work presented in this dissertation documents the investigation of two chemical systems relevant to pyroprocessing used nuclear fuel. The first investigation determined that the use of molybdate melts at high temperatures is feasible for the removal of fission products from a uranium product for a modified open fuel cycle. The composition of the uranium product based on the $\text{MoO}_3:\text{Na}_2\text{MoO}_4$ ratio in the melt was investigated. It was determined that melt compositions containing more MoO_3 than UO_2 yield uranium molybdates as a major species, such as UMo_2O_8 , while melts containing less MoO_3 lead to the formation of UO_2 precipitate as a major species.

The conditions to achieve the purest uranium oxide product were also investigated and determined to be:

1. A melt consisting of 20 wt% MoO_3 - 50 wt% Na_2MoO_4 -30 wt% UO_2
2. Heating the melt to 1313 K and performing the physical separation of the UO_2 from the mother liquor.
3. Washing the uranium product once with Na_2MoO_4 .

The fission products investigated in the simulated fuel displayed adequate partitioning from the uranium precipitate product. Particularly good separations ($D=100$ - 55000) were seen in fission products such as Cs, Sr, Ru and Rh. Zirconium and the lanthanides had lower distribution ratios ($D=5$ -100); however, distribution ratios greater than 10 are adequate for purification and recycle of the UO_2 .

The second investigation was the study of phase equilibria of uranium and neptunium trichloride in the LiCl-KCl molten salt electrolyte used in electrorefining used nuclear fuel. The fundamental phase behavior of the UCl_3 and NpCl_3 in the LiCl-KCl system is important for predicting the behavior of the electrolyte at the electrode-electrolyte interface during electrorefining used nuclear fuel. The LiCl-UCl_3 , KCl-UCl_3 , LiCl-KCl-UCl_3 and KCl-NpCl_3 systems were evaluated using DSC measurements with heating data to avoid supercooling, which was observed in the cooling data, XRD analysis, and sample analysis by ICP-MS or ICP-OES. The LiCl-UCl_3 system displayed a eutectic transition at 24.6 mol % UCl_3 and 75.4 mol% LiCl with melting at 763 ± 2 K. The resulting phase diagram was consistent with the literature. The KCl-UCl_3 system displayed two eutectic transitions. The first eutectic, e_1 , was seen at 19.25

mol% UCl_3 and 80.75 mol % KCl with melting at 827 ± 3 K. The second eutectic, e2, was seen at 56.70 mol% UCl_3 and 43.3 mol % KCl with melting at 805 ± 4 K. The K_2UCl_5 melting transition was observed at 635 K in DSC and XRD. No evidence of a K_3UCl_6 phase was observed. The LiCl-KCl-UCl_3 system was drawn from the LiCl-UCl_3 and KCl-UCl_3 experimentally determined binary systems, and the LiCl-KCl binary system from the literature. This system displayed two ternary eutectics. The first eutectic, E1, was seen at 32.7 mol % UCl_3 , 41.96 mol% LiCl , and 25.34 mol % KCl with melting at 681.1 ± 5.9 K. The second eutectic, E2, was seen at 7.85 mol % UCl_3 , 50.02 mol % LiCl , and 42.13 mol % LiCl with melting at 619.3 ± 1.1 K.

The KCl-NpCl_3 binary phase diagram developed from experimental data is the only phase diagram established for the KCl-NpCl_3 system. NpCl_3 was synthesized from neptunium nitrate by calcining the neptunium nitrate to neptunium oxide, reducing neptunium oxide with calcium to metallic neptunium, and reacting this metal with ammonium chloride to produce NpCl_4 . The NpCl_4 was reduced to NpCl_3 with Zn , and the product was characterized with XRD and DSC. Only compositions below 50 mol % NpCl_3 in the phase diagram were studied, because this region is of interest for electrorefining. A eutectic transition, e1, was seen at 16 mol % NpCl_3 at 863 K. A second eutectic was identified to have a melting temperature of 778 K. The congruently melting phase K_3NpCl_6 with melting at 958 K, and incongruently melting phase of K_2NpCl_5 melting at 845 K were identified, and characterized by XRD.

These two investigations of chemical processes used for pyroprocessing used nuclear fuel helped to advance fundamental knowledge to further improve pyroprocessing. The first study provided insight into the feasibility of using molybdate melts to purify uranium from fission products in a modified open fuel cycle. The second study provided fundamental knowledge of the phase equilibria of UCl_3 and NpCl_3 in LiCl-KCl systems, which allows for improved understanding of these species in the electrorefining process.

8. Bibliography

1. Taylor, R., *Reprocessing and Recycling of Spent Nuclear Fuel*. 2015: Elsevier Science.
2. Williamson, M.A. and J.L. Willit, *Pyroprocessing Flowsheets for Recycling Used Nuclear Fuel*. Nuclear Engineering and Technology, 2011: p. Medium: X; Size: 329-334.
3. McPheeters, C.C., R.D. Pierce, and T.P. Mulcahey, *Application of the pyrochemical process to recycle of actinides from LWR spent fuel*. Progress in Nuclear Energy, 1997. **31**(1): p. 175-186.
4. Laidler, J.J., et al., *Development of pyroprocessing technology*. Progress in Nuclear Energy, 1997. **31**(1): p. 131-140.
5. Kok, K.D., *Nuclear Engineering Handbook*. 2009: CRC Press.
6. Burris, L., et al., *The Melt Refining of Irradiated Uranium: Application to EBR-II Fast Reactor Fuel. I. Introduction*. Nuclear Science and Engineering, 1959. **6**(6): p. 493-495.
7. Goff, K., et al., *Electrochemical processing of used nuclear fuel*. Nuclear engineering and technology, 2011. **43**(4): p. 335-342.
8. *Pyroprocessing Technologies Recycling Used Nuclear Fuel for a Sustainable Energy Future* A.N. Laboratory, Editor.
9. Ackerman, J.P., *Chemical basis for pyrochemical reprocessing of nuclear fuel*. Industrial & Engineering Chemistry Research, 1991. **30**(1): p. 141-145.
10. Zhang, J., *Electrochemistry of actinides and fission products in molten salts—Data review*. Journal of Nuclear Materials, 2014. **447**(1–3): p. 271-284.
11. Ustinov, O.A., L.P. Sukhanov, and S.A. Yakunin, *Reprocessing of spent oxide nuclear fuel by recrystallization in molybdate melts*. Atomic Energy, 2006. **101**(4): p. 771-774.
12. Ustinov, O.A., L.P. Sukhanov, and O.N. Pogorelko, *Reduction recrystallization of uranium oxides in molybdate melts*. Atomic Energy. **102**(5): p. 361-363.
13. Ustinov, O.A., *The physical chemistry for regenerating spent uranium and plutonium oxide fuel by recrystallization from molybdate melts*. Atomic Energy, 1997. **82**(2): p. 99-102.
14. Hames A.L., Tkac.P., Paulenova A., Williamson M.A., Willit J.L. *Investigation of U Behavior in Molybdate Melts for Alternative Pyrochemical Reprocessing of Spent Nuclear Fuel*. in American Chemical Society National Meeting. 2013. Indianapolis, Indiana.
15. Hames, A.L., et al., *Investigation of molybdate melts as an alternative method of reprocessing used nuclear fuel*. Journal of Nuclear Materials, 2017. **486**: p. 158-166.
16. Nakayoshi, A., et al., *Investigation of a LiCl–KCl–UCl₃ system using a combination of X-ray diffraction and differential thermal analyses*. Journal of Nuclear Materials, 2013. **441**(1–3): p. 468-472.
17. Zemczuzny, S. and F. Rambach, *Schmelzen der Alkalichloride*. Zeitschrift für anorganische Chemie, 1910. **65**(1): p. 403-428.

18. Richards, T.W. and W.B. Meldrum, *THE MELTING POINTS OF THE CHLORIDES OF LITHIUM, RUBIDIUM AND CAESIUM, AND THE FREEZING POINTS OF BINARY AND TERNARY MIXTURES OF THESE SALTS, INCLUDING ALSO POTASSIUM AND SODIUM CHLORIDE*. Journal of the American Chemical Society, 1917. **39**(9): p. 1816-1828.
19. Schaefer, W., Neues Jahrb. Mineral., Geol., Paleontol., Beil, 1920. **43**: p. 132.
20. Keitel, H., *Über die ternären Systeme aus Lithium-, Kalium-, Rubidiumchlorid und Kalium-,Rubidium, Cäsiumchlorid*. Neues Jahrb. Mineral., Geol., Paleontol., Beil, 1925. **52**: p. 378-423.
21. Elchardus, E. and P. Laffitte, *Etude thermique des systJmes KCl-BaCl₂ et KCl-LiCl*. Bull. Soc. Chim.(France), 1932. **51**: p. 1572-9.
22. Unzakov, G.M., DAN SSSR. . **87**: p. 791.
23. Bergman, E.K.A.A.G., Izv. SFKhA, 1954: p. 255.
24. Sangster, J. and A.D. Pelton, *Phase diagrams and thermodynamic properties of the 70 binary alkali halide systems having common ions*. Journal of physical and chemical reference data, 1987. **16**(3): p. 509-561.
25. Kaplun, A.B. and A.B. Meshalkin, *Study of phase equilibria in salt and oxide systems by the oscillation method of phase analysis*. Journal of Thermal Analysis and Calorimetry, 2008. **92**(3): p. 687-690.
26. Basin, A.S., et al., *The LiCl-KCl binary system*. Russian Journal of Inorganic Chemistry, 2008. **53**(9): p. 1509-1511.
27. Korin, E. and L. Soifer, *Thermal analysis of the system KCl-LiCl by differential scanning calorimetry*. Journal of thermal analysis, 1997. **50**(3): p. 347-354.
28. Ghosh, S., et al., *Experimental investigations and thermodynamic modelling of KCl-LiCl-UCl₃ system*. Calphad, 2014. **45**: p. 11-26.
29. C.J. Barton, A.B.W., W.R. Grimes, *Phase Diagrams of Nuclear Reactor Materials*, in U.S.A.E.C., Report No. ORNL-2548 Contract No. W-7405. 1959, Oak Ridge National Laboratory: Oak Ridge, Tennessee.
30. Desyatnik, V.N., et al., *Fusibility diagrams of systems involving lithium chloride, uranium trichloride, and uranium tetrachloride*. Soviet Atomic Energy, 1972. **32**(6): p. 563-564.
31. Kraus, C.A., *Phase Diagram of Some Complex Salts of Uranium with Halides of the Alkali and Alkaline-Earth Metals*, in Manhattan Project Report- 'No. 251. July 13, 1943.
32. Desyatnik V.N. , D.V.B., Raspopin S.P. , *Interaction of Uranium Trichloride with Alkali Metal Chlorides*. Russian Journal of Physical Chemistry, 1973. **47**(10): p. 1538-1539.
33. Chirkst, I.G.S.a.D.E., *Phase Diagrams of Uranium Trichloride- Alkali Metal Chloride Systems*. Koordinatsionnaya Khimya, 1981. **7**(1): p. 97-102.
34. B.J., T., *Freezing Points of Some Ternary Mixtures Derived from 55 mol% UCl₃-45 mol% KCl*, in Technical Report, LA-3579-MS, L.A.N. Laboratory, Editor. 1966.

35. Ustinov, O.A., et al., *The system MoO₃-UO₃*. Soviet Atomic Energy. **34**(3): p. 203-205.
36. Prokoshin A.D., U.O.A., Andrianov I.A., Chebotarev N.T., Matyushin E.A., , *The MoO₃-PuO₂ System*. Russian Journal of Inorganic Chemistry, 1976. **21**(6): p. 854-856.
37. Tul'skii G.V., U.O.A., *Behavior of Trace Impurities of Ruthenium, Cerium, and Cesium in the Crystallization of Uranium Dioxide from Molten UO₂-MoO₃-Na₂MoO₄*. Radiochemistry, 1977. **19**(3): p. 254-259.
38. Hames A.L., T.P., Williamson M.A., Willit J.L. *Investigation of Molybdate Melts fo Alternative Pyrochemical Reprocessing of Used Nuclear Fuel*. in *2012 International Pyroprocessing Research Conference*. 2012. Fontana, Wisconsin.
39. Tkac P., Hames A.L., Cruse T.A., Willit J.L. Williamson M.A. . *Alternative Pyrochemical Reprocessing of Used Nuclear Fuel Using Molybdate Melts*. in *12th Information Exchange Meeting on Actinide and Pission Product Partitioning and Transmutation 2012*. Prague, Czech Republic.
40. Fortes, A.D., *Crystal structures of spinel-type Na(2)MoO(4) and Na(2)WO(4) revisited using neutron powder diffraction*. Acta Crystallographica Section E: Crystallographic Communications, 2015. **71**(Pt 6): p. 592-596.
41. Bramnik, K.G. and H. Ehrenberg, *Study of the Na₂O—MoO₃ System. Na₆Mo₁₁O₃₆ — a New Oxide with Anatase-related Structure, and the Crystal Structures of Na₂MoO₄*. Zeitschrift für anorganische und allgemeine Chemie, 2004. **630**(8-9): p. 1336-1341.
42. Gatehouse, B.M., *Alkali metal and silver molybdates and polymolybdates some recently determined structures*. Journal of the Less Common Metals, 1974. **36**(1–2): p. 53-59.
43. Wooster, N., *The crystal structure of Molybdenum Trioxide, MoO₃*, in *Zeitschrift für Kristallographie - Crystalline Materials*. 1931. p. 504.
44. Rao M.C., R.k., Kasturi A., Shekhawt M.S., *Structural Stoichiometry and Phase Transitions of MoO₃ Thin Films for Solid State Microbatteries*. Research Journal of Recent Sciences 2012. **2**(4): p. 67-73.
45. Hoermann, F., *Beitrag zur Kenntniss der Molybdate und Wolframate. Die binären Systeme: Li₃MoO₄□MoO₃, Na₂MoO₄□MoO₃, K₃MoO₄□MoO₃, Li₂WO₄□WO₃, Na₂WO₄□WO₃, K₂WO₄□WO₃, Li₂MoO₄□Na₂MoO₄, Li₂WO₄□Na₂WO₄, Li₂MoO₄□K₂MoO₄*. Zeitschrift für anorganische und allgemeine Chemie, 1929. **177**(1): p. 145-186.
46. Yu. G. Petrosyan, V.M.Z., O. A. Ustinov, and T. M. Panfilova, Russ. J. Inorg. Chem. (Engl. Transl.), 1977. **22**(10): p. 1542-1544.
47. Gatehouse, B.M., C.E. Jenkins, and B.K. Miskin, *The crystal structure of a sodium molybdenum oxide, Na₆Mo₁₀O₃₃, containing cross-linked chains of octahedra and square pyramids*. Journal of Solid State Chemistry, 1983. **46**(3): p. 269-274.

48. Voronko, Y.K., A.A. Sobol, and V.E. Shukshin, *Raman scattering study of molten alkali-metal molybdates rich in MoO₃*. Inorganic Materials, 2014. **50**(8): p. 844-849.
49. Saraiva, G.D., et al., *Temperature-dependent Raman scattering studies on Na₂Mo₂O₇ disodium dimolybdate*. Journal of Raman Spectroscopy, 2011. **42**(5): p. 1114-1119.
50. Seleborg, M., *A Refinement of the Crystal Structure of Disodium Dimolybdate*. Acta Chemica Scandinavica, 1967. **21**: p. 499-504.
51. Goloboy, J.C., et al., *Complex Oxides as Molecular Materials: Structure and Bonding in High-Valent Early Transition Metal Compounds*, in *Polyoxometalate Molecular Science*, J.J. Borrás-Almenar, et al., Editors. 2003, Springer Netherlands: Dordrecht. p. 79-174.
52. Willis, B.T.M., *Neutron Diffraction Studies of the Actinide Oxides. I. Uranium Dioxide and Thorium Dioxide at Room Temperature*. Proceedings of the Royal Society of London. Series A. Mathematical and Physical Sciences, 1963. **274**(1356): p. 122-133.
53. Skinner, L.B., et al., *Molten uranium dioxide structure and dynamics*. Science, 2014. **346**(6212): p. 984-987.
54. Krivovichev, S.V. and P.C. Burns, *Chapter 4 - Actinide compounds containing hexavalent cations of the VI group elements (S, Se, Mo, Cr, W)*, in *Structural Chemistry of Inorganic Actinide Compounds*. 2007, Elsevier: Amsterdam. p. 95-182.
55. Krivovichev, S. and P. Burns. *γ-UMo₂O₈ as a new polymorph of uranium dimolybdate containing tetravalent uranium*. in *Doklady Physics*. 2004. Springer.
56. Dahale, N.D., et al., *Structural and thermal studies on Na₂U(MoO₄)₃ and Na₄U(MoO₄)₄*. Journal of Alloys and Compounds, 2007. **440**(1-2): p. 145-149.
57. Hames A.L., Cruse T.L., Willit J.L. Williamson M.A, Paulenova A. *A Fundamental Investigation of the Synthesis and Characterization of UCl₃ and (NH₄)₂UCl₆ for Applications of Transuranic Chloride Synthesis and Characterization*. in *International Pyroprocessing Research Conference*. 2014. Idaho Falls, Idaho.
58. Lind, C., et al., *Synthesis and Properties of the Negative Thermal Expansion Material Cubic ZrMo₂O₈*. Chemistry of Materials, 1998. **10**(9): p. 2335-2337.
59. Sczancoski, J.C., et al., *SrMoO₄ powders processed in microwave-hydrothermal: Synthesis, characterization and optical properties*. Chemical Engineering Journal, 2008. **140**(1-3): p. 632-637.
60. Zakharov, N.D. and P. Werner, *Three Dimensional Structure of UMo₈O₂₆: Ordering of U-Vacancies*. MRS Proceedings, 2002. **718**.
61. G. Wei, M.H., M. Ichinose, S. Miyata, N. Yokozeki, M. Myouchin, and M. Iwase,, *High Temp. Mater. Processes (Berlin, Ger.)*, 2014. **33**(4): p. 313-317.

62. Desal K.H., G.R.W., Parfitt D., Wiss T., Van Uffelen p., *Atomic-scale Simulation of Soluble Fission Products in UO₂*, in *EUR Report ISSN*, E.C.-J.R.C.-I.f.T. Elements, Editor. 2009, E Institute fo Transuranium Elements.
63. Lang, S.M., et al., *High-temperature reactions of uranium dioxide with various metal oxides*. 1956, National Bureau of Standards, Washington, DC.
64. Wolten, G.M., *Solid Phase Transitions in the UO₂-ZrO₂ System1*. Journal of the American Chemical Society, 1958. **80**(18): p. 4772-4775.
65. Cohen, I. and B.E. Schaner, *A metallographic and X-ray study of the UO₂-ZrO₂ system*. Journal of Nuclear Materials, 1963. **9**(1): p. 18-52.
66. Evans, P.E., *The System UO₂-ZrO₂*. Journal of the American Ceramic Society, 1960. **43**(9): p. 443-446.
67. Sunder, S., R. McEachern, and J.C. LeBlanc, *High-temperature, Knudsen cell-mass spectroscopic studies on lanthanum oxide/uranium dioxide solid solutions*. Journal of Nuclear Materials, 2001. **294**(1–2): p. 59-63.
68. Stadlbauer, E., et al., *Thermodynamics and phase relationships of the ternary lanthanum-uranium-oxygen system*. Journal of Solid State Chemistry, 1974. **10**(4): p. 341-350.
69. Dörr, W., S. Hellmann, and G. Mages, *Study of the formation of UO₂-PuO₂ solid solution by means of UO₂-CeO₂ simulate*. Journal of Nuclear Materials, 1986. **140**(1): p. 7-10.
70. Hanken, B.E., et al., *Energetics of cation mixing in urania-ceria solid solutions with stoichiometric oxygen concentrations*. Physical Chemistry Chemical Physics, 2012. **14**(16): p. 5680-5685.
71. Ali, M.E.-S. and R. Lorenzelli, *Kinetics of initial stage of sintering of UO₂ and UO₂ with Nd₂O₃ addition*. Journal of Nuclear Materials, 1979. **87**(1): p. 90-96.
72. Hinatsu, Y. and T. Fujino, *Magnetic susceptibilities of UO₂ • Nd₂O₃ solid solutions*. Journal of Solid State Chemistry, 1988. **73**(2): p. 388-397.
73. Grossman, L.N., J.E. Lewis, and D.M. Rooney, *The system UO₂-Eu₂O₃ at high temperatures*. Journal of Nuclear Materials, 1967. **21**(3): p. 302-309.
74. Berndt, U., R. Tanamas, and C. Keller, *The ternary UO₂ • UO₃ • EuO_{1.5}(EuO) system and investigation of Eu(II)-actinide(IV)-perovskites*. Journal of Solid State Chemistry, 1976. **17**(1): p. 113-120.
75. Durazzo, M., et al., *Phase studies in the UO₂-Gd₂O₃ system*. Journal of Nuclear Materials, 2010. **400**(3): p. 183-188.
76. Riella, H.G., et al., *UO₂-Gd₂O₃ solid solution formation from wet and dry processes*. Journal of Nuclear Materials, 1991. **178**(2): p. 204-211.
77. Beals, R.J. and J.H. Handwerk, *Solid Solutions in the System Urania—Rare-Earth Oxides: I, UO₂-GdO_{1.5}*. Journal of the American Ceramic Society, 1965. **48**(5): p. 271-274.
78. De Alleluia, I.B., et al., *Phase relationships for the ternary UO₂ • UO₂ • REO_{1.5} (RE = Rr, Nd, Dy) systems*. Journal of Inorganic and Nuclear Chemistry, 1981. **43**(8): p. 1831-1834.

79. Kim, H.-S., et al., *Thermal Expansion of (U, Dy) O₂ as a Function of Dy₂O₃*.
80. Keller, C., et al., *Phasengleichgewichte in den systemen uranoxid-oxide der seltenen erden (Ho, Er, Tm, Yb, Lu)*. Journal of Inorganic and Nuclear Chemistry, 1969. **31**(4): p. 965-980.
81. Housecroft, C.E. and A.G. Sharpe, *Inorganic Chemistry*. 2005: Pearson Prentice Hall.
82. Atkins, P., *Shriver and Atkins' Inorganic Chemistry*. 2010: OUP Oxford.
83. *Introduction to Phase Equilibria in Ceramic Systems*. 1984: Taylor & Francis.
84. Pelton, A.D., *Thermodynamics and Phase Diagrams of Materials, in Phase Transformations in Materials*. 2005, Wiley-VCH Verlag GmbH & Co. KGaA. p. 1-80.
85. Okamoto, H. and T.B. Massalski, *Thermodynamically Improbable Phase Diagrams*. Journal of Phase Equilibria, 1991. **12**(2): p. 148-168.
86. Okamoto, H. and T.B. Massalski, *guidelines for binary phase diagram assessment*. Journal of Phase Equilibria, 1993. **14**(3): p. 316-335.
87. McGreevy, R.L. and M.A. Howe, *The structure of molten LiCl*. Journal of Physics: Condensed Matter, 1989. **1**(49): p. 9957.
88. Takagi, R., H. Ohno, and K. Furukawa, *Structure of molten KCl*. Journal of the Chemical Society, Faraday Transactions 1: Physical Chemistry in Condensed Phases, 1979. **75**(0): p. 1477-1486.
89. Caccamo, C. and M. Dixon, *Molten alkali-halide mixtures: a molecular-dynamics study of Li/KCl mixtures*. Journal of Physics C: Solid State Physics, 1980. **13**(10): p. 1887.
90. Cook, E.L.W., *Phase Diagram for Ceramists*, 1989. **7**(The Am, Soc. Inc.).
91. Aspinall, H.C., *Chemistry of the f-Block Elements*. 2001: Taylor & Francis.
92. Okamoto, Y., F. Kobayashi, and T. Ogawa, *Structure and dynamic properties of molten uranium trichloride*. Journal of Alloys and Compounds, 1998. **271–273**: p. 355-358.
93. Meyer, G., H.C. Gaebell, and R. Hoppe, *K₂UCl₅, Rb₂UCl₅, UCl₃ and a comparison with analogous rare earth chlorides*. Journal of the Less Common Metals, 1983. **93**(2): p. 347-351.
94. R.E. Thoma, H.I., H. A. Friedman, G. D. Brunton, G. M. Hebert, T. N. McVay, *Reactor Chemistry Division Annual Progress Report ORNL- 3789*, W.R. Grimes, Editor. 1965.
95. Li, X., et al., *Dynamic Fluctuation of U³⁺ Coordination Structure in the Molten LiCl–KCl Eutectic via First Principles Molecular Dynamics Simulations*. The Journal of Physical Chemistry A, 2017. **121**(3): p. 571-578.
96. Suzuki, Y., et al., *Preparation of Neptunium Mononitride by Carbothermic Reduction*. Journal of Nuclear Science and Technology, 1994. **31**(7): p. 677-680.
97. Shirai, O., et al., *Electrode reaction of the Np³⁺/Np couple in LiCl–KCl eutectic melts*. Journal of Applied Electrochemistry, 2001. **31**(9): p. 1055-1060.

98. Shirai, O., et al., *Recovery of Neptunium by Electrolysis of NpN in LiCl-KCl Eutectic Melts*. Journal of Nuclear Science and Technology, 2000. **37**(8): p. 676-681.
99. Sakamura Y., S.O., Iwai T., Suzuki Y., *The thermodynamics of neptunium in LiCl-KCl eutectic/liquid bismuth systems*. Journal of the Electrochemical Society, 2000. **147**(2): p. 642-649.
100. Roy J.J., G.L.F., Grimmett D.L., Fusselman S.P., Krueger C.L., Storvick T.S., Inoue T., Sakamura Y., Takahshi N., *Thermodynamic Properties of U, Np, Pu, and Am in Molten LiCl-KCl Eutectic and Liquid Cadmium*. The Journal of the Electrochemical Society 1996. **143**(8): p. 2487-2492.
101. Krueger, C., et al., *Measurement of the standard potential of the Np (III)/Np (O) couple in LiCl-KCl eutectic*. Journal of the Electrochemical Society, 1991. **138**(4): p. 1186-1187.
102. Sakamura, Y., et al., *Chlorination of UO₂, PuO₂ and rare earth oxides using ZrCl₄ in LiCl-KCl eutectic melt*. Journal of Nuclear Materials, 2005. **340**(1): p. 39-51.
103. Hayashi, H., et al., *Syntheses of neptunium trichloride and measurements of its melting temperature*. Journal of Nuclear Materials, 2013(0).
104. Foropoulos J., A.L., Trujillo E.A, *Dehydration of Plutonium or Neptunium Trichloride Hydrate*, U.S.D.o. Energy, Editor. 1992.
105. Fried, S., *METHODS OF MAKING-NEPTUNIUM*. 1951, Google Patents.
106. Fuger J., P.V.B., Hubbard W.N., Oetting F.L., , *The Actinide Halides*. 1 ed. The Chemical Thermodynamics of Actinide Elements and Compounds, ed. R.M.H. Medvedev V., Westrum E.F., Oetting F.L. Vol. 8. 1983, Vienna: IAEA. 267.
107. Masset P., A.C., Konings R. J. M., Malmbeck R., *Electrochemical behaviour of neptunium in the molten LiCl-KCl eutectic*. Journal of Electroanalytical Chemistry 2007. **603**: p. 166-174.
108. Carnall W.T., C.H.M., Pappalardo R.G., Cohen D., Fried S., et al. , *Absorption spectra of NpCl₃ and NpBr₃*. The Journal of Chemical Physics 1974. **61**(12): p. 4993-5008.
109. Spirlet, M.-R., X. Jemine, and J. Goffart, *A single-crystal X-ray structure determination of neptunium tetrachloride*. Journal of Alloys and Compounds, 1995. **216**(2): p. 269-271.
110. Fuger, J., D. Brown, and J.F. Easey, *Thermodynamics of the actinide elements. Part I. Heats of formation of crystalline neptunium tetrachloride, neptunium oxide dichloride, and neptunium trioxide monohydrate, and a new determination of the heat of formation of the Np and Np ions in M-hydrochloric acid*. Journal of the Chemical Society A: Inorganic, Physical, Theoretical, 1969(0): p. 2995-2998.
111. Bagnall, K.W. and J.B. Laidler, *Neptunium chloro-complexes*. Journal of the Chemical Society A: Inorganic, Physical, Theoretical, 1966. **0**(0): p. 516-520.
112. Fried, S., *Transuranic metal halides and a process for the production thereof*. 1951, Google Patents.

113. Polovov I.B., S.C.A., May I., Vasin B.D., Volkovich V.A., Griffiths T.R., *Spectroelectrochemical Studies of Uranium and Neptunium in LiCl-KCl Eutectic Melt*. Electrochemical Society Transactions, 2007. **3**(35): p. 503-511.
114. Fried, S. and N. Davidson, *The Preparation of Solid Neptunium Compounds I*. Journal of the American Chemical Society, 1948. **70**(11): p. 3539-3547.
115. Brown, D. and J. Edwards, *Preparation and crystallographic properties of the trichlorides, tribromides, and tri-iodides of uranium, neptunium, and plutonium*. Journal of the Chemical Society, Dalton Transactions, 1972(16): p. 1757-1762.
116. Ionova, G., C. Madic, and R. Guillaumont, *Covalency effects in the standard enthalpies of formation of trivalent lanthanide and actinide halides*. Radiochimica Acta, 1997. **78**: p. 83-90.
117. Westrum, E.F. and L. Eyring, *The Heat of Solution of Neptunium Metal and the Heats of Formation of Some Neptunium Chlorides. A Microcalorimeter for Heat of Solution Measurements I*. Journal of the American Chemical Society, 1952. **74**(8): p. 2045-2047.
118. Cummings, B.B., Nucleonics, 1949. **5**(5): p. 62-85.
119. Lemire R.J., F.J., Spahiu K., Nitche H., Sullivan J.C., Ullman W.J., Potter P., Vitorge P., Rand M.H., Wanner H., Rydberg J., *Chemical Thermodynamics of Neptunium and Plutonium*. Chemical Thermodynamics ed. O.N.E. Agency. Vol. 4. 2001, Issy-les-Moulineaux: Nuclear Energy Agency. 845.
120. Bratsch, S.G. and J.J. Lagowski, *Actinide thermodynamic predictions. 3. Thermodynamics of compounds and aquo-ions of the 2+, 3+, and 4+ oxidation states and standard electrode potentials at 298.15 K*. The Journal of Physical Chemistry, 1986. **90**(2): p. 307-312.
121. Kubaschewski O., A.C.B., Spencer P.J., *Materials Thermochemistry*. 6th ed. 1993, Oxford, UK,; Pergamon Press.
122. Rand M.H., F.J., *The Thermodynamic Properties of the Transuranium Halides* 2000: European Communities, 2000.
123. Konings R. J. M., M.R., Serp J., , *Evaluation of thermochemical and electrochemical data for the pyrochemical partitioning process*. Journal of Nuclear Science and Technology, 2002. **Supplement 3**: p. 906-909.
124. Krestov, G.A., *Thermochemistry of compounds of rare-earth and actinide elements*. 1972, Washington D.C.: Joint Publications Research Service.
125. Zachariasen, W., *Crystal chemical studies of the 5f-series of elements. XII. New compounds representing known structure types*. Acta Crystallographica, 1949. **2**(6): p. 388-390.
126. Konings R. J. M., M.L.R., Fuger J. , *Thermodynamic Properties of Actinides and Actinide Compounds*, in *The Chemistry of the Actinide and Transactinide Elements*, E.N.M. Morss L.R., Fuger J., Editor. 2006, Springer: Dordrecht. p. 2113-2224.

127. Choppin, G.R., J.-O. Liljenzin, and J.A.N. Rydberg, *CHAPTER 21 - The Nuclear Fuel Cycle*, in *Radiochemistry and Nuclear Chemistry (Third Edition)*. 2002, Butterworth-Heinemann: Woburn. p. 583-641.
128. Liu, L.G., *Eart Planet Sci. Lett*, 1982. **1**: p. 110.
129. Barshick, C., D. Duckworth, and D. Smith, *Inorganic Mass Spectrometry: Fundamentals and Applications*. 2000: Taylor & Francis.
130. G. Hörne, W.F.H., H. J. Flammersheim *Differential Scanning Calorimery*, ed. S.-V.B. Heidelberg. 2003.
131. Hörne G., H.W.F., Flammersheim H.J., *Differential Scanning Calorimery*, ed. S.-V.B. Heidelberg. 2003.
132. Gao, Y.L., et al., *Calorimetric measurements of undercooling in single micron sized SnAgCu particles in a wide range of cooling rates*. *Thermochimica Acta*, 2009. **482**(1-2): p. 1-7.
133. Thomas, L.C., *Use of multiple heating rate DSC and modulated temperature DSC to detect and analyze temperature-time-dependent transitions in materials*. *American Laboratory*, 2001. **33**(1): p. 26-31.
134. Brundle, C.R., C.A. Evans, and S. Wilson, *Encyclopedia of Materials Characterization: Surfaces, Interfaces, Thin Films*. 1992: Butterworth-Heinemann.
135. Rose, M.A., M.A. Williamson, and J. Willit, *Investigation of residual anode material after electrorefining uranium in molten chloride salt*. *Journal of Nuclear Materials*, 2015. **467**, **Part 2**: p. 576-581.